UC San Diego

UC San Diego Electronic Theses and Dissertations

Title

Addressing the Instability and Improving the Commercialization Prospects of Perovskite Photovoltaics Through a Layer by Layer Approach

Permalink

https://escholarship.org/uc/item/01277687

Author

Kodur, Moses Nathaniel

Publication Date

2023

Peer reviewed|Thesis/dissertation

UNIVERSITY OF CALIFORNIA SAN DIEGO

Addressing the Instability and Improving the Commercialization Prospects of Perovskite
Photovoltaics Through a Layer by Layer Approach

A dissertation submitted in partial satisfaction of the
requirements for the degree Doctor of Philosophy

in

Chemical Engineering

by

Moses Nathaniel Kodur

Committee in charge:

Professor David Fenning, Chair
Professor Prabhakar Bandaru
Professor Darren Lipomi
Professor Oscar Vazquez Mena
Professor Ying Shirley Meng

2023

The Dissertation of Moses Nathaniel Kodur is approved, and it is acceptable in quality and form for publication on microfilm and electronically.

University of California San Diego

2023

DEDICATION

I dedicate my dissertation work to my family and friends who have supported me through this whole journey.

EPIGRAPH

It is paradoxical, yet true, to say, that the more we know, the more ignorant we become in the absolute sense, for it is only through enlightenment that we become conscious of our limitations. Precisely one of the most gratifying results of intellectual evolution is the continuous opening up of new and greater prospects.

Nikola Tesla

TABLE OF CONTENTS

LIST OF FIGURES

LIST OF TABLES

ACKNOWLEDGEMENTS

I would like to express my deep gratitude to Professor David Fenning for supporting me as my research mentor for the past five years and serving as the chair of my committee. By passing on a wealth of knowledge, pushing me to grow in my scientific thinking, and inspiring me to pursue excellence, Professor Fenning has made me both a better researcher and person. Additionally, I want to thank the many members of the Fenning Research Group, both past and present, including, but not limited to: Dr. Yanqi Luo, Dr. Taewoo Kim, (soon to be) Dr. Xueying Quinn, Dr. Jonathan Scarf, Dr. Rishi Kumar, Dr. Erick Martinez Loran, Dr. Guillaume von Gastrow, Dr. Sean Dunfield, Pedram Abbasi, Deniz Cakan, Isabel Albelo, Connor Dolan, Zhewen Deng, Guang-yu Lee, Jack Palmer, Manas Likhit, Zachary Dorfman, Shreya Rengarajan, Apoorva Gupta, Vivek Devalla, Ethan Jing, Tala Sidawi, Andrew Zakoor, Justin Skaggs, Eric Oberholtz, Sara Dorr, Sophia Alm, Joshua Gong, Elizabeth Pegg, and Mason Holst who have been amazing teammates and made my time in graduate school enjoyable and fruitful.

I would also like to acknowledge the many collaborators from UC San Diego whose contributions and neighborly help were vital to my projects including members of Dr. Shirley Meng's lab: Dr. Shen Wang (who taught me how to make my first perovskite solar cell), Dr. Min-cheol Kim, Dr. Thomas Brenner, Oystein Fjeldberg, and So-Yeon Ham; and members of Dr. Darren Lipomi's lab: Dr. Rory Runser, Dr. Mickey Finn, Guillermo Esparza, and Alexander Chen. I also had the pleasure of working with several external collaborators including Dr. Ross Kerner, Dr. Joseph Berry, and Dr. Neil Dasgupta (and their teams) who provided a inspiring exchange of ideas that led to exciting discoveries even beyond what is published in this dissertation.

Prior to and through graduate school, I have had an amazing support structure and am grateful for all the encouragement along the way. I am thankful for Chabot Community College and the professors who went above and beyond to prepare me for graduate school. As an undergraduate researcher, Dr. Chuze Ma and Dr. Judith Alvarado were amazing mentors and equipped me for graduate level research. Thank you to the UC LEADs program, the Navigators at

UC San Diego, Laurel Bible Chapel, and the Sloan Program for their mentorship and professional development meetings.

Lastly, I want to acknowledge my family for their abundant, overflowing support and encouragement. It is much easier to face the challenges of the day with such a strong and loving family who cheers you on. I have special gratitude to my loving parents, Silas and Darlene Kodur, who laid the foundation for my education. My beautiful wife, Laura, whose words of encouragement and endless patience through countless late nights has pushed me to the end. And my in-laws, Scott and Dotty Calvin, who have graciously accepted me as part of the family.

Chapter 2, in full, is a reprint of the material "Stability of Perovskite Films Encapsulated in Single- and Multi-Layer Graphene Barriers" by Rory Runser, Moses Kodur, Justin H. Skaggs, Deniz N. Cakan, Juliana B. Foley, Mickey Finn III, David P. Fenning, and Darren J. Lipomi as it appears in ACS Applied Energy Materials. The dissertation author was the first author of this paper, all authors contributed to this work.

Chapter 3, in full, is a reprint of the material "Electrochemical Screening of Contact Layers for Metal Halide Perovskites" by Moses Kodur, Zachary Dorfman, Ross A. Kerner, Justin H. Skaggs, Taewoo Kim, Sean P. Dunfield, Axel Palmstrom, Joseph J. Berry, and David P. Fenning as it appears in ACS Energy Letters. The dissertation author was the first author of this paper, all authors contributed to this work.

Chapter 4, in part, is under preparation to be submitted under the title "Solvent-free Transfer of Freestanding Large-Area Conjugated Polymer Films for Optoelectronic Applications" by Guillermo L. Esparza, Moses Kodur, Benjamin Wang, Alexander X. Chen, Rory Runser, David P. Fenning, and Darren J. Lipomi. The dissertation author was the primary investigator and author of this material The dissertation author was the primary investigator and author of this material.

Chapter 5, in part, is under preparation to be submitted under the title "Robotic High-Throughput Screening Identifies Durable Halide Perovskite Absorbers for Tandem Photovoltaics" by Rishi E. Kumar, Moses Kodur, Deniz N. Cakan,Jack Palmer, Apoorva Gupta, Eric Oberholtz,

Sean P. Dunfield, David P. Fenning. The dissertation author was the primary investigator and author of this material.

VITA

PUBLICATIONS

(* = authors contributed equally to the work)

1. Ma, C., Alvarado, J., Xu, J., Clément, R. J., Kodur, M., Tong, W., Grey, C. P., Meng, Y. S., Exploring Oxygen Activity in the High Energy P2-Type Na0.78Ni0.23Mn0.69O2 Cathode Material for Na-Ion Batteries. Journal of the American Chemical Society 2017, 139 (13), 4835–4845.

2. Alvarado, J., Ma, C., Wang, S., Nguyen, K., Kodur, M., Meng, Y. S., Improvement of the Cathode Electrolyte Interphase on P2-Na2/3Ni1/3Mn2/3O2 by Atomic Layer Deposition. ACS Applied Materials Interfaces 2017, 9 (31), 26518–26530.

3. Kodur, M., Kumar, R. E., Luo, Y., Cakan, D. N., Li, X., Stuckelberger, M., Fenning, D. P., X-Ray Microscopy of Halide Perovskites: Techniques, Applications, and Prospects. Advanced Energy Materials 2020, 10 (26), 1903170.

4. Quinn, X. L., Kumar, R. E., Kodur, M., Cakan, D. N., Cai, Z., Zhou, T., Holt, M. V., Fenning, D. P., Europium Addition Reduces Local Structural Disorder and Enhances Photoluminescent Yield in Perovskite CsPbBr3. Advanced Optical Materials 2021, 2002221, 2002221.

5. Choudhary, K., Chen, A., Runser, R., Urbina, A., Dunn, T., Kodur, M., Kleinschmidt, A., Fenning, D. P., Ayzner, A., Lipomi, D. J., Comparison of the Mechanical Properties of a Conjugated Polymer Deposited using Spin Coating, Interfacial Spreading, Solution Shearing, and Spray Coating. ACS Applied Materials Interfaces 2021, 13 (43): 51436–46

6. Runser, R.*; Kodur, M.*; Skaggs, J. H.; Cakan, D. N.; Foley, J. B.; Finn, M.; Fenning, D. P.; Lipomi, D. J., Stability of Perovskite Films Encapsulated in Single- and Multi-Layer Graphene Barriers. ACS Applied Energy Materials 2021, 4 (9), 10314-10322.

7. Kodur, M.*, Dorfman, Z.*, Kerner, R., Skaggs, J., Kim, T., Dunfield, S., Palmstrom, A., Berry, J. J., Fenning, D. P., Electrochemical Screening of Contact Layers for Metal Halide Perovskites. ACS Energy Letters 2021, 7 (2), 683–89

ABSTRACT OF THE DISSERTATION

Addressing the Instability and Improving the Commercialization Prospects of Perovskite
Photovoltaics Through a Layer by Layer Approach

by

Moses Nathaniel Kodur

Doctor of Philosophy in Chemical Engineering

University of California San Diego, 2023

Professor David Fenning, Chair

The ascent of perovskite photovoltaics has been one of the most significant and exciting developments in renewable energy research. The myriad of absorber composition blends and compatible device structures offer a wide variety of applications and several paths towards full commercial deployment. However, the rapid decrease in performance of perovskite photovoltaics under operational conditions prohibits their ubiquitous distribution.

In this dissertation, a top to bottom approach is utilized to advance the commercial viability of perovskite photovoltaics. Beginning with encapsulation schemes, large-area graphene stacks with a polyisobutylene edge seal were investigated as potential moisture and oxygen

barriers for perovskite films. These materials were found to provide a moderate but insufficient protection from a damp heat environment. However, an all-glass encapsulation scheme enabled over 1000 hours of exposure to damp heat (85 °C, 65% RH) without any loss in film quality (validated by photoluminescence, UV-Vis spectroscopy, and X-ray diffraction). Attention was then focused on the selective contact layers, beginning with a presentation of electrochemical measurements that were adapted to study the optoelectronic properties, surface coverage, and reactivity of transport layers. Tin oxide, commonly used as an electron transport layer in perovskite photovoltaics, was highlighted as a case study to demonstrate the screening potential of these tools by correlating cyclic voltammetry on a bottom selective contact to final device performance once the device stack was completed. Chronoamperometry was also used to test the reactivity of tin oxide, at the surface, to acidic perovskite precursors, which can potentially be used to predict the reactivity of perovskites at buried interfaces within a device. Next, a solvent-free dry transfer process was designed and highlighted for its ability to deposit a large, uniform film of conjugated polymers which are frequently used as hole transport layers in perovskite photovoltaics. This technique is especially useful for top selective contacts since it eliminates concerns with solvent compatibility of the underlying perovskite film. Lastly, design considerations of the absorber were comprehensiviely explored through the development of a high throughput Perovskite Automated Solar Cell Assembly Line which was used, in combination with active learning principles, to design and test wide bandgap perovskite absorbers for use in silicon-perovskite tandem photovoltaics. Overall, this dissertation presents the steps that we have taken to advances perovskite photovoltaics from an intriguing research project to an effective and vital technology that aid in addressing the ever increasing global energy demands.

Chapter 1

Introduction: The Rise of Perovskites

1.1 A History of Photovoltaics

Increases in technology and population across the globe have exponentially increased energy consumption. To keep up with these demands, substantial improvements to energy generation, transport, and storage will be required. Of sustainable options, solar energy represents a particularly untapped source for energy generation. As a giant nuclear reactor, the sun radiates an unfathomable amount of energy of which a small fraction enters our domain, the earth. Sunlight keeps the earth warm and inhabitable and it is essential for agriculture, producing crops and raising livestock. Energy from the sun is stored in organic species which eventually turn into wood, coal, and oil. In other words, the vast majority of energy consumed by humanity has ultimately come from the sun. But until recently, humans have not managed to collect energy directly from the sun.

Our foray into the world of photovoltaics (PV), namely devices that collect light (photons) and convert it into electricity (voltage and current), began when French physicist Antoine-César Becquerel observed a light dependent voltage in an experiment involving a solid electrode in an electrolyte solution in 1839. However, it wasn't until 1883 that Charles Fritts, who used junctions formed by coating selenium with gold, built the first genuine photovoltaic device with a power conversion efficiency (PCE) of approximately 1%. After that, photovoltaics development stalled until 1953 when physicists from the Bell Laboratories (Gerald Pearson, Calvin Fuller, and Daryl

Chapin) designed the first practical photovoltaic device made out of silicon.[6] Since then, silicon photovoltaics have increased rapidly in stability and PCE. Additionally, other photovoltaic technologies have been developed. However, the unique combination of high performance, relatively low cost, good durability, and material availability has given silicon photovoltaics the distinction as the most popular and widespread technology to date.

Photovoltaics made from mono- and poly-crystalline silicon represent the first generation of solar cells. These devices rely on heavily n-doped and p-doped silicon to form a p-n junction that, when put in contact with one another, facilitates the extraction of electron-hole pairs. While the abundance of silicon in the earth's crust held promise to drive down the material cost of silicon, the high purity requirements for PV application necessitates high temperature processing which increases the overall cost and energy payback time of silicon PV. Despite tremendous progress, the expensive fabrication and non-ideal semiconductor properties of silicon form inherent limitations in reducing the cost per kilowatt hour of silicon PV, either by means of reducing the price or increasing its efficiency; as a result, wide-spread installation of silicon PVs remains cost prohibitive, particularly at the residential level.

In an attempt to address the high manufacturing costs associated with the first generation of vacuum deposited thick ($\sim 300 \mu$m) crystalline semiconductors such as silicon, the second generation of PV consists mostly of thin-film semiconductors processed at low temperatures. This includes materials such as GaAs, CdTe, $CuInGaSe_2$ (CIGS), and amorphous silicon(a-Si:H). While these technologies have had a fair amount of success (e.g. GaAs holds the record efficiency for a single junction solar cell), their cost per kilowatt hour (aside from amorphous silicon), primarily driven by material scarcity, limits their prospects for widespread adoption.

Seeking to find thin-film semiconductors based on abundant sources, researchers next turned to organic, dye-sensitized, quantum-dot, and perovskite solar cells (PSCs). While much cheaper than silicon and more sustainable than second generation PV materials, this third generation of PV devices has largely fallen short of hopes, with the notable exception of metal halide perovskite solar cells (Figure 1.1).
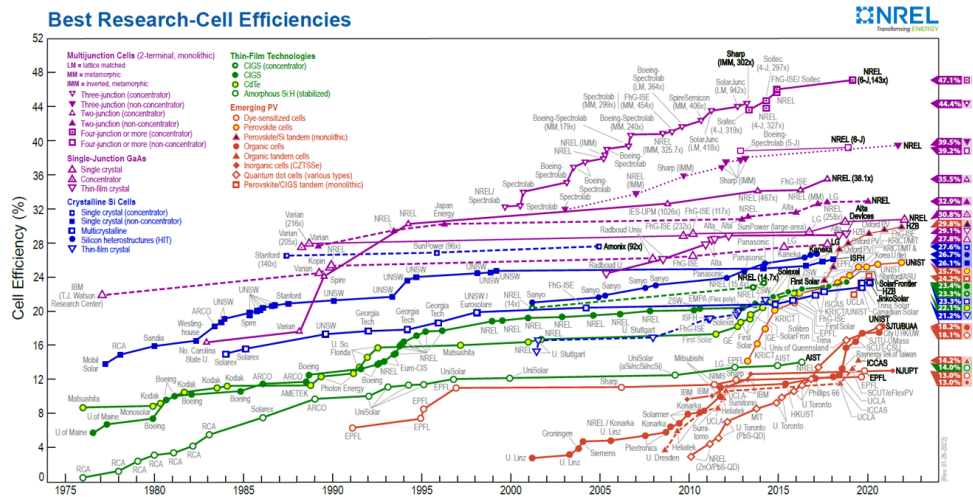
Figure 1.1. Record of highest performing research-cell efficiencies for each major PV technology.[1]

1.2 The Allure of Perovskites

The first metal halide perovskite solar cells were made in 2009 and had PCEs of just 3.8%. However, over the past 13 years, the record PCE has risen to 25.7%, making it more efficient than poly-crystalline silicon PV and rapidly closing in on mono-crystalline silicon PV. Moreover, since the active layer is a thin-film (typically around 500 nm) made from abundant elements, the material cost of the absorber is around 5-10% that of poly-crystalline silicon.

Metal halide perovskites are a family of materials that share a crystal structure of ABX_3 where A is composed of monovalent cations typically methylammonium (MA^+), formamidinium (FA^+), cesium (Cs^+) and rubidium (Rb^+); B contains divalent metal cation such as Pb^{2+} or Sn^{2+}; and X hosts halogen anions such as I^-, Br^- or Cl^-.[7] The compositional flexibility of perovskite materials allows its bandgap, conductivity, thermodynamic stability, and other optoelectronic properties to be fine-tuned through simple chemical substitutions. Furthermore, perovskite absorbers are known to have intrinsic properties that are very favorable for photovoltaic performance including a high absorption coefficient,[8] suitable and tunable bandgap,[9] long carrier diffusion lengths,[10] ambipolar carrier transport,[11] and high carrier mobilities.[12] And finally, perovskites are easily fabricated from low energy, low cost processes forecasting a low overall

production cost.[13]

1.3 Challenges Facing Perovskite Photovoltaics

Typical perovskite solar cells are made in either an n-i-p or p-i-n architecture where the perovskite serves as the light-absorber "intrinsic" (i) material that is sandwiched between selective n- and p- type selective contacts that extract electrons and holes, respectively, via band alignment at the interface.
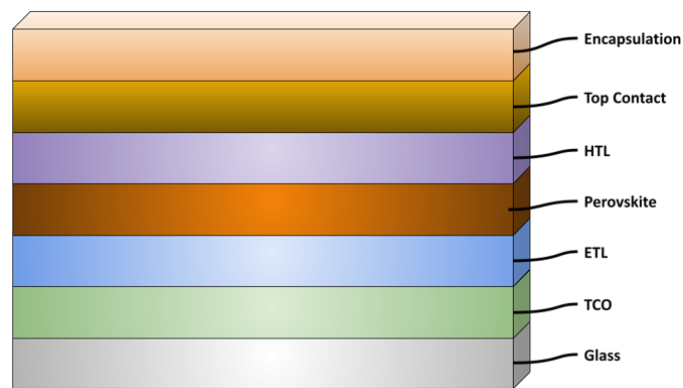
Figure 1.2. Schematic of a generic n-i-p perovskite solar cell.

While perovskites have great optoelectronic properties, have realized high efficiencies, and can likely be scaled through a variety of depositions methods, their commercialization prospects have been hindered by their poor stability. Specifically, perovskite solar cells are susceptible to degradation induced by light, elevated temperature, applied potential, oxygen, and moisture.[14–16] While the durability of PSCs has been greatly improved, they still requires significant progress before they can be considered a reliable PV technology.

1.4 An Overview of This Work

In this work I highlight advancements I made, with the assistance of many colleagues, on each layer of the perovskite solar cell, with an emphasis on improving both the short- and long-term performance of the device.

In **Chapter 2**, we explore encapsulation schemes for perovskites via single- and multi-layered graphene barriers. The use of graphene as a functionalized moisture , that participates in the the solar cell function in addition to protecting it from the atmosphere, has often been pitched, but not explored comprehensivey. In this section, we highlight the challenges of scaling up graphene-based barriers to research-scale devices ($< 5 \text{ cm}^2$) which does not bode well for large area photovoltaics. As an alternative, we demonstrate that polyisobutylene edge seals between two sheets of glass creates a viable encapsulation scheme that is resilient to increased temperature and humidity (50 days at 85 °C and 65% RH with no PSK film degradation).

In **Chapter 3**. we demonstrate the adaptation of easily accessible electrochemical tools and analysis for screening of transport layers in the perovskite solar cell stack. Specifically, we perform cyclic voltammetry (CV) scans on several batches of vacuum thermally evaporated tin oxide and compare CV metrics to finished device figures of merit to identify correlations that can be used to predict the V_{OC} and J_{SC} of the devices. Additionally, we couple these measurements to potentiostatic measurements (chronoamperometry) in a MAI-based electrolyte to probe the reactivity of the tin oxide with acidic perovskite precursors, ultimately showing that it is dependent on the oxidation state of the tin oxide at the surface (as confirmed by XPS).

In **Chapter 4**, we unveil a solvent-free transfer (SFT) method to deposit conjugated polymers onto planar substrates while curtailing solvent compatibility requirements. Specifically, using poly(3-alkylthiophene)s (P3ATs) as hole transport layers in a perovskite solar cell, we show that the SFT method can yield devices of similar quality to their spin-coated analogues.This opens the door for the SFT of other conjugated polymers onto the perovskite that would normally be destructive to the underlying with traditional sequential deposition methods.

Finally, in **Chapter 5**, we debut the Perovskite Automated Solar Cell Assembly Line (PASCAL) to enable high throughput fabrication and analysis of perovskite films and devices. To demonstrate its capability, we explore the triple cation, triple halide compositional space to identify promising wide bandgap perovskite absorbers for silicon-perovskite tandem applications.

Together, these innovations address issues with environmental ingress, contact layer

characterization, contact layer fabrication, and perovskite compositional exploration– addressing almost all areas of the perovskite device that are currently lacking for commercialization.

Chapter 2

Stability of Perovskite Films Encapsulated in Single- and Multi-Layer Graphene Barriers

2.1 Introduction

As mentioned previously, the stability of perovskite solar cells (PSCs) remains as one of the major challenges on their path towards commercialization and wide-scale deployment.[17] While the record efficiencies of PSCs continue to rise,[18,19] their sensitivity to environmental factors such as moisture,[20,21] oxygen,[14] temperature,[22] and light[23,24] limit their economic and practical viability. To address these concerns, researchers have undertaken several lines of inquiry in order to extend the lifetimes of PSCs. These areas of research focus fall broadly into three categories: (1) the development of new perovskite compositions with greater intrinsic stability (e.g. mixed cation and/or halides composition blends);[15,25–27] (2) the optimization of interfaces within devices, so as to minimize defects and vacancies;[14,20,28,29] and (3) the encapsulation of devices in order to slow the ingress of moisture and oxygen.[30–34] In this chapter, we present our investigation into graphene for its use as an encapsulation material in PSCs.

To measure the stability against these stressors, researchers often use accelerated degradation studies, in which materials or whole devices are subjected to extreme conditions that simulate long-term degradation. Recently, the research community has attempted to standardize

testing protocols to aid in the comparison of stability measured in different laboratories.[35] For example, the vulnerability of perovskites to heat, moisture, and oxygen can be simultaneously evaluated using "damp heat testing," in which devices or films are subjected to high temperatures and humidity in order to rapidly simulate the effects of long-term degradation.[14, 20, 21, 36, 37] These accelerated testing conditions have proven to be a challenging stability threshold for perovskite photovoltaics to overcome due to their intrinsic sensitivity to oxygen and water.[21, 30, 38–40] One obstacle in devising scalable encapsulation schemes for PSC is that typical materials used for encapsulation of solar cells or other semiconductors—typically ethylene vinyl acetate or other polyolefins—require processing temperatures often around 150 °C.[41, 42] In PSCs, however, such temperatures can destabilize the perovskite absorber, the hole-transport layer (HTL), or both.[43, 44] As a result, PSCs often exhibit a reduction in efficiency after encapsulation,[37] and relatively long-lasting PSCs have a lower efficiency compared to record devices.[45] It is therefore critical to investigate new barrier materials and encapsulation techniques that are compatible with PSCs.

Graphene is an intriguing material for thin-film, flexible barriers due to the impermeability of its basal plane to gases[46] as well as its high optical transmissivity.[47] In this paper we investigate the efficacy of graphene barriers towards preventing the degradation of perovskite films, using an encapsulation scheme shown in Figure 2.1. The use of a low-temperature-activating polyisobutylene (PIB) edge seal results in a high-quality encapsulation without causing degradation of the film, and ensures that any small species ingress is through the barrier film being investigated.[30, 48, 49] Numerous papers already speculate an enhancement to the stability of perovskite solar cells (PSCs) when encapsulated with graphene.[20, 50] Graphene derivatives, including fluorine-doped nano-platelets[51] and graphene oxides,[52, 53] have also been shown to increase the stability of PSCs. Various studies have also incorporated graphene into PSCs as an electrode material (due to the electrical conductivity of graphene) either in combination with or separate from barrier applications.[7, 54] Nonetheless, the presence of grain boundaries and defects within CVD graphene can provide numerous permeation pathways for species such as water and oxygen.[55] As a result, many reports of improved PSC stability due to encapsulation with

graphene may not be due entirely to graphene itself, but rather aided by the polymeric support layer on which the graphene is adhered.
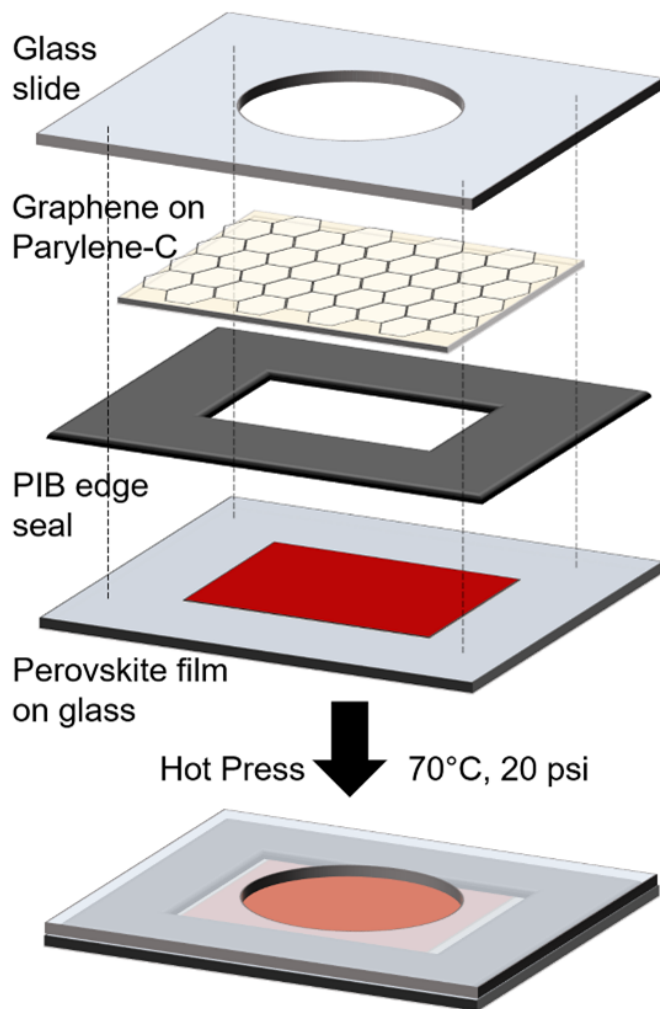
Figure 2.1. A schematic drawing of the exploded image view of a perovskite film encapsulated with graphene on a polymeric backbone.

One method to reduce the availability of these pathways for the permeation of gases is by stacking multiple monolayers of graphene on top of eachother. With multiple layers, transport through grain boundaries and pinholes may become blocked by adjoining layers.[56] Here we measure the performance of barriers composed of up to three layers of graphene (Figure 2.2a), beyond which the cost, complexity of fabrication, and optical losses (2.3% per layer of graphene)[47] (Figure 2.2b) would be impractical for optoelectronic devices, such as

9

thin-film solar cells.
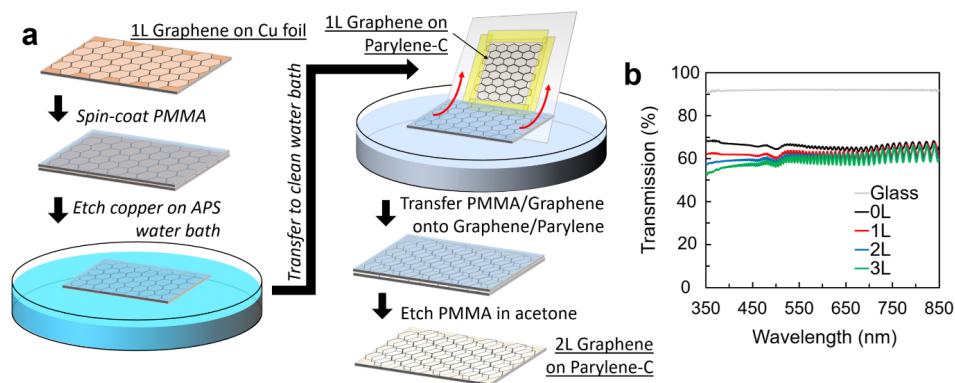
Figure 2.2. Preparation of multi-layer graphene barrier films. a) Schematic illustration of fabrication of 2-layer graphene on parylene. b) UV-Vis transmission spectra of graphene-on-parylene barriers as a function of the number of graphene layers.

2.2 Materials and Methods

2.2.1 Materials

Formamidinium iodide (FAI) and methylammonium bromide (MABr) were purchased from GreatCell Solar Materials. CsI (99.999% purity), DMSO (99.9% purity), DMF (99.9% purity), and chlorobenzene (99.9% purity) were purchased from Sigma-Aldrich. PbI_2 (99.99% purity) and $PbBr_2$ (99.99% purity) were purchased from TCI. Poly(methyl methacrylate) (PMMA, M_W = 550,000) was obtained from Alfa Aesar. Ammonium persulfate (APS) and anisole were obtained from Acros Organics. Prior to use, all solvents were dried for 24 hours with 3Å molecular sieves (VWR, grade 564, mesh 8-12) then filtered with a 0.22 μm PTFE syringe filter. Monolayer CVD graphene on copper foil and monolayer graphene mounted on 10 µm parylene-C were supplied by Grolltex, Inc, with a >95% surface coverage of graphene as determined by optical microscopy. Polyisobutylene (PIB) edge seal sheets were obtained from Quanex.

2.2.2   Preparation of Graphene Materials

Monolayer graphene on 10 μm parylene-C (hereafter referred to as 1L) was used as is. The procedure we used to prepare 2-layer (2L) and 3-layer (3L) graphene on parylene-C involved iterative deposition of monolayer graphene,[50,57] shown in Figure 2.2a. Briefly, monolayer graphene on copper foil (5 cm × 5 cm) was spin-coated with a 4 wt% PMMA solution in anisole at 4000 RPM for 60 seconds. After annealing at 150 °C for 5 minutes to remove any remaining anisole, the copper was etched in a 0.05 g/mL solution of APS in water for 2 hours, until fully dissolved. The resulting floating PMMA/graphene was transferred to a clean water bath. Separately, a 5 cm × 5 cm piece of 1L graphene was taped to a glass slide, graphene facing up. The PMMA/graphene was transferred directly onto the 1L film, with the two graphene layers in direct contact, and allowed to dry overnight in a desiccator. Finally, the PMMA was removed by etching in a 50 °C bath of acetone for 5 minutes, then rinsed with IPA and allowed to dry. This process was repeated once more to yield 3-layer graphene. Successful graphene transfer was confirmed via UV-Vis (Figure 2.2b) showing a successive decrease in optical transmission with each layer of graphene added. Lastly, 0L graphene (aka plain 10 μm parylene-C) was obtained by treating 1L films with plasma (30 W) for 30 seconds at a base pressure of 250 mTorr of air. Graphene removal was confirmed via sheet resistance measurements which showed no conductivity in the resulting films, as well as UV-Vis showing an increase in optical transmission (Figure 2.2b).

2.2.3   Preparation of Perovskite Films

Substrates—glass or fluorine-doped tin oxide (FTO)—were cleaned through a series of sonication (15 minutes) and rinse steps in the following sequence: 2 v% Hellmanex in DI water, DI water, isopropanol, and acetone. Afterward, the substrates were rinsed in IPA and dried with compressed air.

The triple cation perovskite films were prepared in a nitrogen-filled glovebox. First, two

separate solutions of 1.5 M lead iodide(PbI_2) and 1.5 M lead bromide($PbBr_2$) were prepared with a 9:1 volume ratio of DMF and DMSO used as a solvent. The solutions were vortexed then heated to 100 °C for 10 minutes. The PbI_2 solution was added to FAI and $PbBr_2$ solution was added to MABr such that 1.22 M solutions of $FAPbI_3$ and $MAPbBr_3$, respectively, with a 1.09 over-stoichiometric ratio of the lead salts were formed (using the 9:1 DMF:DMSO solution to dilute as necessary). An additional solution of 1.5 M CsI in DMSO was prepared in the glovebox and heated at 150 ° for 10 minutes. The $FAPbI_3$ and $MAPbBr_3$ solutions were mixed together in a 5:1 ratio and 5% molar ratio (with respect to the A-site) of CsI was added to the final solution resulting in a nominal stoichiometry of $FA_{0.79}MA_{0.16}Cs_{0.05}Pb(I_{0.84}Br_{0.16})_3$.

The perovskite films were formed by spin coating. Prior to deposition the substrates were treated with air-based plasma for 10 minutes at 300 mTorr. 90 μL of solution was dropped onto the substrate and doctor bladed across the entire surface. The first step of the spin-cast at 1000 RPM for 10 seconds served to remove excess solution and ensure an even spread across the entirety of the substrate. In the second step, the speed was increased to 5500 RPM for 20 seconds. 250 μL of chlorobenzene was dispensed rapidly (in approximately 1 second) after 8 seconds had expired in step 2 of the spin-coat. The films were annealed on a hotplate for 45 minutes at 100 °C, resulting in a final thickness of 550 nm.

2.2.4   Encapsulation of Films

The assembly of the encapsulated films is shown in Figure 2.1. After spin-coating of the perovskite films, the edges of the film (approximately 0.5 cm) were wiped away with methoxyethanol and a cotton swab. PIB edge seal sheets were cut into 2.5×2 cm^2 rectangles, from which a 2×1.5 cm^2 rectangle was cut out from the center. Barrier films were cut to 2.25 $\times$ 1.75 cm^2 rectangles and placed onto glass slides which had a 1 cm hole drilled out from the center. Adhesive PIB edge seal pieces were then placed on top, and pressed with tweezers to hold in place. These barrier/glass slides were then transferred to the glovebox, where perovskite films were pressed onto the PIB edge seal. The films were then placed onto a hot plate at 70 °C,

12

under a mass exerting a pressure of 20 psi to activate the edge seal. After 20 min, samples were removed from the hot plate, and allowed to cool. For samples encapsulated in glass, a 2.5 × 2 cm^2 glass slide was adhered with PIB edge seal directly onto the perovskite film. Additional control (exposed) samples with no barrier were also prepared.

Film Monitoring

Samples were placed into a humidity chamber at 65 °C, 85% relative humidity (ISOS-D-3 testing protocol).[35] Films were removed from the humidity chamber at regular intervals and analyzed via photoluminescence measurements and UV-Vis spectroscopy. Photoluminescence measurements were taken using a Renishaw Raman/micro-PL microscope with a 633 nm excitation laser, 600 l/mm grating. UV-Vis measurements were taken on a Perkin Elmer LAMBDA 1050+ UV/Vis/NIR Spectrophotometer. For each condition, five films were prepared and aged while two films were actively monitored. At the end of the aging test, the encapsulation was removed from films to enable analysis via x-ray diffraction (XRD). XRD measurements were taken using a Rigaku SmartLab diffractometer. Pictures of the films before and after aging for 200 hours are shown in Figure 2.3.
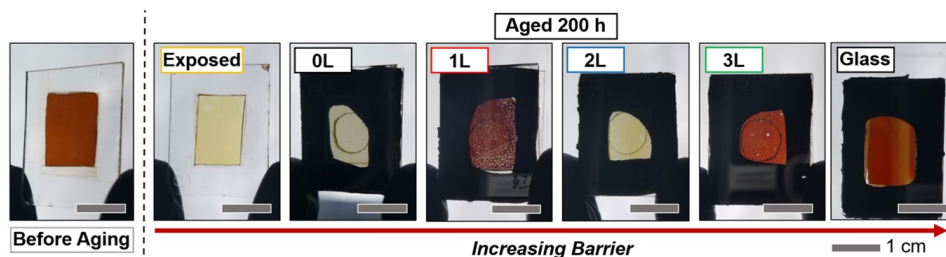
Figure 2.3. Pictures of representative films before and after aging for 200 hours.

2.3 Results and Discussion

The optical absorbance evolution of select perovskite films is shown in Figure 2.4a-c. As seen in Figure 2.4a, the exposed films quickly tended towards optical transparency, retaining only a small amount of absorbance at shorter (purple) wavelengths (and thus appearing

light yellow—see Figure 2.3). This trend is attributed to the degradation to and subsequent outgassing of volatile species (such as methylammonium iodide and HI) from the perovskite film.[58] Figure 2.4b shows the UV-Vis evolution for the 1L-encapsulated films, where the decrease in absorbance was also observed but was less rapid. The 0L, 2L and 3L graphene/parylene samples showed similar behavior. Finally, the glass-encapsulated films (Figure 2.4c) showed minimal variation in absorbance during aging, confirming the quality of the PIB edge seal as well as the strong thermal stability of the perovskite (the glass-encapsulated samples were left to age an additional 800 hours after the remaining samples were removed from the humidity chamber, and still displayed minimal signs of degradation). We observed distinct absorbance profiles between the exposed/0L/2L samples and the 1L/3L samples. The former set showed a marked decrease in absorbance at longer wavelengths, which we attribute to the conversion of perovskite into PbI_2, which is optically absorbent only below 550 nm.[59] The latter set, in contrast, continued to absorb light up to 750 nm throughout the aging test, due to the continued presence of perovskite. These observations are clarified by considering absorbance at 450 nm (where absorbance from the triple cation perovskite, δ-$FAPbI_3$,[60] and PbI_2 are observed) and at 700 nm (which is only absorbed by the perovskite. In Figure 2.4d, the ratio of absorbance between 450 nm and 700 nm are shown as a function of time. Here, the 1L/3L samples retained about 2× more absorbance at longer wavelengths than the 0L/2L samples, which themselves were about 3× more absorbent than the exposed film. Additionally, when the time evolution of absorbance at 700 nm is considered (Figure 2.4e), we observe that 3L retains much more perovskite relative to the other barrier films. However, significant loss is still realized even in the 3L condition.

Figure 2.3, showing photos of the aged film, also mirrors this trend, with the exposed/0L/2L films appearing yellow, compared to the red-colored 1L/3L films (though visually, some spottiness is apparent in the 1L/3L films, indicative of degradation in those films as well). The 2L graphene exhibits worse performance than the 1L due to the handling required to coat the additional graphene layer onto the commercial 1L graphene/parylene (see Figure 2.2), which can

induce defects/tears in graphene.[61] The decrease of performance upon the addition of a second graphene layer was observed across all five films that were aged. Additionally, multiple sets of 2L films prepared from different batches of graphene exhibited diminished performance as confirmed by conductivity and Raman measurements.
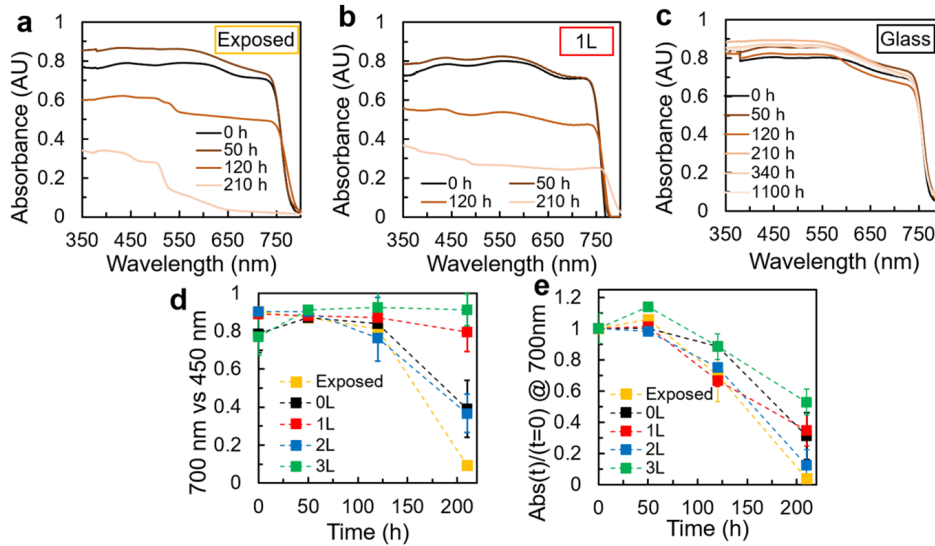
Figure 2.4. UV-Vis tracking during perovskite film aging. a-c) Evolution of UV-Vis spectra for a) exposed, b) 1L, and c) glass-encapsulated films. Remaining UV-Vis spectra are given in Figure 2.5. d) Ratio of absorbance intensity at 700 nm vs 450 nm. (e) Ratio of absorbance intensity at 700 nm at t vs t=0.

To complement the information gained from tracking optical absorbance, we also monitored the films' photoluminescence (PL) behavior over time, which can give insight into the films' optoelectronic properties. These results are shown in Figure 2.6. To improve readability, the evolution of the peak PL intensity (Figure 2.6a-b) and peak PL wavelength (Figure 2.6c-d) have each been split into 2 panels, with the same data from the 1L-encapsulated sample represented in both panels. As shown in Figure 2.6a, all of the graphene/parylene films exhibit an increase in PL over time, despite becoming yellow/spotty during aging (Figure 2.3). In early trials, we considered that this phenomenon could be due to condensation forming on the graphene/parylene barrier, potentially amplifying the PL emissions back to the detector. Thus, in later trials we carefully dried the exposed barrier films with an air gun prior to every PL measurement, and this

15
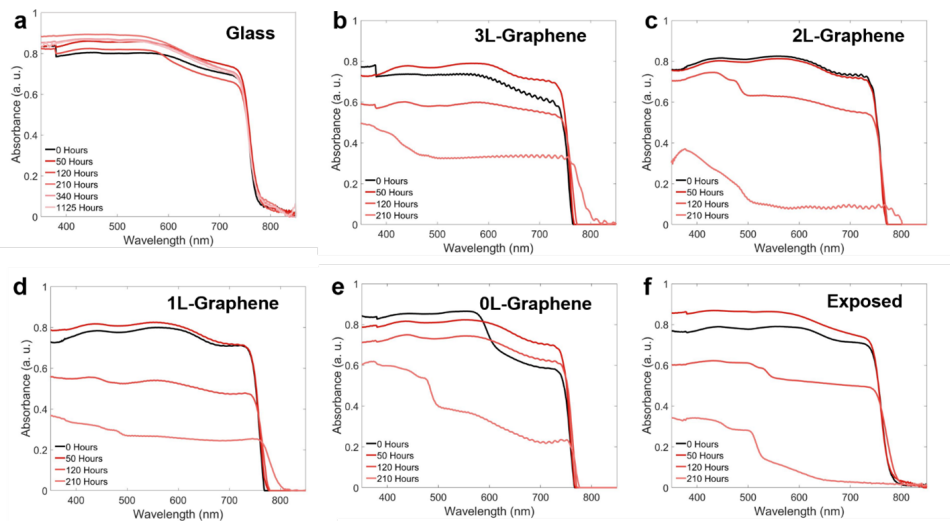
Figure 2.5. UV-Vis evolution of perovskite films encapsulated with a) glass, b) 3L, c) 2L, d) 1L, e) 0L and f) exposed.

phenomenon persisted. In contrast, the exposed films exhibited no photoluminescence under laser excitation by 100 hours, while the glass-encapsulated films showed only a slight increase in PL emission. (Figure 2.6b). In addition, the graphene/parylene-encapsulated samples exhibited a shift in the peak wavelength of PL emissions (Figure 2.6c), a behavior not present in the glass films, and only minimally observed in exposed films (Figure 2.6d).

Further understanding the differences in perovskite decay was achieved via probing the crystallographic properties of the films through x-ray diffraction (XRD). The x-ray diffractograms for our films before and after aging for 200 hours are shown in Figure 2.8a. The glass-encapsulated films remained virtually unchanged compared to films analyzed before aging, in alignment with the trends observed with UV-Vis and PL. In contrast, the graphene/parylene films all exhibited a substantial decrease in intensity of the triple cation perovskite peak at 2θ = 14°, while also gaining a prominent peak at 2θ = 11.5°, corresponding to the hexagonal δ-FAPbI$_3$. The δ-FAPbI$_3$ peak is not seen in either the exposed or glass-encapsulated films; it formed only in the presence of the semi-permeable parylene encapsulation material.

The x-ray diffractograms also allow for qualitative estimation of the relative degree of conversion between triple cation perovskite and δ-FAPbI$_3$ between the graphene/parylene films,
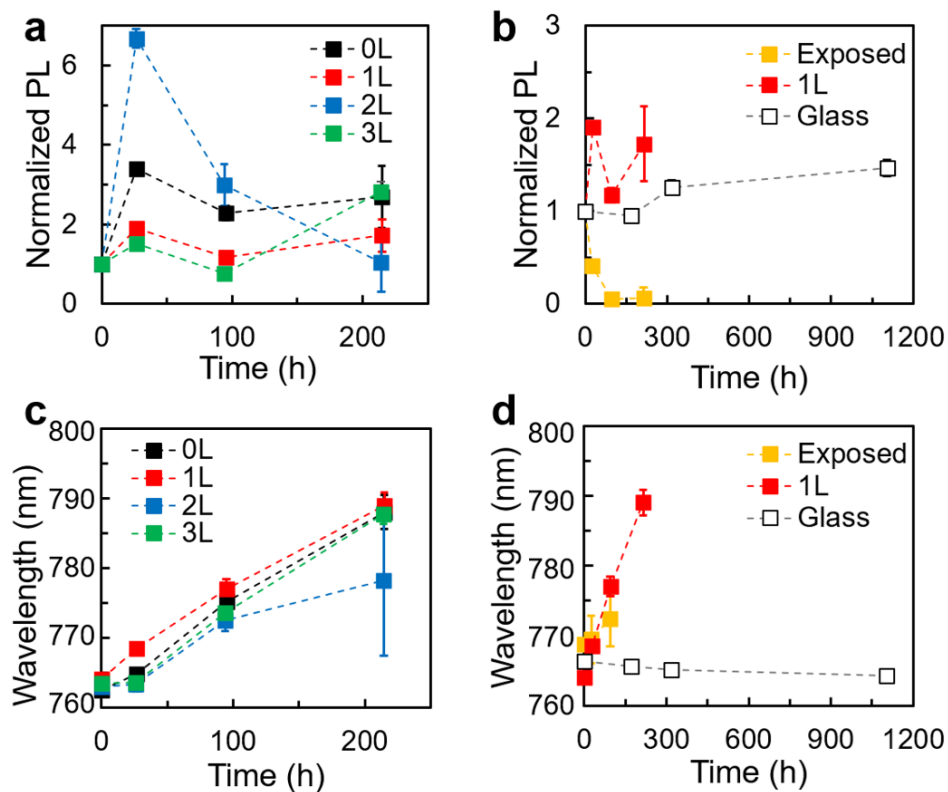
Figure 2.6. Photoluminescence (PL) evolution during aging. a) Normalized average PL evolution for 0, 1, 2 and 3L-graphene. b) PL evolution comparing 1L to glass and control samples. c) Peak PL wavelength evolution for 0, 1, 2 and 3L-graphene. d) Evolution of peak PL wavelength comparing 1L to glass and exposed samples. The complete PL spectra are shown in Figure 2.7
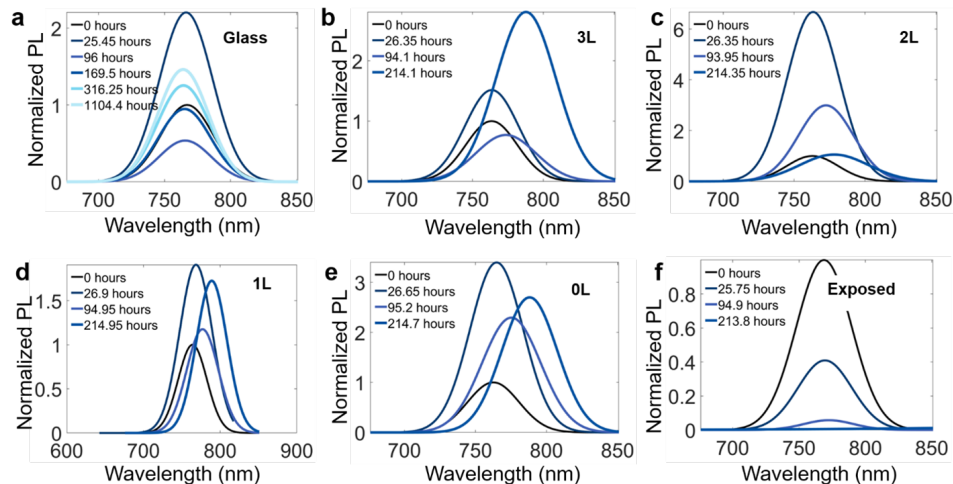
Figure 2.7. Photoluminescence evolution of perovskite films encapsulated with (a) glass, (b) 3L, (c) 2L, (d) 1L, (e) 0L and (f) exposed. Photoluminescence measurements were taken using a Renishaw Raman/micro-PL microscope with a 633 nm excitation laser, 600 l/mm grating, 0.15 second dwell time, 0.1% power, and 8 μm spot size.

by comparing the intensities of the peaks at 14° and 11.5°.[22] This ratio is plotted in Figure 2.8b, and shows the dramatic effect that the addition of graphene conveys to the parylene support layer. While the triple cation perovskite in the 0L graphene has almost completely decayed into δ-FAPbI$_3$, the 1L graphene film has a 15× higher ratio of triple cation to δ-FAPbI$_3$, which itself is nearly doubled again between the 1L and 3L graphene. Meanwhile, the 2L films exhibited worse performance than either the 1L or 3L films, a similar trend as seen via optical absorbance and PL emission. The addition of a 3rd layer of graphene (3L) appears able to negate and improve upon any damaging wrinkles/tears induced by the multi-layer graphene preparation.

These observations suggest that our set of films have undergone three unique degradation pathways. The first, seen in the exposed films, is the degradation of the triple cation perovskite into PbI$_2$,[62] along with the expulsion of all volatile species. The second, observed in the glass-encapsulated samples, is a slow thermal anneal due to the elevated temperature (85 °C) of the humidity chamber used for the accelerated decay test. The effect is a reduction of non-radiative recombination centers (leading to a slight PL increase) without changes to the chemical composition of the films, as there is no pathway for species ingress/egress. The final degradation
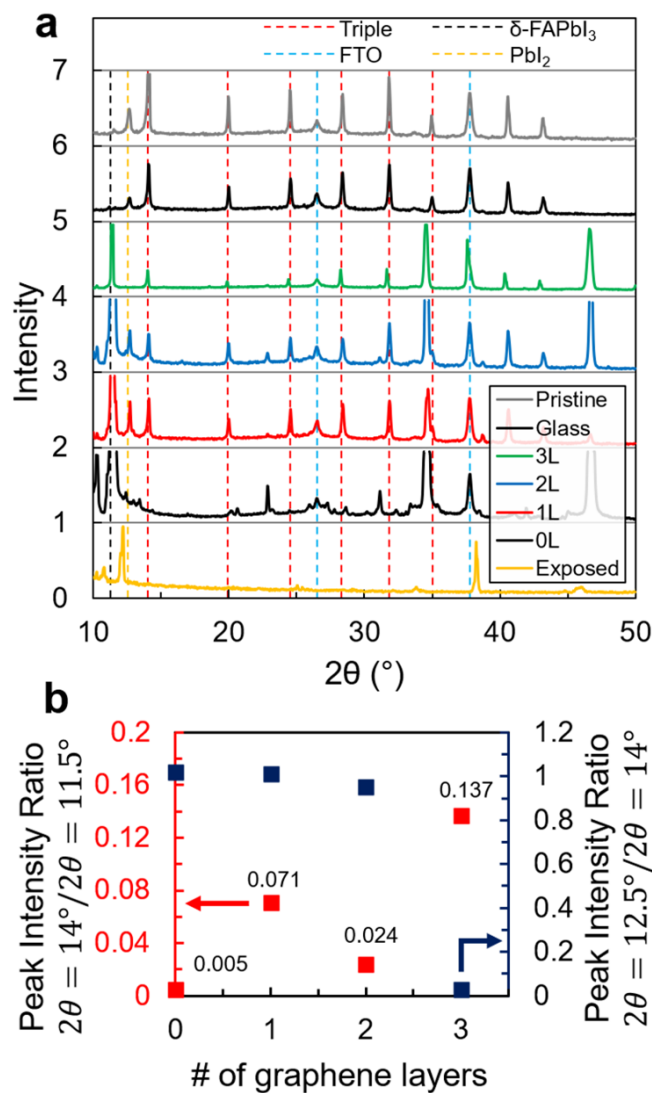
Figure 2.8. XRD analysis of perovskite films. (a) XRD diffractograms for films before and after aging. (b) Ratio of peak intensity of triple cation perovskite ($2\theta = 14°$) to peak intensity of δ-FAPbI$_3$ ($2\theta = 11.5°$) and PbI$_2$ peak intensity ($2\theta = 12.5°$) as a function of number of layers of graphene.

pathway observed, seen in the graphene/parylene films, is the phase segregation and formation of multiple perovskite phases, particularly iodide-rich and bromide-rich domains. This is exhibited by the increased and red-shifted PL profile, which is attributed to the iodine-rich phases acting as a carrier sink.[63] Additionally, photoinactive phases (such as δ-FAPbI$_3$ and potentially I$_2$[62]) are forming, due to the ingress of oxygen and water.[64]
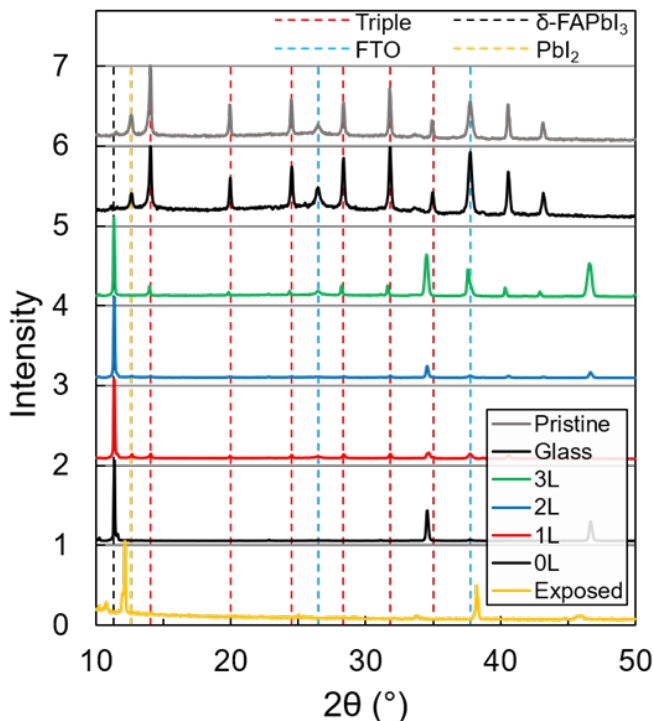
Figure 2.9. XRD diffractograms for films before and after aging. Spectra are identical to those in Figure 2.8a but here they have been normalized to their strongest peak, allowing for visual observation of the relative intensities of $2\theta = 11.5°$ (δ-FAPbI$_3$) and $2\theta = 14°$ (triple perovskite) peaks (at the detriment of visualization of many other peaks in the diffractograms).

More detailed analysis of the graphene barriers, separate from the perovskite films, was carried out in order to validate our findings. Figure 2.12a shows the sheet resistance of the graphene films. The increasing conductivity as each layer is added, as well as overall magnitude of sheet resistance, are consistent with previous reports.[50] The average optical transmissivity of the films (Figure 2.12b) likewise shows a successive change with each layer added, further confirming successful transfer. In contrast, air permeability measurements (Figure 2.12c, appara-
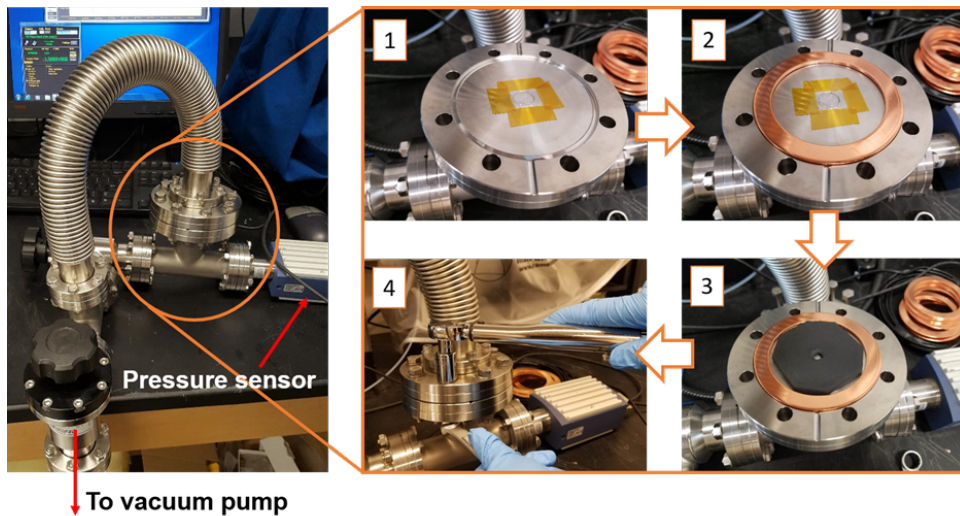
Figure 2.10. Schematic overview of isochoric gas permeability apparatus. 1) The barrier material is adhered with Kapton tape over the sintered porous opening in the flange. 2) A single-use copper gasket is placed on the flange. 3) A rubber spacer with a circular hole (6 mm diameter) is placed over the barrier. The spacer provided additional support to the barrier film and prevented it from tearing when subjected to vacuum. 4) The upper flange is attached, and the system is bolted and tightened. The entire system is pumped down to vacuum, after which the upper half of the system is slowly brought back up to atmospheric pressure. The pressure sensor (Inficon) tracks the pressure increase over time, which is recorded with the TGaugeExpress software.
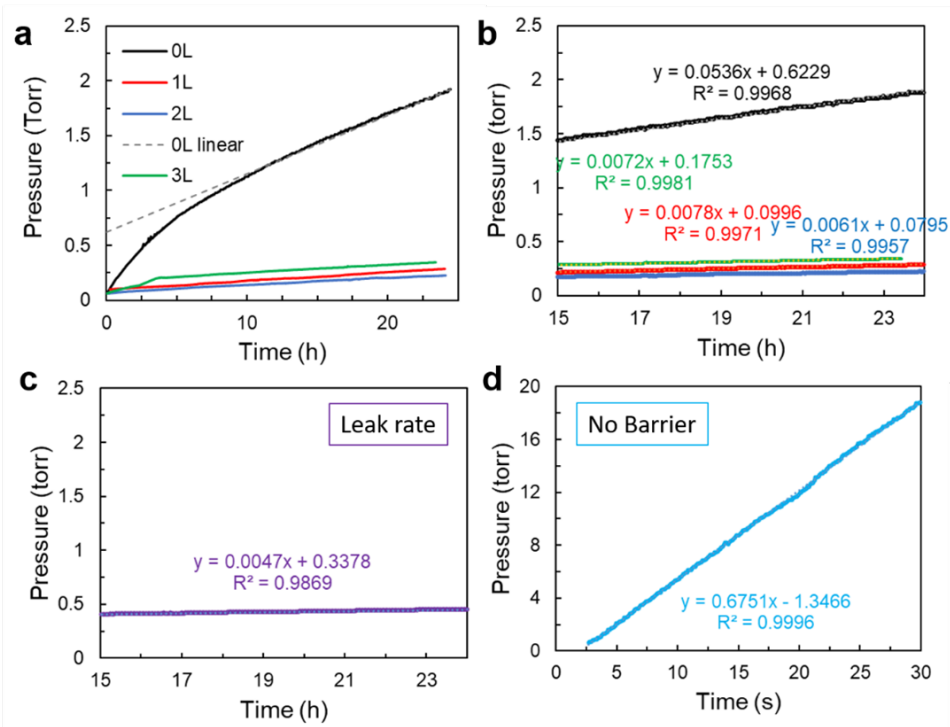
Figure 2.11. a) Measurement of pressure change over time for graphene barriers. b) Linear regions of pressure change, with slope shown in units of torr/hr. c) Measurement of leak rate of system. d) Measurement of intrinsic resistance of air permeation using no barrier (slope shown in units of torr/s).

tus shown in Figure 2.10-2.11) show a large (15×) decrease between 0L and 1L, followed by

smaller variations from 1L to 2L to 3L. Notably, the difference between the permeability of 0L

vs 1L films is identical the difference in ratio of the triple cation perovskite/δ-FAPbI$_3$ shown

in Figure 2.8b. Meanwhile, the minimal variations in air permeability between the single- and

multi-layer graphene barriers are in sharp contrast to the varied perovskite degradation observed,

with 2L films decaying substantially compared to 1L and 3L films.
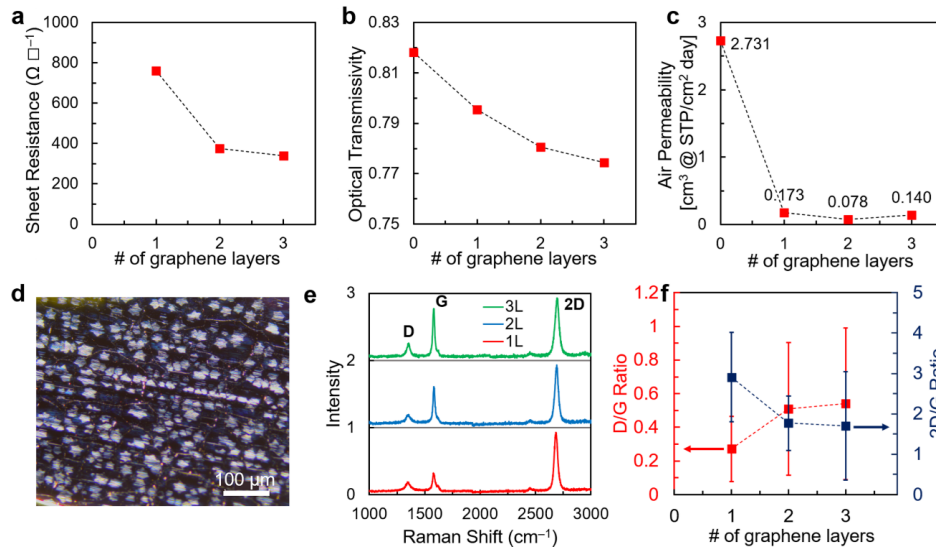
Figure 2.12. Analysis of single- and multi-layer graphene barrier films. a) Sheet resistance
of films as a function of number of layers (0L films produced an open circuit). b) Average
optical transmissivity (extracted from Figure 2.2b). c) Air permeability of films, found using
an isochoric gas permeability apparatus. d) Optical micrograph of 1L graphene, as received. e)
Representative Raman spectra of 1L, 2L and 3L graphene films. f) Average D/G and 2D/G ratio
for graphene films.

To investigate this discrepancy, spatial mapping using Raman was conducted in order

to analyze the quality of the graphene films and spatial resolution(Figure 2.13-2.14). We note

that Raman analysis cannot be done directly on the parylene films, whose spectra overwhelm the

graphene signal, and must instead be measured following water transfer onto a silicon substrate.

The overlain spectra for 30 measurements for 1L graphene show a wide range of graphene

quality, and numerous traces show minimal or no graphene signal. Indeed, the spatial coverage of

transferred graphene was less than 50% for both 1L and 2L films, coupled with large variability

in the 2D/G ratio (Figure 2.8), which gives information regarding the number of monolayers of graphene.[65] Several factors likely influence the lack of uniformity and variability in coverage of the graphene films. First, nanoislands and macroscopic regions of multilayer graphene are commonly found on CVD-grown graphene (see Figure 2.12d), and are formed via nucleation from silica or other impurities within the copper foil on which it is grown;[66,67] thus, a uniform monolayer of graphene is unlikely to be present in the 1L films to begin with. Additionally, the water transfer method for layer-by-layer growth of multilayer graphene is easily susceptible to wrinkling and tearing.[61] Although previous work by Yoon et. al. on multilayer graphene films (prepared via the same method as our own films) claims that that strong van der Waals forces between graphene layers can fully suppress lateral diffusion of air molecules,[68] the authors note that in cracked regions, air molecules will indeed diffuse laterally, allowing them to access adjoining grain boundaries and pinholes and permeate vertically through the film. We note that a graphene grain boundary typically refers to a tilt grain boundary comprised of 5- and 7-membered rings,[69,70] through which small species are able to permeate.[71] The wide variability in graphene uniformity and coverage in our multilayer (i.e. 2L and 3L) films will therefore result in highly variable barrier properties over a large area. Given the penalties of increased process complexity and materials cost of each successive layer of graphene used, compared to the small improvement in perovskite film stability shown between 1L and 3L graphene, we conclude that 1L graphene may offer the best combination of properties for use in flexible, optically transparent barrier applications for perovskite films. Beyond single- and multi-layer graphene, other 2D materials may prove to be intriguing for similar encapsulation applications. As an example, graphene oxide also exhibits good barrier performance against air and water,[72] although thickness would need to be carefully controlled to retain optical transmissibility.[73] Meanwhile, hexagonal boron nitride has recently emerged as a promising new 2D material and exhibits excellent transparency due to its wide bandgap,[74] although it tends to have smaller grains than CVD graphene,[75] which could exacerbate the leakage issues we observed.

1L — D/G Ratio heatmap

	1	2	3	4	5	6
1	0.03151	0.05155	0	0.3186	0.2076	0
2	0.2335	0	0	0.7326	0	0
3	0	0.2413	0	0.2632	0	0
4	0	0.4665	0	0	0	0
5	0	0.1994	0	0	0.2493	0

Average = 0.272

2L — D/G Ratio heatmap

	1	2	3	4	5	6
1	0	1.107	0.1198	0	0.1812	0
2	0	0	0.1461	0	0	1.141
3	0	0	0	0	0	0
4	0.4065	0.4268	0	0	1.024	0
5	0.3456	0.5759	0.1996	0	0	0

Average = 0.51

3L — D/G Ratio heatmap

	1	2	3	4	5	6
1	0.6248	0	0	0.08637	1.23	0
2	0.7515	0	1.164	0	0	0
3	0	1.267	0.3808	0.2292	0	0
4	0	0.03428	0	0	0	0
5	0.03896	0	0.1667	0.5638	0.5	0

Average = 0.54

1L — 2D/G Ratio heatmap

	1	2	3	4	5	6
1	1.511	0	0	1.596	2.452	0
2	5.011	0	0	3.972	0	0
3	0	3.422	0	2.495	0	0
4	0	3.351	0	0	0	0
5	0	2.003	0	0	3.359	0

Average = 2.91
Coverage = 36%

2L — 2D/G Ratio heatmap

	1	2	3	4	5	6
1	0	1.107	0.1198	0	0.1812	0
2	0	0	0.1461	0	0	1.141
3	0	0	0	0	0	0
4	0.4065	0.4268	0	0	1.024	0
5	0.3456	0.5759	0.1996	0	0	0

Average = 1.77
Coverage = 36%

3L — 2D/G Ratio heatmap

	1	2	3	4	5	6
1	1.135	0.9398	3.904	0.9389	0.85	1.027
2	0.6457	1.821	0	0	1.399	3.134
3	0.6995	1.403	2.482	2.878	6.261	1.549
4	0	1.695	0.04084	1.121	0	0.5545
5	1.152	0	1.084	1.296	2.797	0

Average = 1.70
Coverage = 80%

Figure 2.13. Heatmaps showing spatial coverage of graphene on 1L, 2L and 3L films. Squares marked "0" indicate that no graphene was detected in the measurement. The measurement settings were: 8 μm spot size, 10 μm step size (5 x 6 grid or 30 spectra total), 514 nm laser.
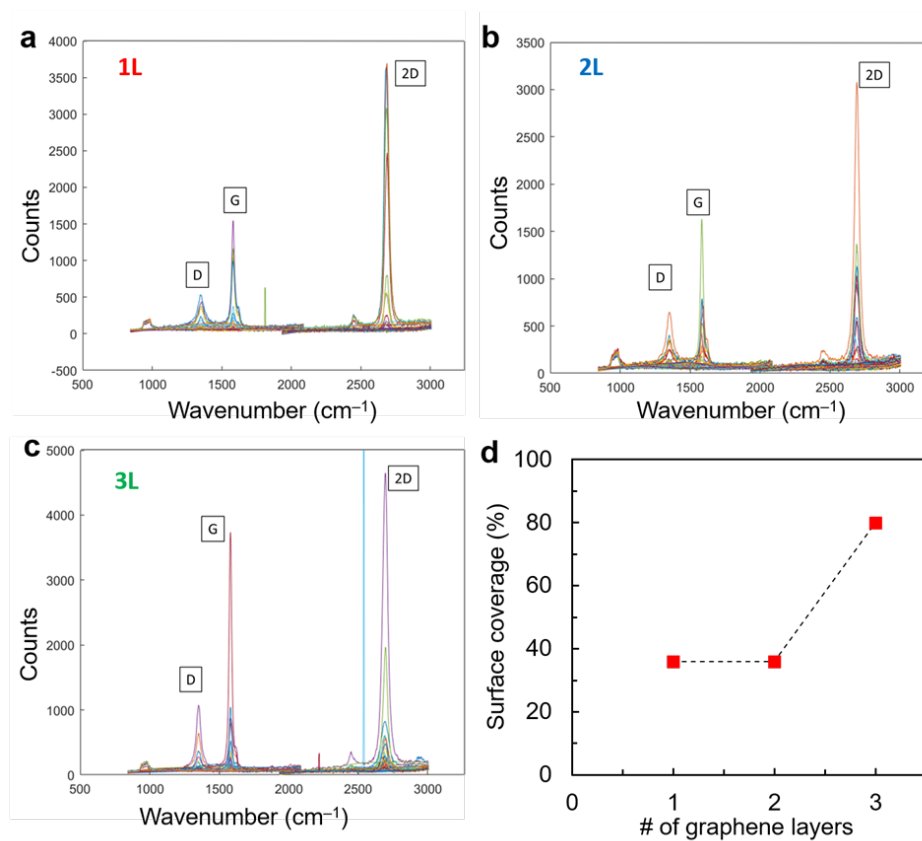
Figure 2.14. Overlain Raman spectra for a) 1L, b) 2L and c) 3L graphene films, transferred to Si. d) Surface coverage as calculated by % of measurements with nonzero 2D/G ratio.

26

2.4 Conclusions

Experimental results show that single-layer graphene can confer substantially improved barrier performance to a polymeric support film, with multi-layer (at least 3L) graphene yielding further improved barrier performance. We emphasize that 2L graphene exhibited worse performance as an encapsulant than 1L graphene, most likely due to defects introduced during manipulation of the films. Nevertheless, all of our graphene/parylene-encapsulated films showed substantial degradation compared to glass-encapsulated films, suggesting that for rigid, non-flexible, long-lasting applications, the addition of graphene to a semi-permeable flexible polymer barrier is insufficient for generating a highly stable device. While modifications to the preparation procedure of the multi-layer graphene could result in improved barrier performance, the numerous grain boundaries in CVD graphene still result in a bulk material that is far from attaining the "impermeable" status of glass or molecular graphene. Still, the substantial improvement obtained from the addition of a single layer of graphene to our polymer support layer makes graphene-based barriers a compelling potential encapsulant for lightweight and/or flexible perovskite solar cells.

Chapter 2, in full, is a reprint of the material "Stability of Perovskite Films Encapsulated in Single- and Multi-Layer Graphene Barriers" by Rory Runser, Moses Kodur, Justin H. Skaggs, Deniz N. Cakan, Juliana B. Foley, Mickey Finn III, David P. Fenning, and Darren J. Lipomi as it appears in ACS Applied Energy Materials. The dissertation author was the first author of this paper, all authors contributed to this work.

Chapter 3

Electrochemical Screening of Contact Layers for Metal Halide Perovskites

3.1   Introduction

High performance metal halide perovskite (MHP) photovoltaic devices ubiquitously employ heterostructure architectures where photogenerated charges are separated by carrier selective contacts.[76–78] A primary strategy to improve device efficiency is rooted in the development of carrier selective transport layers to control carrier extraction and process compatibility for a given perovskite composition.[79–88] For example, the electron selective transport layer (ESL) is chosen to minimize non-radiative recombination rates at the interface, align its conduction band minimum (CBM) with that of the absorber, and create a dense layer that minimizes leakage currents.[89,90] These properties are typically investigated by a suite of techniques including photoemission spectroscopy (PES), which is especially useful to determine the valence band maximum (VBM), surface chemistry, and fundamental relationships between the two.[91,92] Electrochemical techniques can provide similar, albeit indirect, information about these properties and have the advantage of being inexpensive, accessible, and compatible with large area or high throughput studies.[93–95] These characteristics make electrochemical measurements effective for transport layer development, monitoring process reproducibility, and implementing quality control, particularly at an industrial scale where the ultra-high vacuum requirements of PES complicate its implementation. Electrochemical characterization tools have been implemented

to study other photovoltaic materials and devices, such as organic photovoltaics[96–99] and dye-sensitized solar cells,[100–103] but application to perovskites, and more specifically to perovskite solar cells, has been limited.[79, 82, 104] Here, we correlate electrochemical characteristics of a SnO_x transport layer directly with perovskite photovoltaic performance parameters, demonstrating the utility of electrochemical probes for designing and characterizing perovskite photovoltaics.

In this work, we highlight the utility of electrochemical probes to rationalize the optimization of metal oxides for ESLs in optoelectronic devices.[105] Specifically, we use this approach to understand interface chemistry and energy level alignment dictated by processing dependencies of a vacuum thermally-evaporated SnO_x (VTE-SnO_x) ESL used as the superstrate contact for MHP solar cells. We find that the cyclic voltammetry (CV) characteristics of the VTE-SnO_x layers in an aqueous ferri-/ferrocyanide ($Fe[CN]_6^{3-/4-}$) electrolyte correlate to the final performance of the devices. In particular, the cathodic onset potential at which the current for the complexed Fe^{3+} to Fe^{2+} reduction "turns on" is related to the processing-dependent electron transfer of the VTE-SnO_x and correlates to the solar cell open-circuit voltage (V_{OC}). Additionally, anodic sweeps directly probe electronic current leakage pathways irrespective of their origin (defects, pinholes, conductive filaments, impurities, etc.), and the magnitude of this loss mechanism is reflected in the short-circuit current density (J_{SC}). Finally, to show how these properties are affected by the VTE-SnO_x chemistry, we present potentiostatic chronoamperometry in an aqueous methylammonium iodide electrolyte where proton-assisted reduction of Sn^{II} defects to Sn0 occur at the surface of the VTE-SnO_x at -1.0 V versus Ag/AgCl. For optimally-annealed VTE-SnO_x with more complete conversion to Sn^{IV}, reduction to Sn0 does not onset until more cathodic potentials ($<$ -1.3 V versus Ag/AgCl), in agreement with O:Sn ratios determined by X-ray photoemission spectroscopy (XPS). Thus, the electrochemical techniques provide key empirical information to optimize transport layer processing.

Importantly, these insights are provided prior to device completion and adaptable to high-throughput experimentation or large areas, making them viable for quality control, which we demonstrate by analyzing a 100 cm^2 VTE-SnO_x ESL Many processing approaches compatible

with the electrochemical methods described here have been demonstrated for SnO_x in the literature, including spin-coat,[29, 106] chemical bath deposition,[107, 108] atomic layer deposition,[109–111] thermal evaporation,[112, 113] and sputtering.[114, 115] Using the electrochemical measurements described in this manuscript provides a rapid and straightforward means to screen newly-developed transport materials and assists in their co optimization with active layer processing to ensure high yield and high performance critical for the commercialization of MHP-based photovoltaics and related optoelectronic devices.

3.2   Materials and Methods

3.2.1   Substrate Preparation

Fluorine-doped tin oxide (FTO) substrates were purchased from Greatcell Solar Materials (TEC15, 15Ω/sq) and then cleaned by sonicating in 2 vol% Hellmanex III in DI water for 15 minutes, rinsing with DI water, sonicating in DI water for 15 minutes, rinsing with DI water, sonicating in IPA (99.5% purity) for 15 minutes, rinsing with IPA, sonicating in acetone (99.9% purity) for 15 minutes, rinsing with IPA, and then drying with filtered air.

3.2.2   Tin Oxide (SnO_x) Deposition

SnO_x nano powder bought from US Research Nanomaterials (99.7% purity, 35-55 nm) was thermally evaporated onto FTO substrates in an alumina-coated tungsten boat under vacuum (at least 6 x 10^{-6} mTorr) at a rate of 0.05-20 Å/s. Immediately prior to deposition, FTO substrates were plasma treated in air for 10 minutes at 300 mTorr. After deposition, the SnO_x films were annealed in air for 1 hour at temperatures from 180-200°C in a box furnace.

3.2.3   Electrochemical Measurements

A standard three-electrode electrochemical setup was used for cyclic voltammetry, electrochemical impedance spectroscopy, and chronoamperometry (Figure 3.1). A 0.5M KCl electrolyte in 18.2 MΩ-cm DI water with 1.0 mM $K_3Fe(CN)_6$, and 1.0 mM $K_4Fe(CN)_6$ was

used for the cyclic voltammetry, electrochemical impedance spectroscopy, and chronoamperom-etry to analyze surface coverage. A single junction silver chloride (AgCl) reference electrode (Pine Research, RREF0021) in saturated potassium chloride (KCl) and a standard platinum (Pt) counter electrode (Pine Research, 99.99%, RRPG249PT) were used as the reference and counter electrodes, respectively. All voltages reported were corrected with 85% automatic and 15% manual iR compensation. All electrochemical measurements were performed on a Biologic VSP 300 potentiostatic with EC-lab software.
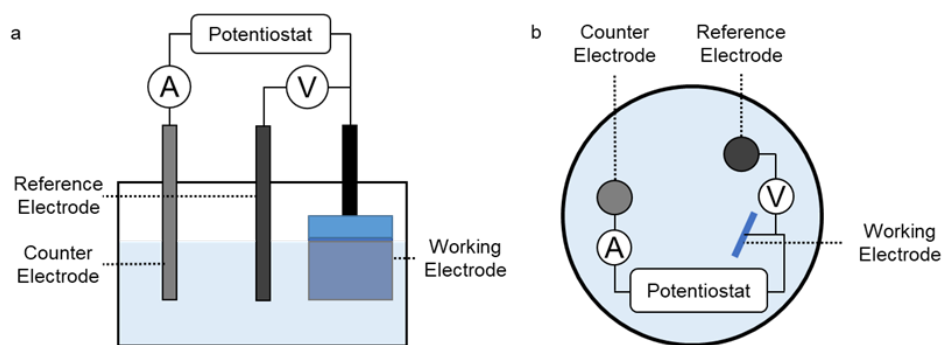
Figure 3.1. a) Cross-sectional view of the 3-electrode system utilized throughout this work. In all cases, a Ag/AgCl reference electrode and platinum counter electrode were used. b) Top view of the same apparatus and schematic of external measurement circuit.

To avoid error in measurements, the counter electrode (CE) should be an inert conductor. Additionally, the surface area of the CE should be much larger (at least 10x) than the surface area of the working electrode (WE). This prevents the half-reaction occurring at the CE from becoming limiting. The reference electrode should be placed near the working electrode to minimize voltage losses due to uncompensated electrolyte resistance and thus provide a more accurate measurement. Even so, some voltage loss will be realized and require iR correction as described above.[116]

In cyclic voltammetry, the films were scanned 5 times at which point we they stabilized with minimal differences between scans 4 and 5. The scan rate was 20 mV/s. Mott-Schottky analysis was performed following Step Potential Electrochemical Impedance Spectroscopy (SPEIS), run from -0.2 to 1.2 V vs. Ag/AgCl at frequencies ranging 1-11 kHz. Due to the high

doping level in the SnO_x ($> 10^{18}$ cm^{-3}), a correction for the Helmholtz layer was applied to isolate the space charge capacitance.[117] In the chronoamperometric measurements to determine pore density, the films were held at 0.4 V vs. Ag/AgCl for 30 seconds after a 1 second linear sweep from open-circuit voltage.

3.2.4   Device Fabrication and Current Voltage Characterization

All photovoltaic devices were completed with a triple cation perovskite with solution stoichiometry $FA_{0.79}MA_{0.16}Cs_{0.05}Pb$ ($I_{0.84}Br_{0.16}$)$_3$, spiro-OMeTAD (2,2,7,7-tetrakis[N,N-di-p-methoxyphenylamino]-9,9-spirobifluorene), and Au following procedures based on Correa-Baena et. al.[118] Modifications to the reported process include: a) the [PbI$_2$]:[FAI] and [PbBr$_2$]:[MABr] ratios were fixed at 1:1.09, b) the perovskite films were annealed for 45 minutes at 100°C in a nitrogen filled glovebox, and c) the spiro-OMeTAD layer was not doped with FK209 but rather oxidized in dry air for 24 hours prior to gold evaporation. FAI and MAI were purchased from GreatCell Solar Materials, CsI (99.999% purity) from Sigma Aldrich, lead iodide (99.99% purity) and lead bromide (99.99% purity) from TCI, spiro-OMeTAD (purity $>$ 99.5%) from LumTec, and gold from Lesker.

Devices were tested in ambient atmosphere, in a Newport-Oriel Class A solar simulator, under AM 1.5G, at 100 mW/cm^2, with a scan speed of 0.1V/s, and a fixed aperture of 0.07 cm^2. Prior to testing, the light intensity was calibrated using a silicon reference cell.

3.2.5   Chronoamperometry (CA) / Reactivity Measurements

The CA measurement uses the same electrochemical set-up as described above in the Electrochemical Measurements section, but with an aqueous 0.1M MAI electrolyte. For the CA measurements, the films were held at potentials between -1.3 and -1.1 V vs Ag/AgCl for 5 minutes and the current response was collected.

3.2.6 X-ray Photoemission Spectroscopy (XPS)

XPS on 25 nm VTE-SnO$_x$ films annealed at different temperatures was performed at the Irvine Material Research Institute utilizing their Kratos AXIS-Supra. These measurements were done normal to the sample surface with a monochromatic Al K source at vacuum levels below 5 x 10^{-8} Torr. The pass energy for survey scans and detailed spectra was 160 eV and 20 eV, respectively, while the step size was 1 eV and 0.1 eV, respectively. XPS on electrochemically degraded films were performed at the CMMR Materials Research Facility at UC San Diego on a PHI Quantera Scanning XPS. These measurements were done normal to the sample surface with a 50 W Al K source at vacuum levels below 9.1 x 10^{-9} Torr. The pass energy for survey scans and detailed spectra was 280 eV and 26 eV, respectively, while the step size was 0.25 eV and 0.05 eV, respectively. Due to instrument limitations, the binding energy axis for all scans, unless otherwise noted, was calibrated using the average location of the C 1s C-C spectral feature across each sample set such that all binding energy axes remained fixed relative to each other (a uniform shift was applied to each sample set). Spectra taken with the Al source are typically assigned an uncertainty of 0.05 eV. Spectra taken with UPS are typically assigned an uncertainty of 0.025 eV. Compositional analyses are typically assigned an uncertainty of 5%.

3.3   Results and Discussion

3.3.1   Solar Cell Screening Via Cyclic Voltammetry

First, we demonstrate that CV in an electrolyte containing a reversible redox couple can be used to screen selective contacts (here VTE-SnO$_x$) for their suitability in MHP devices. In these measurements, thin-films of VTE-SnO$_x$ deposited on fluorine-doped tin oxide (FTO) substrates are placed in a 1.0 mM solution of the ferri-/ferrocyanide outer-sphere redox couple with a 0.5 M KCl supporting electrolyte, resulting in the formation of a semiconductor-electrolyte junction, as shown in Figure 3.2a (also see Figure 3.1). Without the VTE-SnO$_x$, the cyclic voltammogram on the bare metallic FTO electrode exhibits the classic duck-shaped curve of a

reversible redox couple (Figure 3.2b).[4] In contrast, the band-bending induced in the VTE-SnO$_x$ (Figure 3.2a) leads to a sharp cathodic onset (Figure 3.2b). The cathodic onset shifts to more cathodic potentials with an increase in post-deposition annealing temperature from 180 to 200°C. These trends are representative of changes observed over a wider set of process variations shown inFigure 3.2c. Of process variations, annealing temperature had the strongest impact on the cathodic onset and thus V$_{OC}$, with a positive correlation between the two.
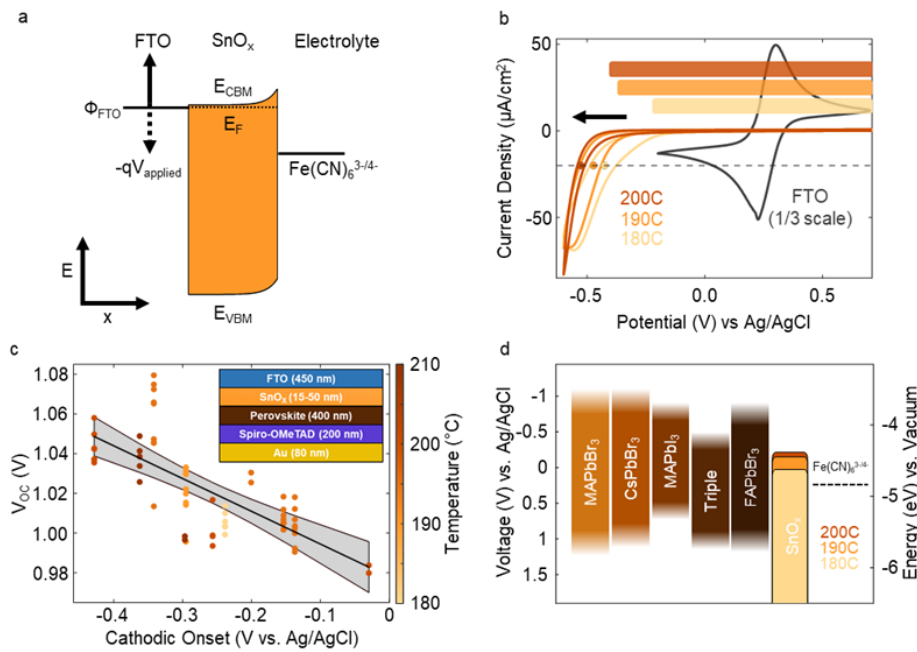
Figure 3.2. a) Schematic energy band diagram of the semiconductor-electrolyte junction formed between n-type VTE-SnO$_x$ and a ferri-/ferrocyanide redox couple in solution. b) Cyclic voltammograms (CV) of VTE-SnO$_x$ films annealed between 180 and 200°C show the blocking nature of the wide-gap VTE-SnO$_x$ until a large enough negative potential enables electron transfer from the VTE-SnO$_x$. For comparison, a CV of a bare FTO substrate, at one third scale, is shown (gray). The flat-band potential of each film is shown above the CV. c) The VOC of devices with varying VTE-SnO$_x$ is correlated with the cathodic onset potential extracted from CV, with a 95% confidence interval shown (device architecture in inset). The color bar indicates the post-deposition anneal temperature. For devices, the perovskite has a nominal stoichiometry of Cs$_{0.05}$FA$_{0.79}$MA$_{0.16}$Pb(I$_{0.84}$Br$_{0.16}$)$_3$. d) A schematic alignment of the band edge positions of common perovskite chemistries compared with the flat-band voltages of the VTE-SnO$_x$ temperature series.[2,3] The dotted line indicates the standard redox potential of ferri-/ferrocyanide. From literature, this triple cation perovskite has a nominal stoichiometry of Cs$_{0.08}$FA$_{0.78}$MA$_{0.14}$Pb(I$_{0.86}$Br$_{0.14}$)$_3$.

The onset potential of cathodic current is directly related to the VTE-SnO$_x$ chemistry and associated energetic alignment, which will impact the formation of the perovskite/ESL interface and ultimately correlates to the V$_{OC}$ of completed devices. Figure 3.2c shows the relationship between the cathodic onset voltage (defined as the potential at which current density = 20 μA/cm^2) and V$_{OC}$ of a completed FTO/VTE-SnO$_x$/FA$_{0.79}$MA$_{0.16}$Cs$_{0.05}$Pb(I$_{0.84}$Br$_{0.16}$)$_3$/2,2',7,7'-tetrakis[N,N-di-p-methoxyphenylamino]-9,9'-spirobifluorene (spiro-OMeTAD)/Au device stack for several experiments with systematic variations made to the VTE-SnO$_x$ ESLs including thickness (10-50 nm), anneal temperature (180-210°C), and deposition rate (0.05-0.20 Å/s). The variability seen in the data set of Figure 3.2c illustrates that the reproducibility of the VTE-SnO$_x$/perovskite interface may be affected by multiple uncontrolled parameters in the processing of the VTE-SnO$_x$, such as ambient humidity and temperature.[119–122] A simple linear model fit to the data indicates with p-value ¡ 10^{-4} that a non-zero slope exists relating V$_{OC}$ to the cathodic onset potential. Despite this scatter, for the procedure used here, we observe that the post-deposition anneal temperature is the most sensitive tested processing parameter to manipulate the cathodic onset potential. Moreover, we find that regardless of the method used to define the onset potential,[123] the trend between V$_{OC}$ and the cathodic onset is consistent (Figure 3.3 and Figure 3.4). Additionally, by comparing the results of CV to the flat-band potentials indicated by the horizontal bars in Figure 3.2b (determined by capacitance-voltage analysis of electrochemical impedance spectra, Figure 3.5), we confirm that changes in the cathodic onset potential trend with the flat-band potential of VTE-SnO$_x$. Moreover, capacitance voltage measurements indicate carrier concentration decreases from 10^{19} to 2×10^{18} cm-3 with increasing annealing temperature from 180 to 200°C (Figure 3.6). All films thus remain degenerately n-type. The resulting flat band potential is nearly equal to the CBM (Figure 3.7). Thus, the changes in the flat-band position correspond to a change in the CBM of the VTE-SnO$_x$ that occurs as the film is annealed in air. The qualitative energetic alignment is shown inFigure 3.2d alongside energy levels reported for various perovskite compositions including the "Triple" cation composition used in our devices.[2,3] Therefore, CV measures the combined effect of multiple electronic properties that dictate charge

transfer at the interface, serving as a time-efficient early diagnostic for an improved interface (e.g. band alignment) between the ESL and perovskite absorbers.
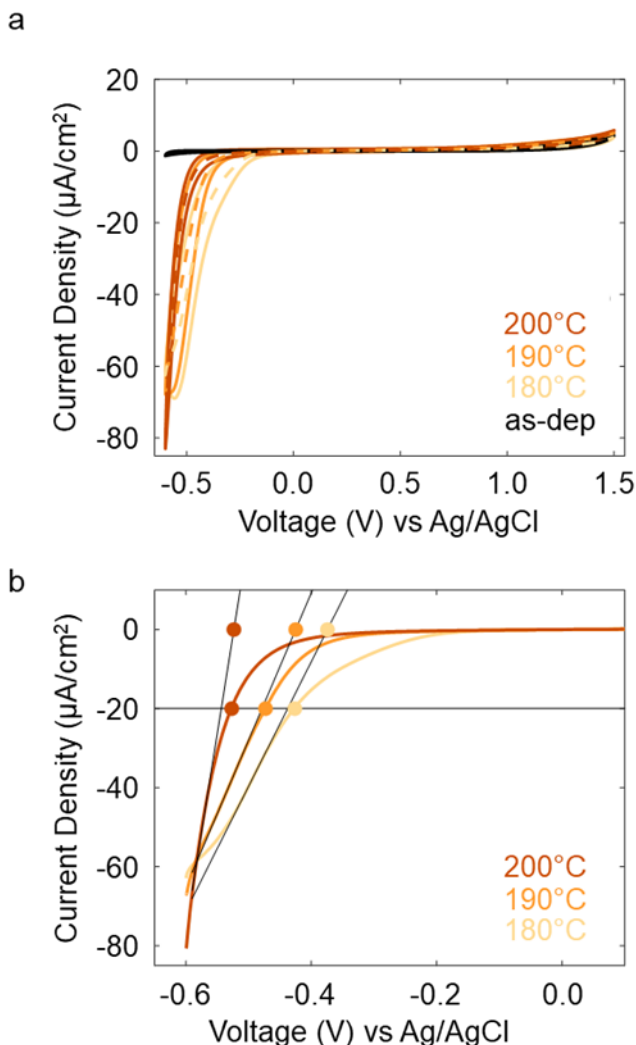
Figure 3.3. a) Cyclic voltammograms (CV) of SnOx films without post-anneal (as-dep) and annealed from 180-200°C. Dashed lines are the averaged curve to account for capacitance. b) The averaged CV curves showing two methods of defining cathodic current onset—either by reaching a current threshold (-20 μA/cm^2 in this case) or by fitting the linear portion and finding the x-intercept. Extracted potentials are shown in Figure 3.4.

We further leverage insight from the anodic portion of the CV, which serves as a measure of undesirable leakage currents, agnostic to their origin, and relates to J_{SC}. For example, in Figure 3.10a, cyclic voltammograms show that VTE-SnO$_x$ films of increasing thickness exhibit
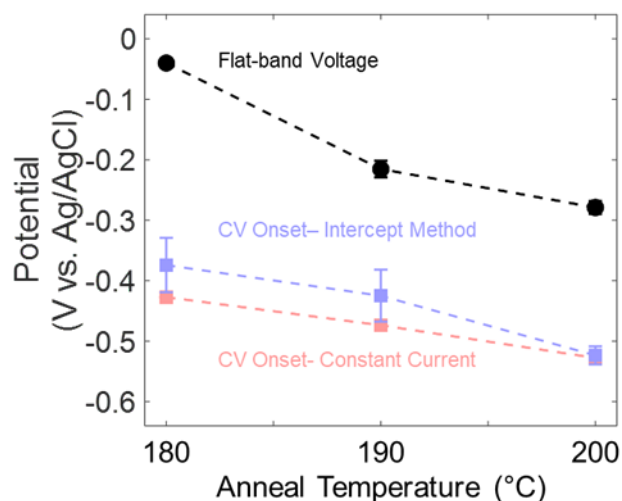
Figure 3.4. Comparison between CV onset definitions as stated in Figure 3.3 (voltage when current matches -20 μA/cm^2 or finding x-intercept of linear portion of the curve) and the flat-band voltage from capacitance-voltage analysis. As can be seen, the trends remain consistent regardless of method used.

reduced anodic current. In perfect hole-blocking films there would be no anodic hole current because of the lack of states available for charge transfer. However, whether by charge transfer with the FTO at pinholes, via conductive filaments, or other defects (inset schematic Figure 3.10a), small hole currents can pass through the film. We further analyzed and attempted to quantify the pinhole density using chronoamperometry. (Figure 3.8) These small current pathways are also evidenced by anodic leakage current in CV and reduce the selectivity of the contact, thereby negatively affecting current collection and the J_{SC} of completed devices (Figure 3.10b). These data also a possess a p-value ¡ 10-4 demonstrating a statistical correlation between J_{SC} and the anodic current.). Additionally, we find that the shunt resistance is negatively correlated with the anodic current. (Figure 3.9) Note the 50 nm thick VTE-SnO$_x$ films in Figure 3.10b display variation in anodic leakage current magnitude and do not necessarily provide the lowest leakage currents, evidencing that processing parameters other than thickness must be considered to minimize anodic currents. ETL thickness modulated the leakage current the most of test process parameters, with intermediate thicknesses of about 20-30 nm producing the highest J_{SC}.

37
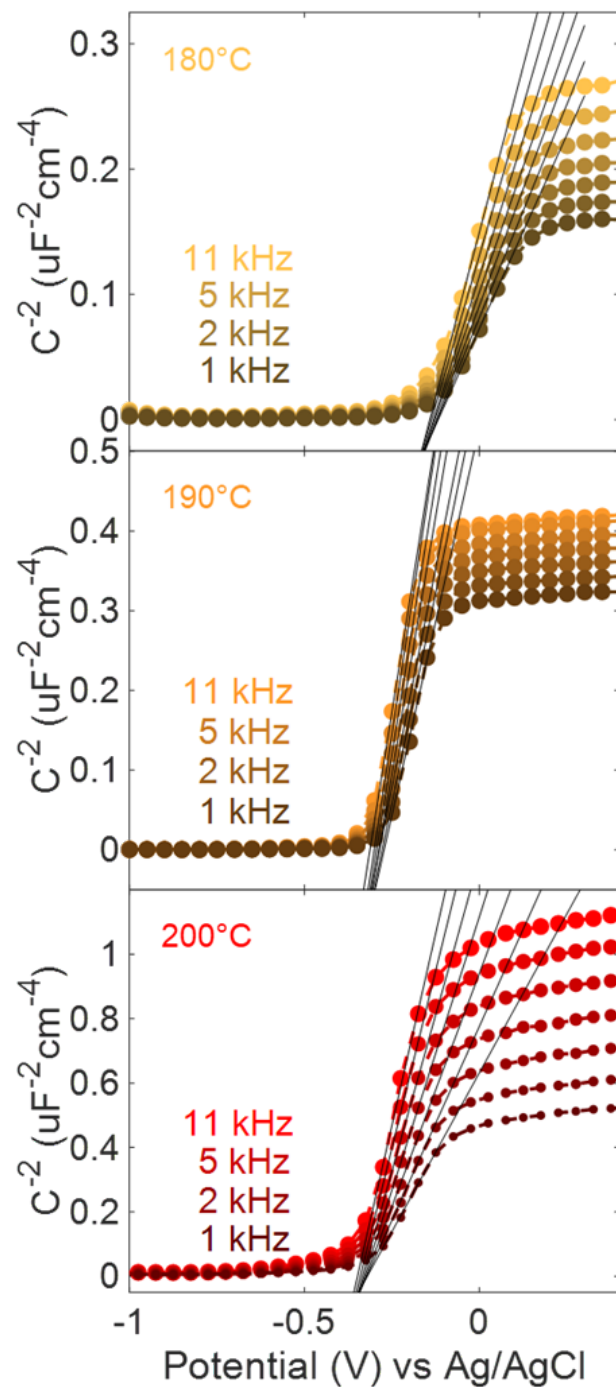
Figure 3.5. Capacitance-voltage (Mott-Schottky) plots from 1-11 kHz of SnO_x on FTO annealed at different temperatures. Extracted flat-band voltages are shown in Figure 3.2b-c and extracted charge carrier densities are shown in Figure 3.6.
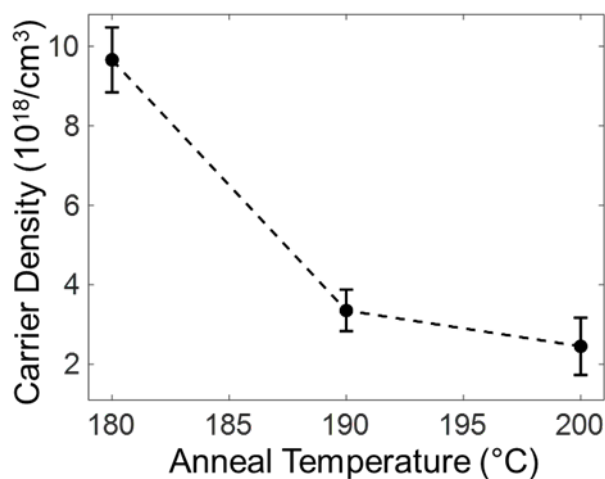
Figure 3.6. Charge carrier density of SnO_x on FTO films with different anneal temperatures extracted from 3.5.
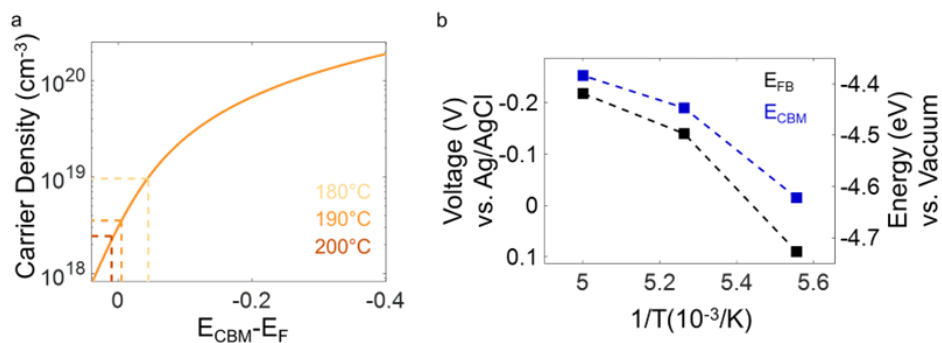
Figure 3.7. a) Charge carrier density as a function of the energy difference between the conduction band minimum (E_{CBM}) and the Fermi level (E_F). See a *Supplementary Note on Calculating Conduction Band Positions* written in the supplementary section. The dotted lines show how the carrier density (calculated from Mott-Schottky) is used to find the energy difference between the Fermi level and conduction band minimum. b) Comparison between the flat-band energy (E_{FB}) calculated from electrochemical-based Mott-Schottky and the conduction band calculated using Fermi-Dirac statistics.
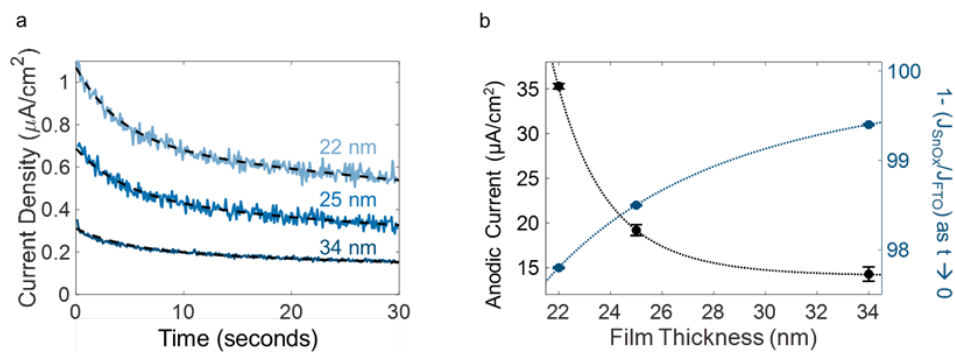
Figure 3.8. a) The current-time profiles of VTE-SnO$_x$ of varying thickness on FTO held at 0.4 V vs Ag/AgCl. If anodic currents are assumed to be the result of pinholes, the initial ratio of current between the tin oxide coated FTO and a bare FTO (extracted as time t goes to 0) can be modeled in a diffusion-limited regime to be proportional to the pore density of the films. Fitting for pinhole fraction results in the solid lines.[4] b) The calculated surface coverage compared to the anodic current at 1.5 V vs Ag/AgCl from cyclic voltammetry. This estimate of surface coverage is inversely correlated with the magnitude of anodic current measured in cyclic voltammetry. Lines are guides to the eye.
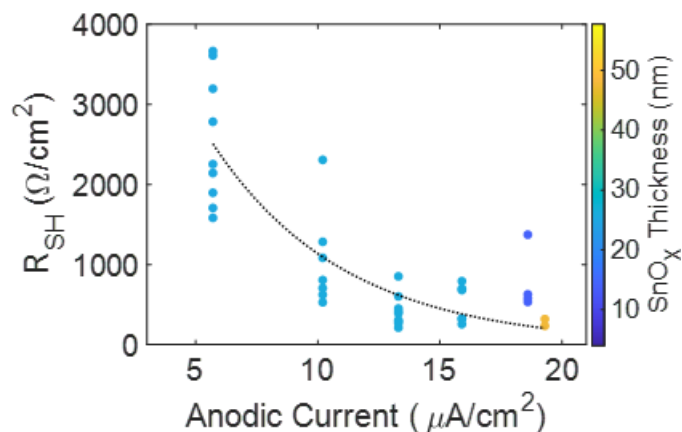
Figure 3.9. The shunt resistance of final devices plotted against the anodic current at 1.5V vs. Ag/AgCl of a representative film from the same deposition and annealing batch. The dotted line is the exponential decay fitting.

If leakage currents are assumed to be dominated by pinholes, the effective surface coverage of the ETL can be estimated by modeling the time-dependent change in current seen after a potential step based on diffusion-limited electron transfer at pinholes (Figure 3.8a).[4] In all cases there was a >97% reduction in the anodic current relative to when no ETL was present. Thick ETL films (at 34 nm) blocked 99.4% of the current (Figure 3.8b). Lower anodic currents thus appear unsurprisingly related to improved surface coverage, as has been shown previously in studies of titania for dye-sensitized solar cells,[80] and are indicative of lower shunt resistance in final devices (Figure 3.9).

3.3.2   Interfacial Reactivity

Finally, we adapted our electrochemical setup to probe for Sn^{II} defects by switching to a weakly acidic, aqueous methylammonium halide electrolyte (0.1 M). Under these conditions (pH 5.8), we expect Sn^{II} and Sn^{IV} to reduce to Sn0 near -0.9 V and -1.2 V versus Ag/AgCl, respectively.[124] Figure 3.19a shows photographs of as-deposited and 200°C annealed VTE-SnO$_x$ thin films after 5 minute potentiostatic biasing at the indicated potentials. Significant darkening of the as-deposited sample was observed at potentials -1.0 V, while darkening did not occur until < 1.2 V for VTE-SnO$_x$ annealed at 200°C. XPS analysis indicates this darkening correlates well with the conversion of VTE-SnO$_x$ to more reduced tin species, including Sn^0 (Figure 3.11). The corresponding chronoamperometry data are shown in Figure 3.12. We attribute reduction in the range of -1.0 to -1.2 V vs. Ag/AgCl to the reduction of Sn^{II} species like SnO to Sn^0 and at potentials from -1.2 to -1.3 V to reduction of Sn^{IV} in SnO$_2$, in accordance with previous studies at similar pH.[93, 125] The presence of tin species with intermediate coordination are suggested by the broadening of the Sn 3d$_{5/2}$ peak after electrochemical degradation (Figure 3.11). The effect of methylammonium acidity was verified by conducting control experiments under the same experimental conditions but using a 0.1 M potassium halide electrolyte. As expected, the thresholds for reduction in the VTE-SnO$_x$ films were shifted to more cathodic applied potentials, evidenced by the lack of darkening in the VTE-SnO$_x$ films (Figure 3.13).[125] The acidic
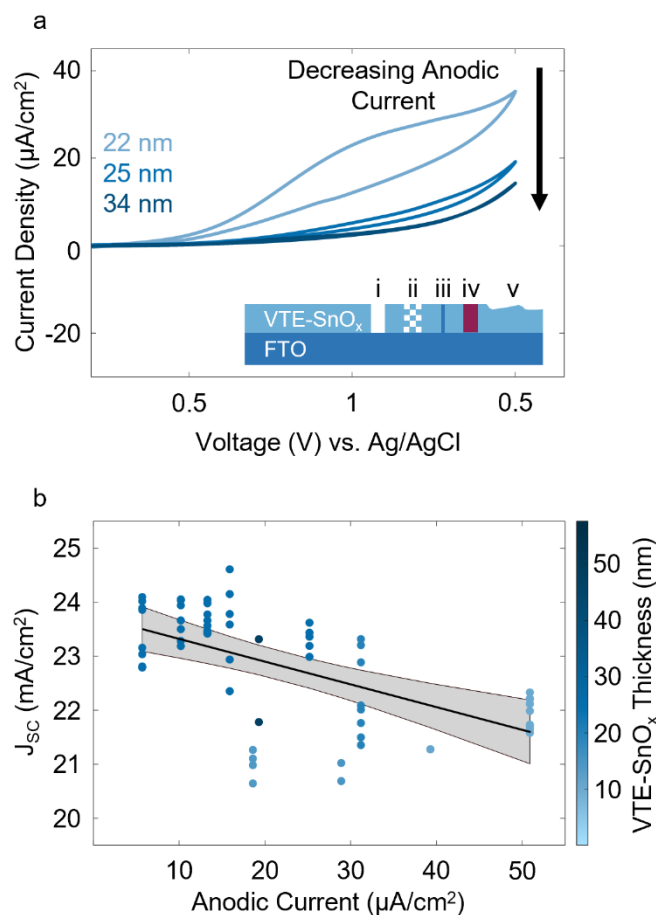
Figure 3.10. a) Cyclic voltammograms of VTE-SnO$_x$ films of the indicated thicknesses annealed at 195°C. Sources of current leakage include: i-ii) pinholes, iii) conductive filaments, iv) defects, and v) other inhomogeneities shown in the inset schematic. b) Short-circuit current density of final devices plotted against the anodic current at 1.5V vs. Ag/AgCl of a representative film from the same deposition and annealing batch. The shaded grey region is the 95% fit confidence interval. The devices are the same as those of Figure 3.2b

attack enabled by methylammonium agrees with recent studies on the perovskite/selective layer interface.[86, 87, 126, 127] Thus the combined XPS and electrochemical characterization strongly suggests the as-deposited VTE-SnO$_x$ contains significant concentrations of Sn^{II} relative to annealed VTE-SnO$_x$, providing chemical insight into the process and performance variations. Further, this highlights the ability of our electrochemical measurement in methylammonium to reveal the presence of high levels of reactive Sn^{II} by a rapid and simple test.
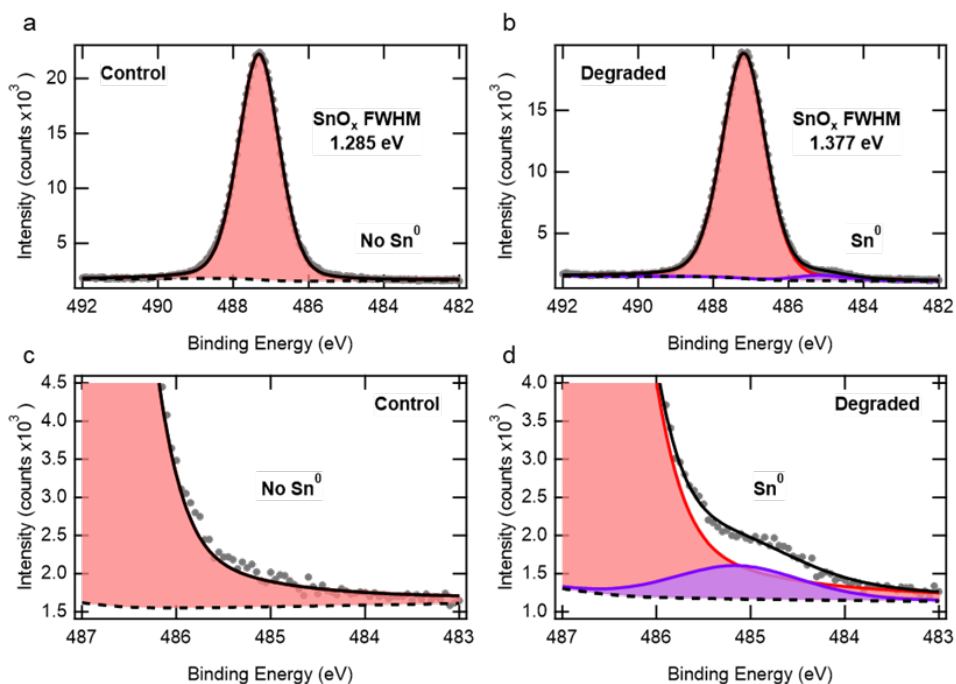
Figure 3.11. a) Raw tin 3d$_{5/2}$ (Sn 3d$_{5/2}$) XPS spectra of a pristine film (30 nm, 200°C anneal) and b) an electrochemically degraded film with contributions from the tin oxide (SnO$_x$) and metallic tin (Sn0) labeled. The FWHM for each SnO$-x$ feature is shown. Electrochemical degradation was induced by holding for 5 minutes at -1.3 Ag/AgCl in 0.1M aqueous MAI electrolyte. c) A closer look at the region of interest where no peak at 485 eV is observed in the control film but d) after electrochemical degradation there is formation of Sn0.

To augment the electrochemical identification of Sn^{II} defects, we performed XPS to directly measure the surface chemistry of the VTE-SnO$_x$ layers as a function of annealing temperature and confirm the origin of the electrochemical characteristics (e.g. the cathodic onset potential). Figures 3.19b and 3.19c show the Sn 3d$_{5/2}$-area-scaled Sn 3d$_{5/2}$ and VBM spectra of the as-deposited samples compared to samples annealed at the indicated temperatures (see
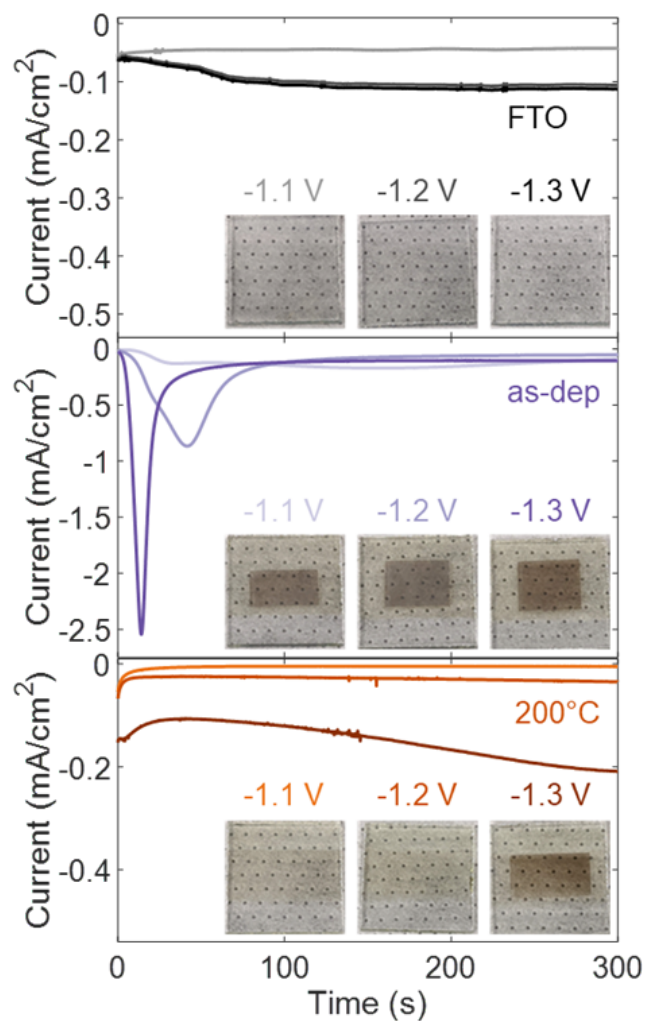
Figure 3.12. The chronoamperometry data corresponding to Figure 3.19a with optical images inset. The FTO control films exhibit no evidence of reaction though current readily passes through the film due to its conductive nature. The as-deposited films readily reduce to Sn^0 at every applied potential and the reaction is accelerated at more cathodic voltages. The annealed films exhibit no reaction until -1.3 V vs. Ag/AgCl is applied where a relatively slow reduction reaction is observed. All films are 25 nm and all voltages are with respect to Ag/AgCl.
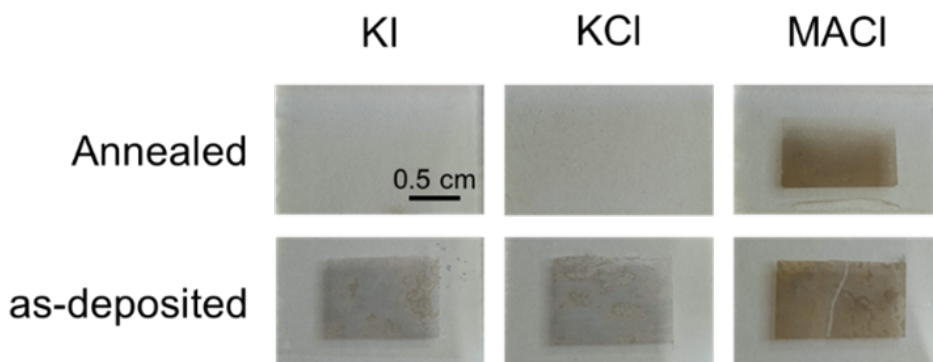
Figure 3.13. Optical images of SnOx films after being held for 5 mins at -1.3 V vs. Ag/AgCl in different 0.1 M aqueous electrolytes. As can be seen, while the as-deposited films react in the presence of all electrolytes, the annealed films (at 200°C) only react in the presence of MA, which as a weak acid dissociates in water. Both the fact that we a) see different reactions to the KI and KCl electrolytes, and b) see optically similar degrees of degradation for the as-deposited and annealed films in MACl but no Sn0 peak in the annealed films (with one in the as-deposited films) suggests different degradation mechanisms between the two processes likely occur.

Figure 3.14 for additional $3d_{5/2}$-area-scaled survey and core levels as well as Figure 3.15-3.16 for plots of the raw data). To determine the ratio of Sn:O we used three main techniques. First, we analyzed the Sn $3d_{5/2}$ core level to attempt to discern Sn^{II} from Sn^{IV}. However, the close proximity of the SnO and SnO_2 Sn $3d_{5/2}$ core level features resulted in a single peak for all samples that we could not confidently decompose,[124, 128–131] limiting us to correlate gradual shifts to higher binding energy (Figure 3.19d) with increased annealing temperatures as a likely indicator for higher ratios of SnO_2 to SnO.[132] Second, we analyzed the VBM, which qualitatively shows different valence "fingerprint" features for SnO and SnO_2 films.[130–132] Although quantitative interpretation is not possible, the increase in signal in the lower binding energy region of the VBM spectra again suggests that the as-deposited VTE-SnO_x has more Sn^{II} (SnO) character than the annealed films. Note that due to signal to noise issues with the original data, the spectra presented here are from an analogue set of SnO_x samples prepared under the same conditions (see Figure 3.17 for XPS VBM scans of the SnO_x films corresponding to the core level XPS). Finally, we calculated the O:Sn ratio shown in Figure 3.19d using the areas of the Sn $3d_{5/2}$ and O 1s peaks scaled by their relative sensitivity factors with contributions

from oxygen-bearing C, Ca, Na, and Si contaminants subtracted – assuming they come from the glass substrate due to dust from sample cleaving during preparation (see Figure 3.14-3.18 for calculation details). We note that this calculation requires a number of assumptions and therefore has multiple potential sources of error. Nonetheless, these results again suggest that the as-deposited film has a larger ratio of SnO to SnO_2 than the other films. Thus, while quantification uncertainties exist, the XPS results all qualitatively indicate a main difference in the VTE-SnO_x is the presence of Sn^{II} defects that are oxidized upon annealing in atmosphere to Sn^{IV}, at least at the surface, in good agreement with our electrochemical results (Figure 3.19a). The challenge of XPS quantification, particularly with elements and chemical states where decomposition is difficult (e.g. Sn $3d_{5/2}$), highlights the ability of electrochemical probes to provide actionable feedback with greater simplicity of measurement and analysis. In the end, both XPS and the chronoamperometry reactivity test reveal that the elimination of Sn^{II} defects play an important role in energetics, which can affect V_{OC}, and durability, providing mechanistic insights into the changes we observe in cyclic voltammetry when changing the anneal temperature.

The electrochemical probes used here – anodic and cathodic CV and potentiostatic stability tests in various electrolytes – and their empirical relationships to device performance enable an informed decision, within minutes, whether to proceed to the next process step or if the process conditions should be changed. Consequently, we now employ these quality control checks in our lab for VTE-SnO_x. Coupled with the ability of electrochemical techniques to probe large areas (Figure 3.20-3.21), these techniques may contribute to the scaling of MHP fabrication.
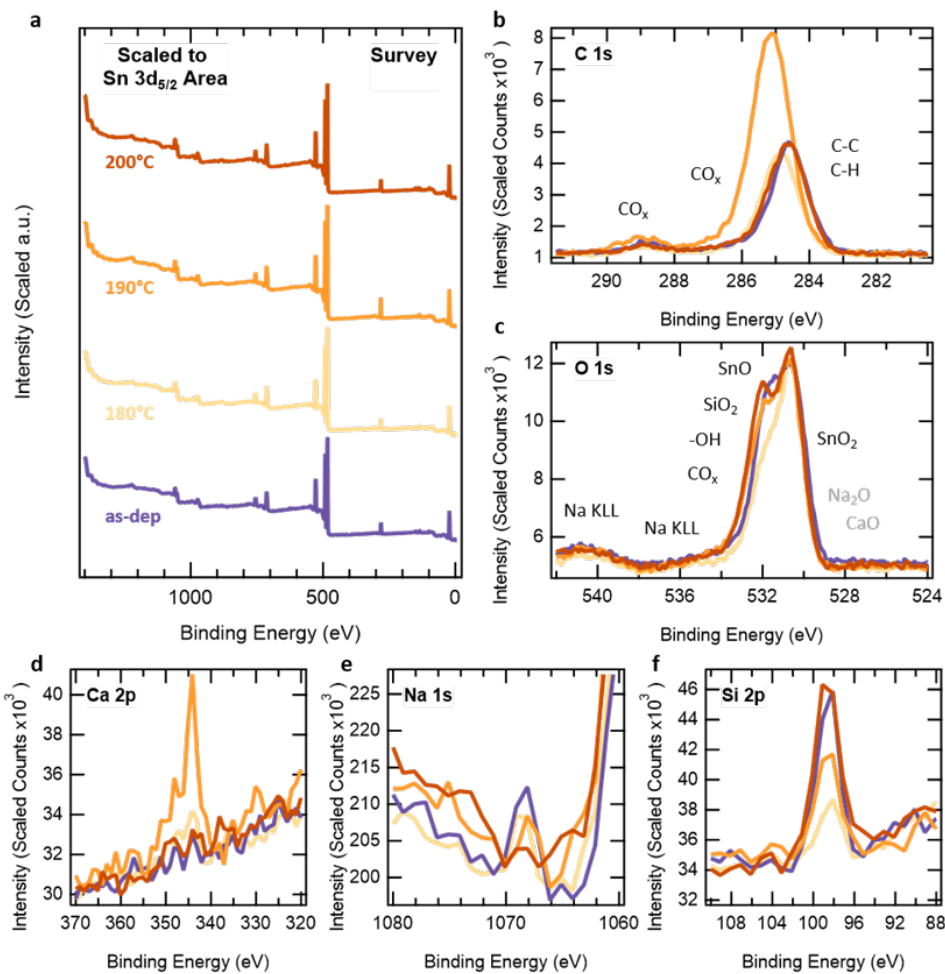
Figure 3.14. a) Survey spectra of SnO$_x$ films on FTO with variations in post-deposition anneal temperature. b) Carbon 1s (C 1s) spectra showing that the 190°C annealed film has a relatively high level of carbon contamination compared to the other films. c) Oxygen 1s (O 1s) spectra showing a general shift from high to low binding energies which is consistent with an increase in the SnO$_2$:SnO ratio. d) Calcium 2p (Ca 2p) spectra showing significant calcium contamination in the 190°C annealed film (confirming contamination concerns from C 1s spectra) e) Sodium 1s (Na 1s) spectra showing its variable presence in all films. f) Silicon 2p (Si 2p) spectra showing its variable presence in all films. Note that all scans shown here are scaled by the Sn 3d$_{5/2}$ area for comparison purposes and that raw data is shown in Figure 3.15-3.16.

47
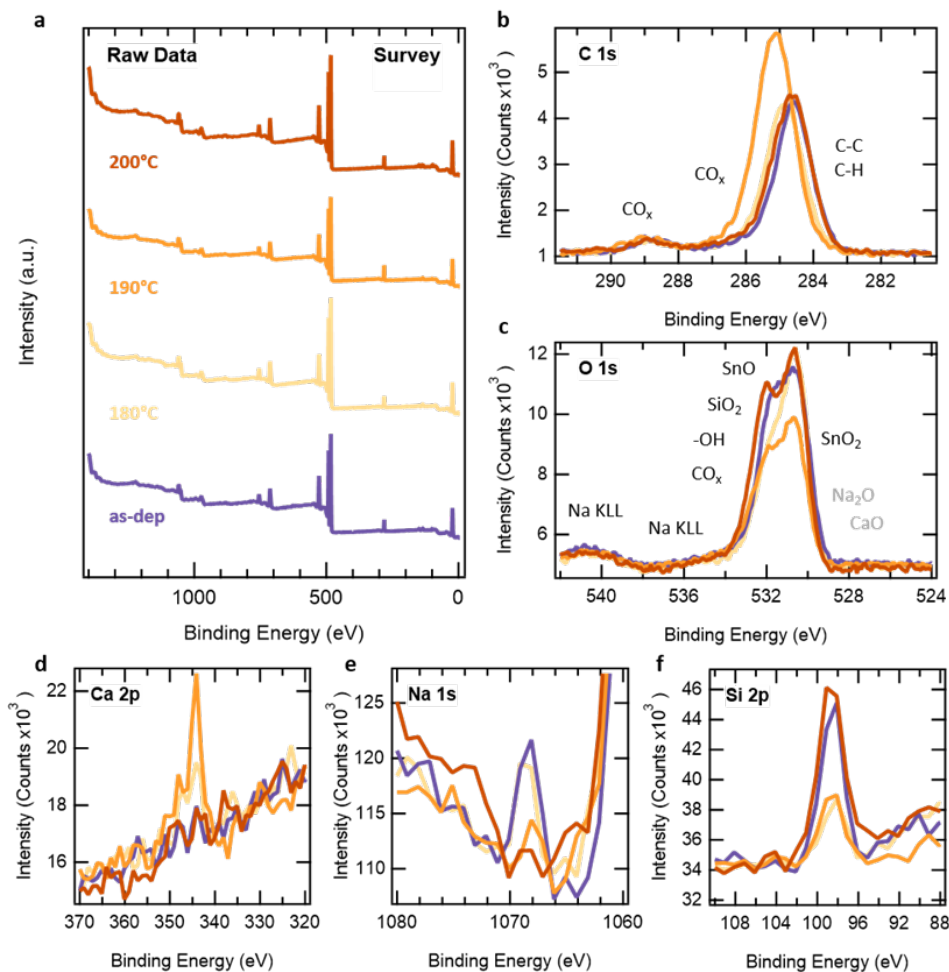
Figure 3.15. a) Survey spectra of SnO$_x$ films on FTO with variations in post-deposition anneal temperature. b) Carbon 1s (C 1s) spectra showing that the 190°C annealed film has a relatively high level of carbon contamination compared to the other films. c) Oxygen 1s (O 1s) spectra showing a general shift from high to low binding energies which is consistent with an increase in the SnO$_2$:SnO ratio. d) Calcium 2p (Ca 2p) spectra showing significant calcium contamination in the 190°C annealed film (confirming contamination concerns from C 1s spectra) e) Sodium 1s (Na 1s) spectra showing its variable presence in all films. f) Silicon 2p (Si 2p) spectra showing its variable presence in all films. Note that this is raw data with binding energy axis scaled by the average position of the C-C bond in C 1s across the sample set.

48
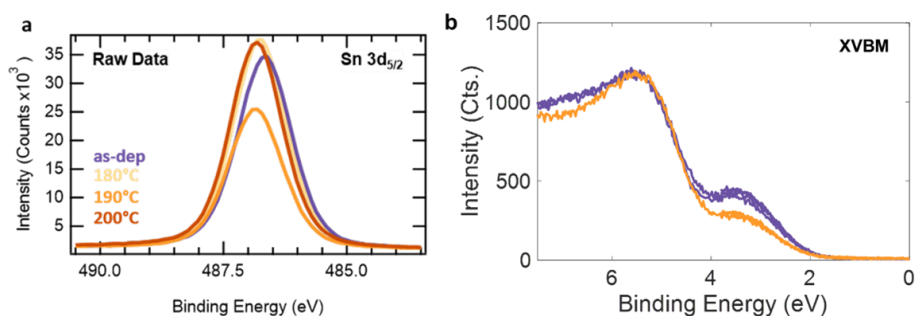
Figure 3.16. a) Tin $3d_{5/2}$ (Sn $3d_{5/2}$) spectra of SnO_x films on FTO with variations in post-deposition anneal temperature. b) X-Ray Valence Band Maximum (XVBM) spectra. Note that this is raw data with the binding energy axis scaled by the average position of the C-C bond in C 1s across the sample set.
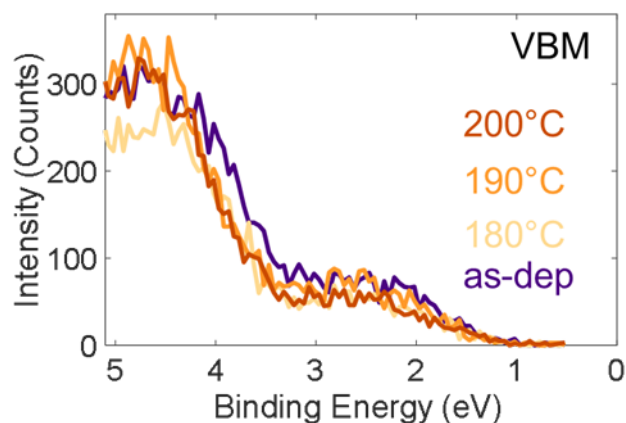
Figure 3.17. X-Ray Valence Band Maximum (XVBM) spectra of as-deposited and annealed SnO_x corresponding to the batches from Figure 3.19b-c, 3.12, and 3.14-3.16. Here, the integrations times were too low to observe a distinct difference between the 4 conditions and longer integration times were needed to improve the signal:noise (S/N) and confidence in differences between the SnO and SnO_2 fingerprint regions. A comparison between as-deposited and a film annealed at 190°C with good S/N is shown in Figure 3.19c.
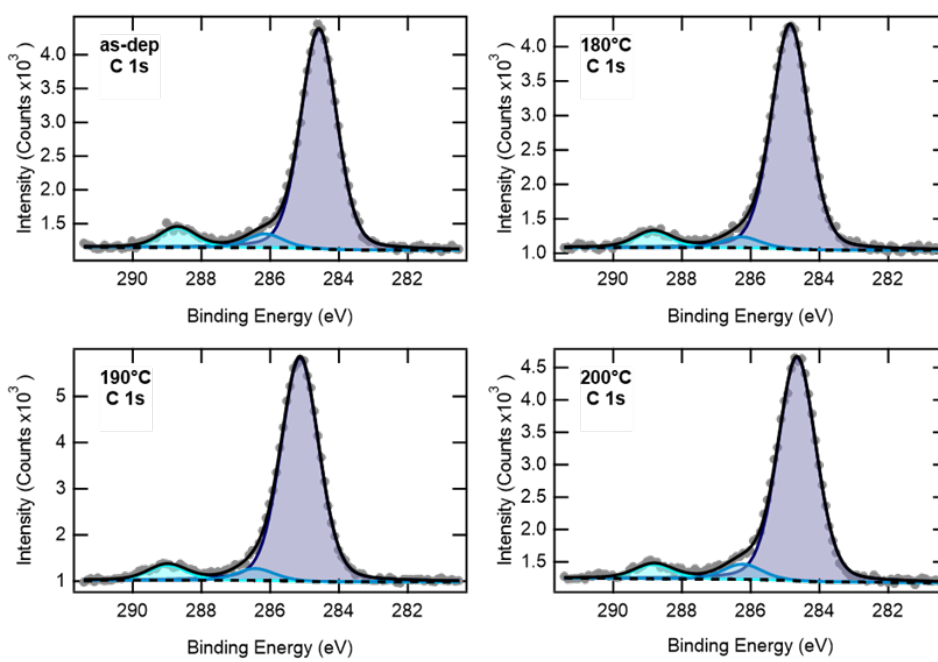
Figure 3.18. Deconvolution of the carbon 1s (C 1s) peak for the as-deposited and annealed SnO_x samples to determine the level of oxygen-containing carbon species, which were then subtracted from the oxygen 1s (O 1s) area to more accurately calculate the O:Sn ratio.[5]
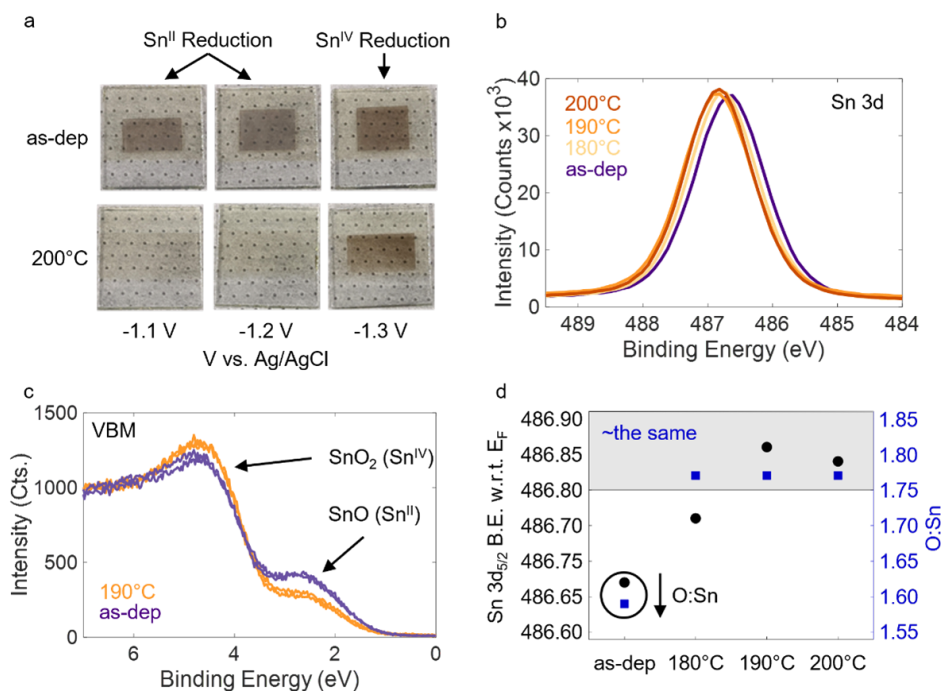
Figure 3.19. a) Photographs of as-dep and 200°C annealed VTE-SnO$_x$ biased at the indicated potentials (Ag/AgCl reference) in an aqueous 0.1 M methylammonium halide electrolyte visually indicating Sn^0 reduction originating from Sn^{II} (-1.1 to -1.2 V) and Sn^{IV} (-1.3 V), inferred from XPS (Figure 3.11). b) Sn Sn 3d$_{5/2}$ and c) X-ray valence band maximum scans (see Figure 3.17 for VBM scans corresponding to Figure 3.19b,d). d) Sn Sn 3d$_{5/2}$ core level shift and calculated O:Sn ratio as a function of annealing temperature.
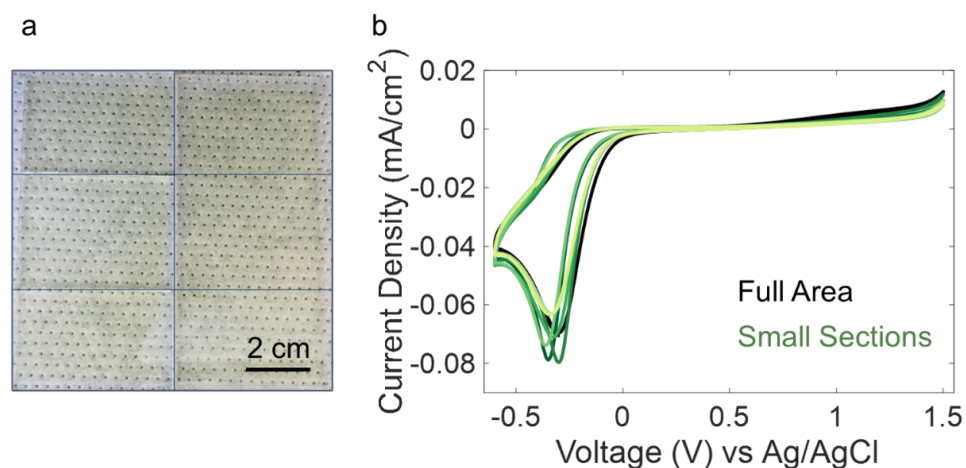
Figure 3.20. a) Optical image of a 40 nm 10x10 cm^2 SnO$_x$ film deposited on FTO and partitioned into six sections. b) Each section was tested individually via cyclic voltammetry showing homogeneity across the film.
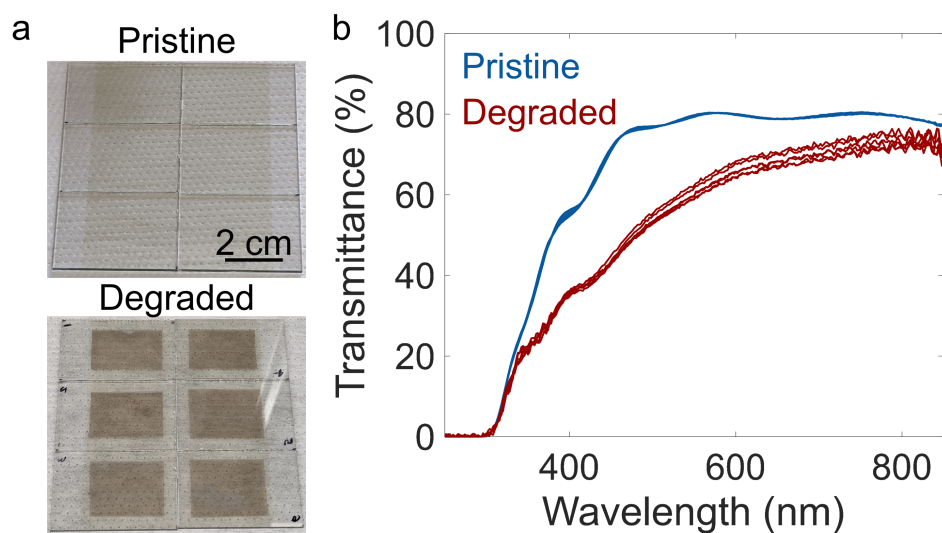
Figure 3.21. Optical image of a 10 x 10 cm^2 SnO$_x$ film deposited on FTO and partitioned into six sections a) before and b) after electrochemical stability testing in aqueous 0.1M MAI solution, where the substrate was held at -1.3V vs. Ag/AgCl for 5 minutes. c) UV-Vis spectroscopy from the six sections before (blue) and after (red) electrochemical degradation. The SnO$_x$ film was 25.2 nm and tested in its as-deposited state without post-deposition annealing.

3.4 Conclusions

In summary, using VTE-SnO$_x$ as a case study, we have revisited the application of simple electrochemical tools to assess the physical and optoelectronic properties of carrier selective contact layers that are relevant to high-performing solid-state optoelectronic devices. Moreover, we have directly correlated various electrochemical properties to final perovskite solar cell performance parameters. Given the critical performance requirements for carrier extraction, efficiency, and interfacial chemical stability in MHP solar cells, we have shown electrochemical tools are particularly well suited to provide rapid and actionable feedback on films incorporated into these devices. It should be noted that while demonstrated on VTE-SnO$_x$, these electrochemical probes are highly adaptable, including for polymeric and hole selective contact materials,[133] and are capable of addressing contact issues at scale. Therefore, they can be used both in the development of new transport layers, by aiding in the troubleshooting process, and/or as a screen for process reproducibility, by permitting comparisons between batches of substrates for perovskite device fabrication. Altogether, the simple electrochemical techniques discussed herein provide a platform for an improved learning cycle, enabling accelerated screening of novel contact layers for specific perovskite compositions to enable well optimized, stable, and high performing devices.

Chapter 3, in full, is a reprint of the material "Electrochemical Screening of Contact Layers for Metal Halide Perovskites" by Moses Kodur, Zachary Dorfman, Ross A. Kerner, Justin H. Skaggs, Taewoo Kim, Sean P. Dunfield, Axel Palmstrom, Joseph J. Berry, and David P. Fenning as it appears in ACS Energy Letters. The dissertation author was the first author of this paper, all authors contributed to this work.

Chapter 4

Solvent-free Transfer of Conjugated Polymers for Hole Transport Layers in Perovskite Solar Cells

4.1   Introduction

The ability to deposit thin films (< 100 nm) with precise thicknesses and in a sequential order is a critical aspect of semiconductor device manufacturing. As modern optoelectronic devices incorporate more organic components (e.g., OLEDs), the development of new processes which are compatible with a wide variety of hard and soft materials becomes increasingly important. Specifically in the context of devices, additional design considerations include an ability to yield homogeneous films on large substrates (> 100 cm^2) that are compatibility with the underlying layers that may be sensitive to stressors such as heat, solvents, or other conditions.

Conjugated polymeric materials—defined by the delocalization of electrons through an extended system of π bonds—are valuable in many multi-layer devices, such as organic and hybrid perovskite photovoltaic cells, due to their high charge carrier mobility, low temperature film formation, and band positioning. However, the deposition of polymeric materials is generally limited to processing from vapor, liquid, or solution phases (e.g., chemical vapor deposition, spin-coating, or various printing methods) which restricts the structural diversity that can be achieved. In the case of vapor-phase processing, the most significant drawback is that the

monomers must be polymerized in situ in a reactive process (as in chemical vapor deposition of polymers).[134–136] For solution-phase processing, perhaps the most significant limitation is ensuring the solvents used do not damage the underlying layers—i.e., "solvent orthogonality."

The deposition of pre-solidified films has been shown to open new opportunities by avoiding solvent incompatibility[137] and enabling conformal coating textured structures.[138] Free-standing polymer films have been of significant scientific and technological interest over the last two decades, where they are used in service of fundamental studies and characterization,[139–142] energy storage,[143] sensing,[144,145] separation membranes,[146] tissue engineering,[147,148] and various other applications.[149–152]

Here, we have made use of freestanding films to fully circumvent the concerns of solvent orthogonality by enabling deposition truly free of liquid solvents. While the polymers are originally formed atop a water bath, using the technique of interfacial spreading,[153–156] the freestanding films are fully dried prior to their transfer to a substrate meaning the underlying layers of a device are agnostic to the original solvents used to form the polymer (water and chlorobenzene in our case). In the intermediate stage of this technique, named "solvent- free transfer" (SFT), the freestanding films are supported by custom built frames which support the edge of the films by van der Waals forces. These films can then be transferred directly onto a variety of substrates that are either bare or coated with other layers in a device stack in a manner which is compatible with roll-to-roll manufacturing. We demonstrate that SFT has significant potential in depositing over large areas by forming and transferring free-standing films which are up to 10×10 cm^2 in area, with thicknesses of approximately 20 nm.

These films are characterized and compared to spin-coated controls to discern uniformity and quantify optoelectronic properties by using surface profilometry, atomic force microscopy, scanning electron microscopy, and electrochemical chronoamperometry and cyclic voltammetry. Finally, we demonstrate the viability of the films as hole-transport layers (HTL) in small area (0.07 cm^2) perovskite solar cells (PSCs) proving their optoelectronic quality.

4.2   Materials and Methods

4.2.1   General

All polymer solutions were made with chlorobenzene as the primary solvent, magnetically stirred for at least 12 hours at approximately 60 °C, and were taken off the heat shortly before experiments and allowed to cool to room temperature. All air plasma treatments were done using a RF plasma cleaner from Harrick Plasma. The plasma cleans were done at 30 W with a chamber pressure of approximately 300 mTorr. All depositions on glass were done within 1 hour after plasma treatment.

4.2.2   Preparation of the Freestanding Polymer Films

All film formations and drawing were performed on custom-built systems. All custom parts, such as roller drums, troughs, and substrate carriage were printed on a Form 3 SLA printer using Form Clear Resin. The troughs in particular were treated in air plasma for an extended period of time (>3 hr) to crosslink the print surface and minimize leeching of the monomers and oligomers into the water used for interfacial spreading. Furthermore, a hydrophobic silane treatment was applied to the trough surface to modify the water contact angle and planarize the water surface in order to avoid pooling of the polymer solution.

4.2.3   Polymer Film Characterization

Profilometry

The initial thickness of transferred films was estimated by using the same "spreading parameters" (drop volume, polymer solution concentration, and dish size) to form films which were transferred to planar (glass) substrates. For P3HpT and P3BT films, the concentrations used were 10 mg/mL and 7 mg/mL respectively. For the small-area trough (4 × 11 cm area) a droplet volume of 15 μL was used. For the large-area trough (13.5 × 15.5 cm area) a droplet volume of 70 μL was used. The thickness of these films was then measured using a Dektak XT

profilometer.

Electrochemistry

For all electrochemical measurements, we used a standard three-electrode system with a bare/coated ITO as the working electrode, a platinum (Pt) wire was used as the counter electrode, and a non-aqueous single junction silver (Ag) reference electrode (Pine Research, AKREF0033) filled with 10 mM of silver nitrate in acetonitrile. In chronoamperometry, the electrolyte used was 0.1M tetrabutylammonium hexafluorophosphate (TBAH, supplied by Fluka) in anhydrous propylene carbonate (Sigma Aldrich) where 20 g/mL of ferroene was added to serve as the redox couple. All voltages reported were corrected with 85% automatic and 15% manual iR compensation and all electrochemical measurements were performed on a Biologic VSP 300 potentiostatic with EC-lab software. The reference electrode was calibrated using the ferrocene/ferrocenium redox couple whose redox standard potential in propylene carbonate has been determined to be 0.624 V vs SHE.[157] In the chronoamperometric measurements to determine pore density, the films were held at 0.8 V vs. SHE for 30 seconds after a 2 second linear sweep from open-circuit voltage. In order to minimize the formation of pinholes, all samples were prepared in a Class 100 cleanroom using a sequentially filtered P3BT solution (0.45 μm and 0.2 μm pore sizes).

Atomic Force Microscopy

The polymer films were deposited by SFT or spin-coated onto polished silicon which had been rinsed in acetone, ethanol, isopropyl alcohol, and deinonized water, followed by treatment with air plasma. AFM measurements were taken using a Veeco atomic force microscope (AFM) in tapping mode and analyzed using Nanoscope and Gywddion software.

Scanning Electron Microscopy

SEM micrographs were captured on a Zeiss Sigma 500 SEM with an accelerating voltage of 3.00 kV and an InLens detector. The samples used were the same as AFM.

4.2.4 Preparation of Perovskite Solar Cells

Substrate Preparation

Indium tin oxide (ITO) substrates were purchased pre-diced and pre-etched from Biotain Crystal Co. (TEC 8, 6-8 Ω/sq). They were cleaned by a series of sonication and washing steps as follows: sonicate in 2 vol% Hellmanex III in DI water for 15 min, rinse with DI water, sonicate in DI water for 15 min, rinse with DI water, sonicate in IPA (99.5% purity) for 15 min, rinse with IPA, sonicate in acetone (99.9% purity) for 15 min, rinse with IPA, and then dry with filtered dry air. Immediately prior to tin oxide deposition, the FTO substrates were UVO-treated for 20 min.

Tin Oxide Electron Transport Layer

The seed solution was prepared by diluting a colloidal dispersion of SnO_2 (15% in water, Alfa Aesar) with DI water (Alfa Aesar) in a 1:4 volume ratio. Prior to use, the solution was stirred at room temperature for 4 hours then filtered with a 0.22 μm PTFE filter. Cleaned and UVO-treated substrates were prepared and 150 μL of the SnO_2 seed solution was spun atop the substrates at 4000 RPM for 30 seconds in air. The films were then sintered at 150°C for 30 minutes also in air.

Perovskite Absorber

The selected perovskite composition has a nominal solution stoichiometry of $FA_{0.78}MA_{0.05}Cs_{0.17}Pb(I_{0.85}Br_{0.10}Cl_{0.05})_3$ dissolved in a 3:1 v/v mixture of DMF and DMSO at a 1.25 M concentration. Prior to the perovskite deposition, the tin oxide coated ITO substrates were treated again with UVO to improve the wettability of the perovskite solution resulting in better films. The films were spin-cast at 5000 RPM for 50 s with a 200 μL drop of methylacetate 22 s into the spin. The resulting films were annealed at 100 °C for 30 min. All perovskite processing was conducted in a nitrogen-filled glovebox.

FAI was purchased from GreatCell Solar Materials, CsI (99.999% purity) and MACl (99.0% purity) from Sigma Aldrich, lead iodide (99.99% purity) and lead bromide (99.99%

purity) from TCI, and lead chloride (99.999% purity) from Sigma-Aldrich.

P3AT Hole Transport Layer

Both poly(3-heptylthiophene) and poly(3-butylthiophene) were dissolved in chlorobenzene at a concentration of 10 and 7 mg/mL, respectively. In the case of the solvent-free transfer, a droplet of solution, with a volume of 15 μL, was dropped onto water in a narrow trough and allowed to solidify on top of the water. The film formation and drawing was done in an oxygen-free, nitrogen-filled glovebox with an oxygen content below 0.02%. The films were then transferred into a separate nitrogen-filled glovebox ($<$ 1 ppm water or oxygen), with a drying step in the antechamber under dynamic vaccum for 10 min. The films were then transferred onto the perovskite device stack and conformal coating was promoted by a vapor treatment of chloroform, performed in a recrystallization dish with a glass lid, at room temperature, for 5 min.

Gold Top Contact

A 100 nm layer of gold was deposited by vacuum thermal evaporation with a 5 nm adhesion layer deposited at 0.03 Å/s then finshed at 0.5 Å/s.

4.2.5   JV Testing

After device fabrication was completed, the cells were allowed to age in nitrogen for 15 days, as this was observed to significantly improve the device fill factors by eliminating "double-diode" behaviour in the JV sweeps (Figure S10). Devices were tested in nitrogen environment using an ABET Mondel 11002 SunLite Solar Simulator, under AM 1.5G, at 100 mW/cm^2, with a scan speed of 0.1 V/s, and a fixed aperture of 0.07 cm^2. Prior to testing, the light intensity was calibrated using a standard silicon reference cell purchased from PV Measurements, Inc.
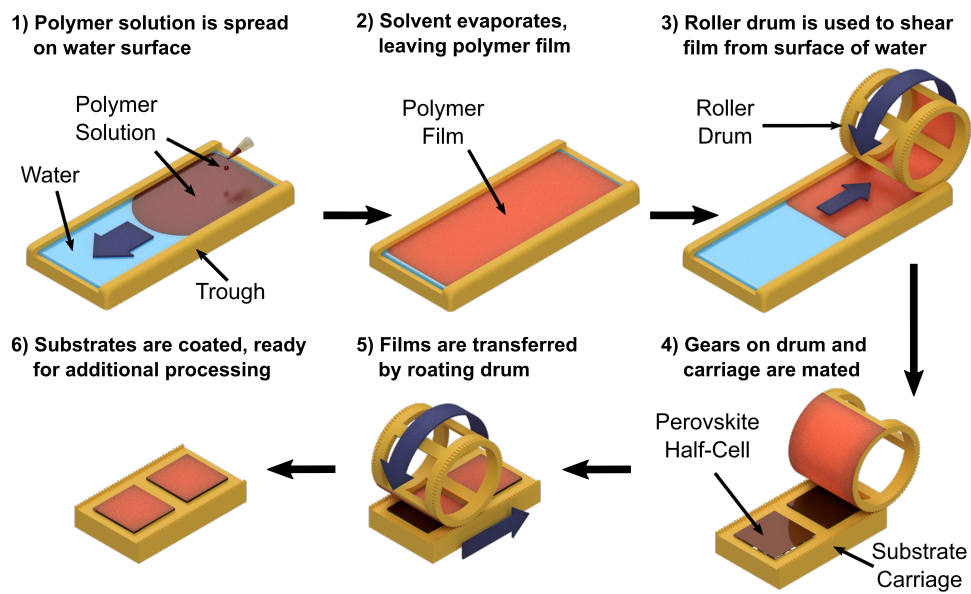
Figure 4.1. Summary of the solvent-free transfer process. A polymer film is formed on the surface of water before being sheared from the water surface using a cylindrical drum. The freestanding film can then be subsequently transferred to a solid substrate.

4.3   Results and Discussion

A summary of SFT, as it is applied in the fabrication of PSCs, is shown in Figure 4.1. The process begins by the interfacial spreading of a polymer solution on the surface of water held in a rectangular trough (step 1). The spreading of the polymer solution itself is driven by the Marangoni effect.[137] Once the solvent evaporates, it leaves behind a polymer film suspended upon the surface of the water. The thickness of this film is determined by the concentration of the solution, the volume of the droplet, and the surface area of the trough (step 2). This film is then contacted at the edges by a supporting structure, in this case a cylindrical drum, to which the edges of the polymer film adhere. The drum is rotated to shear the polymer film off of the surface of the water (step 3). An image of the apparatus used to to draw the film from the water bath is shown in Figure 4.2.The drum with suspended films can then be aligned (step 4) and rolled over appropriately shaped substrates to transfer the film, e.g., to a perovskite half-cell (step 5). An image of the apparatus used to to draw the film from the water bath is shown in Figure 4.3. Once the films have been transferred, the device stack is ready for additional processing (step 6).

Depending on the interfacial energies between the polymer and the desired substrate, the film will readily wet the substrate or it may benefit from additional treatment to promote complete contact. In the case of the perovskite/polymer pairings used in this work, we used chloroform vapor to promote the wetting process, but if the substrate surface is sufficiently hydrophilic, the wetting is rapid and effective.
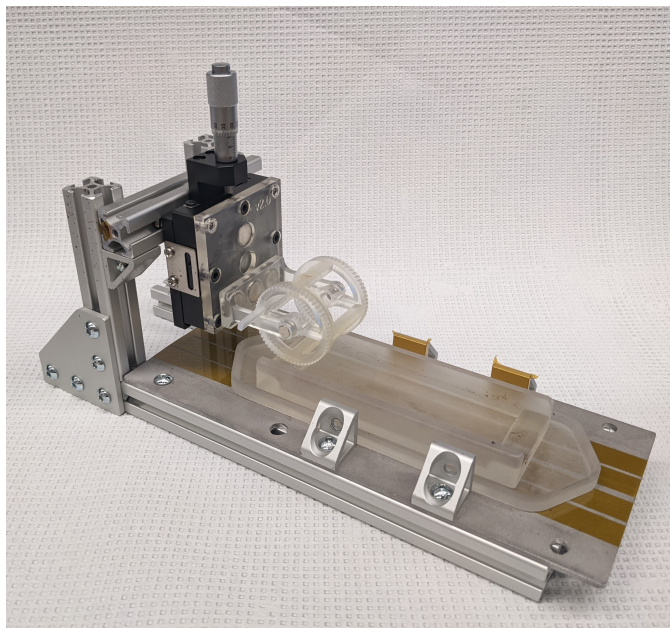
Figure 4.2. The setup used to draw the small area (25×25 mm) freestanding films.

Because of the reliance of SFT on interfacial spreading, it is important to acknowledge the unresolved challenges we encountered when determining which polymers would successfully spread and in achieving reproducibility. For example, we found that the P3AT (poly(3-alkylthiophenes)) family of polymers typically exhibited excellent interfacial spreading and routinely formed high quality films. However, P3HT (poly(3-hexylthiophene)) had significant variability from batch to batch and often resulted in torn films with significant thickness variation across lateral length scales of the order of centimeters. Similarly, Poly-TPD ((N,N'-bis-4-butylphenyl-N,N'-bisphenyl)benzidine) sometimes formed high quality films and sometimes produced films with substantial wrinkling. PTAA (poly(triaryl amine)) was expected to perform similarly to Poly-TPD given their structural similarities but we were never able to
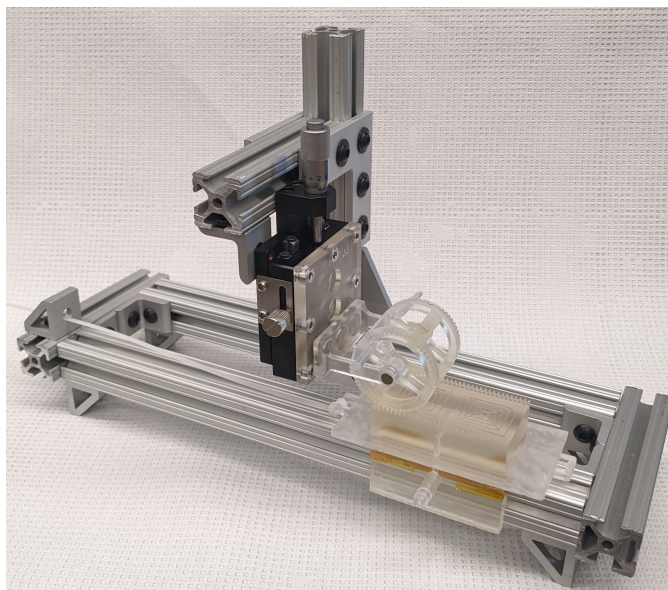
Figure 4.3. The setup used to transfer the small area (25 × 25 mm) freestanding films onto correspondingly sized substrates. Note the presence of a vacuum line on the carriage to hold the substrates in place as the transfer is performed.

successfully spread and transfer a single film. These inconsistencies were observed despite attempts to control the environment (polymer solution preparation in a nitrogen-free environment, UV-light filtering when handling polymer solution or films, solution spreading performed in cleanroom or oxygen-free glovebox, etc...) suggesting that the specific properties which allow a given polymer and batch to spread effectively remains an open question. Overall, we found SFT was amenable to several polymers. In particular, we were readily able to form and coat films from the family of P3ATs as well as Poly-TPD. However, other polymers, such as poly[2,5-(2-octyldodecyl)-3,6-diketopyrrolopyrrole-alt-5,5-(2,5-di(thien-2-yl)thieno [3,2-b]thiophene)] (DPP-DTT), fractured while removing the film from the surface of the water. Nevertheless, it may be possible to broaden the scope of the process to include more brittle polymers with the use of additives or plasticizers. The polymers with which we attempted to form freestanding films are shown in Figure 4.4.

When forming large area films (100 cm^2), we replaced the rotating drum with a square planar frame (10 × 10 cm^2) which shears the film from the water surface by translating laterally
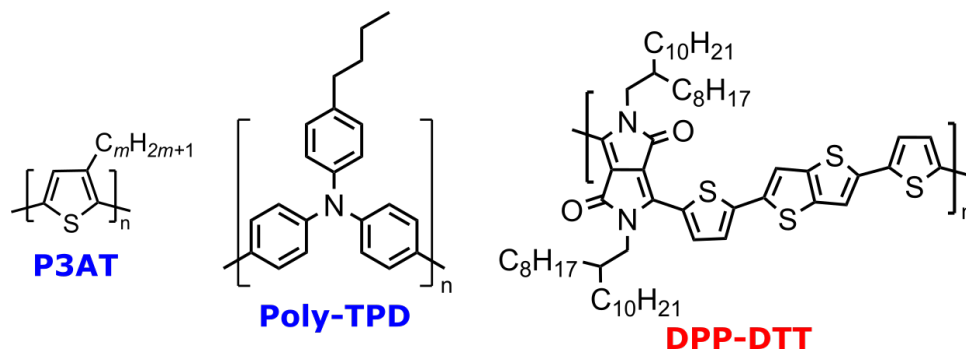
Figure 4.4. Chemical structures of the polymers with which we attempted to form freestanding films. We were successful in forming contiguous freestanding films with the P3ATs ($m = 4, 6, 7$) and Poly-TPD, whereas DPP-DTT fractured during the rolling of the drum.
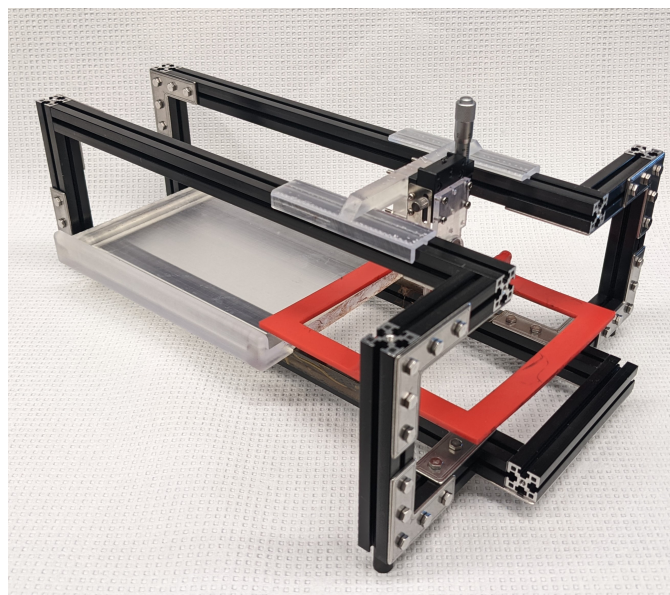
Figure 4.5. The setup used to draw and transfer the large area (10×10 cm) films onto correspondingly sized substrates. The setup is shown in the drawing configuration. The transfer configuration requires the trough be swapped out for a substrate holder, but is otherwise the same.

on a linear bearing (Figure 4.5). This approach is conceptually equivalent to a roller drum of infinite radius. The use of the planar frame (instead of a large drum) minimizes the strain on the film, and the drawn films were of high quality (Figure 4.6a). The film can then be transferred to a large area substrate by lowering down the film at a gentle, off-horizontal angle such that one corner touches down first. Upon contact with a high energy surface, such as glass treated with air plasma, the film is quickly pulled down onto the surface as the triple interface (glass/polymer/air) propagates across the substrate. As this process evolves, air pockets sometimes form. We observed in most instances that these pockets deflated by themselves as the gas molecules diffused through the film, as was the case for the transferred film shown in Figure 4.6b. Otherwise, the elimination of the bubbles can be accelerated by exposing the substrate and film to solvent vapor.
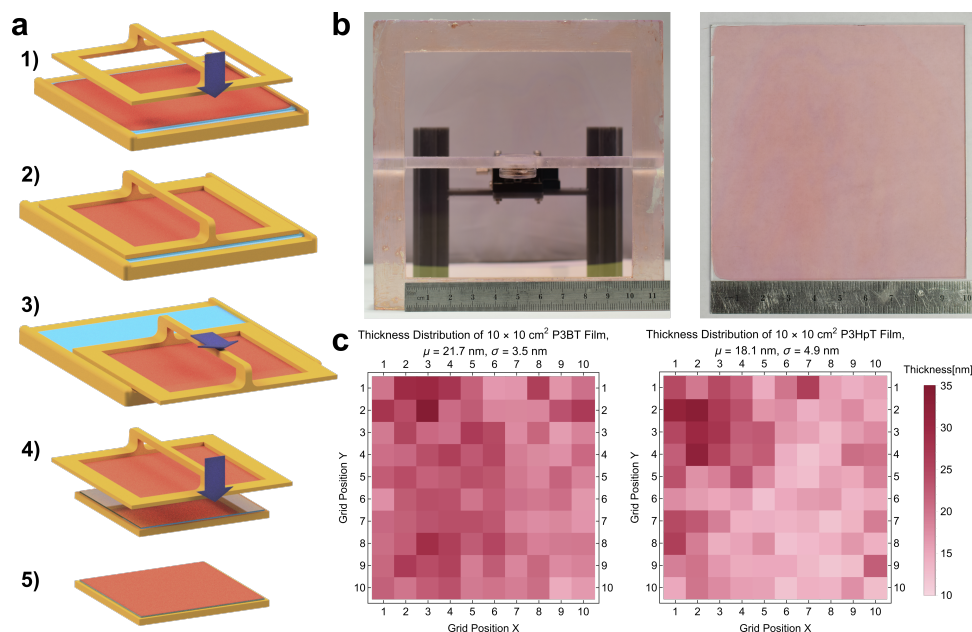
Figure 4.6. a) Summary of the large-area SFT variant, where the floating film is sheared off the water surface by a planar frame, which translates horizontally. This film can then be applied directly to a substrate. b) Photographs of a 10×10 cm^2 area film made of P3BT, mounted on the drawing frame (left) as well as after the same film was transferred onto a sheet of glass (right). c) Thickness measurements by profilometry of the same P3BT film (left) as well as a separate P3HpT film (right).

The thickness uniformity of these films was assessed by contact profilometry (see Figure

4.6c), which we found to have a reasonably low standard deviation (< 5 nm) for films with an approximate mean thickness of 20 nm. Additionally, the quality of the film formed also strongly depends on the local environment, control over which was limited in the ambient laboratory environment. Factors such as the presence (or absence) of air currents can influence the uniformity of the film. Generally, the last regions to dry are also the thickest. This non-uniformity can be attributed to increasing concentration of polymer in the liquid region as the film solidifies in an adjacent region. Therefore, the manner in which the film dries can have a significant impact on the uniformity of the film. For example, in the case of large area films (which were formed with the setup simply placed in the open air of a fume hood), the last region to dry was consistently one of the back two corners, and when drawn, this region would be slightly, but visibly, thicker than the others. In contrast, when the evaporation was allowed to proceed in an enclosed container without flowing air, the overall solidification of the film was much less predictable, as was the subsequent non-uniformity. It may be possible to create a channel where uniform laminar flow can be leveraged to produce films with greater uniformity than is shown in Figure 4.6c.

We then measured the roughness and pinhole density of the films produced by SFT compared to those produced by spin-coating (SC). Films produced by both methods were of the same thickness (ca. 20 nm) and derived from the same solution. Atomic force microscopy (AFM) was used to generate a topographic map of the film surfaces before and after exposure to chloroform vapor, i.e. solvent-vapor annealing (Figure 4.7a). A quantitative look at the surface roughness of the films shows that, overall, the SFT films were slightly smoother than their SC equivalents (Figure 4.7b). As expected, the chloroform vapor treatment reduced the roughness for both the SFT and SC films. To ensure that the minima shown in the AFM images were not pinholes, we obtained scanning electron microscopy (SEM) images of the films (Figure 4.7c); no pinholes were observed.

In addition to AFM and SEM, we tested for the presence of pinholes using electrochemical chronoamperometry.[158] In this technique, we utilized a standard three-electrode system with 0.1
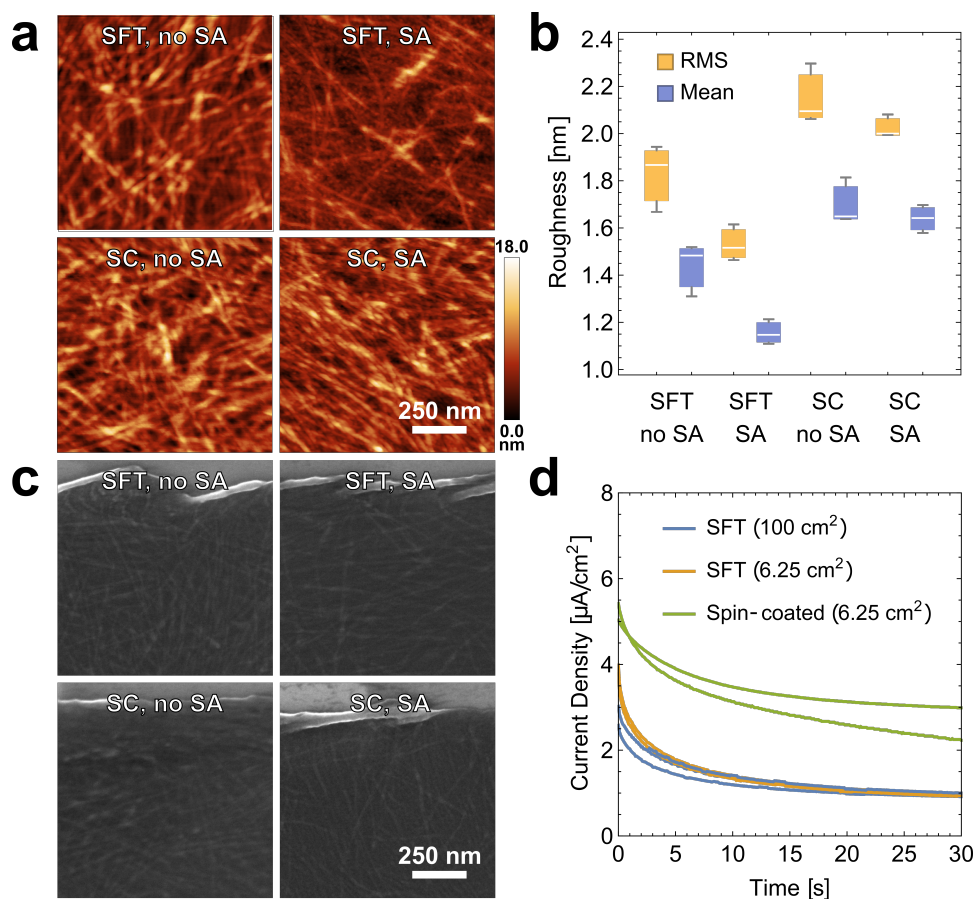
Figure 4.7. a) Atomic force microscopy of P3BT films that were deposited by SFT (top row) and spin-coated (bottom row). Films were evaluated before solvent-vapor annealing (SA) (left) and after SA (right). b) Root-mean-squared and mean roughness of the various films, before and after SA. c) Scanning electron micrographs of the same films. An InLens detector was used to enhance contrast from surface roughness. The horizontal feature at the top of each micrograph is an intentionally scratched region to demonstrate the contrast between the polymer and its underlying silicon substrate. d) Electrochemical chronoamperometry of P3BT films that were deposited by large-area SFT (blue), small-area SFT (yellow), and spin-coating (green) To compare the scalability of SFT, multiple small area films are compared to multiple regions of a single large area film.

66

M tetrabutylammonium hexafluorophosphate (TBAH) in anhydrous propylene carbonate (PC) as the electrolyte and ferrocenne/ferrocenium (F_c/F_c^+) as the outer sphere redox couple. The films were held at 0.8 V vs. SHE for 30 seconds resulting in an exponential decay curve (Figure 4.7d). As detailed in our previous work,[159] the ratio of the current density as time approaches zero between the P3BT-coated ITO electrode and the bare ITO electrode (Figure 4.8) approximates the pore density by with charge can be transported whether by defects, pinholes, conductive filaments, and impurities. Using this method, the surface coverage for films transferred by both SFT methods (small and large area) as well as SC controls was estimated. The results are tabulated in Figure 4.9. We find that all of the films performed similarly with the large area SFT, small area SFT, and SC films exhibiting 97%, 96%, and 95% coverage, respectively. The large area SFT films all came from a single film that was simultaneously applied to several small area (25×25 mm^2) substrates. All of these films were produced from the same sequentially filtered solution (0.45 μm and 0.2 μm pore sizes) and made in a Class 100 cleanroom in order to minimize the occurrence of pinholes.
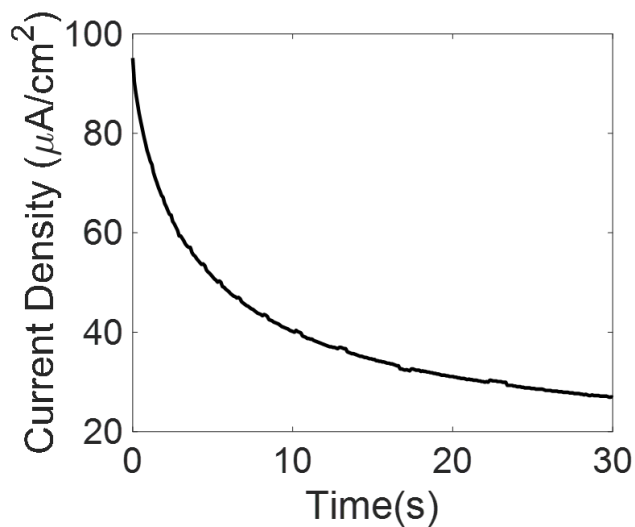
Figure 4.8. Chronoamperometry of the bare ITO substrate.

Ultimately, we were interested in how films deposited by SFT perform in devices in comparison to films produced by spin-coating. In a typical perovskite solar cell (PSC), the

Sample	Coverage
LA-A	0.968
LA-B	0.973
LA-C	0.966
LA-D	0.973
LA Average	**0.970**
SA-1	0.958
SA-1	0.961
SA Average	**0.960**
SC-1	0.943
SC2	0.947
SA Average	**0.945**

Figure 4.9. The surface coverage of each film as determined by chronoamperometry.

absorber is sandwiched between two charge selective layers (the electron- and hole-transporting layers, ETL and HTL). In general, the selective layers must exhibit high electronic conductivity for the desired charge carrier, have favorable band alignments with the absorber, be chemically compatible with the absorber, have a high degree of stability against operational stressors, be optically transparent, and form interfaces with low levels of carrier traps. We reasoned that PSCs would be a good platform on which to test the viability of SFT of a conjugated polymer due to the lack of liquid solvents needed for SFT, which might otherwise damage the underlying perovskite absorber.[160, 161] Additionally, the stability of PSCs is often further negatively impacted by the additives incorporated into the other layers in the device stack, such as the dopants used in the hole-transport layers (HTLs) made from small-molecular (non-polymeric) organic semiconductors.

We made PSCs with a variety of P3ATs, and found the electronic performance of all P3ATs tested to be comparable (Figure 4.10, with a slight loss in V_{oc} with increasing side-chain length. Ultimately, we settled on poly(3-heptylthiophene) (P3HpT) due to the favorable adhesion
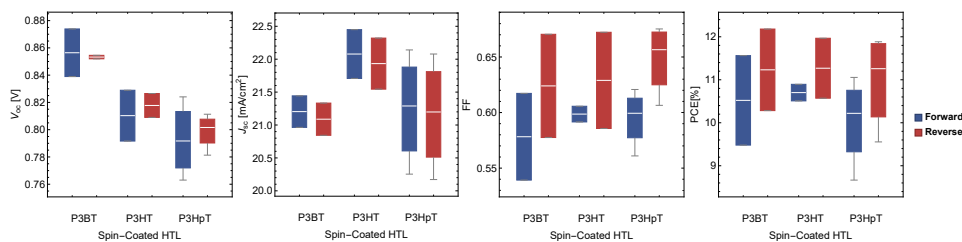
Figure 4.10. Photovoltaic metrics of perovskite cells using one of several spin-coated P3ATs as the HTL. While there is a trend towards higher V_{OC} for shorter alkyl side-chains, the generally comparable performance of the P3ATs, along with the improved wetting of P3HpT on the perovskite, led us to choose P3HpT as our HTL for subsequent batches.

that we observed with the perovskite and this polymer, as opposed to that of glassier P3ATs with shorter alkyl chains. These films had free-standing dimensions of 2.5×2.5 cm^2, though the device active area was significantly smaller, at 0.07 cm^2, as defined by a stencil mask. Our findings are summarized in Figure 4.11. In general, we found the performance of the SFT films to be comparable to the SC ones. The open-circuit voltage, V_{oc}, of SFT devices were somewhat lower, and showed greater hysteresis, when compared to those made with SC. However, the SFT devices displayed slightly increased short-circuit current density, J_{sc}, in both scan directions. The fill-factor (FF) was comparable between the two types of devices, with SC slightly outperforming SFT in the forward scan, but the opposite in the reverse scan. The underlying cause for these differences is unclear, but one possible explanation could be the difference in microstructure of the polymer which results from different processing conditions.[162] For example, the preferential edge-on microstructure of films formed by interfacial spreading when compared to films formed by SC could slightly alter the energetics at the HTL/perovskite interface, therefore affecting the photovoltaic metrics.

Additionally, we attempted to analyze the impact of different SFT processing steps on the final device performance. This included manipulations to the environment during formation to control the oxidative state, the use of chloroform vapor treatment to promote conformal coverage, and aging the completed devices in an inert environment. As expected, we found that the atmosphere used during film formation impacted the overall device performance (Figure 4.12.
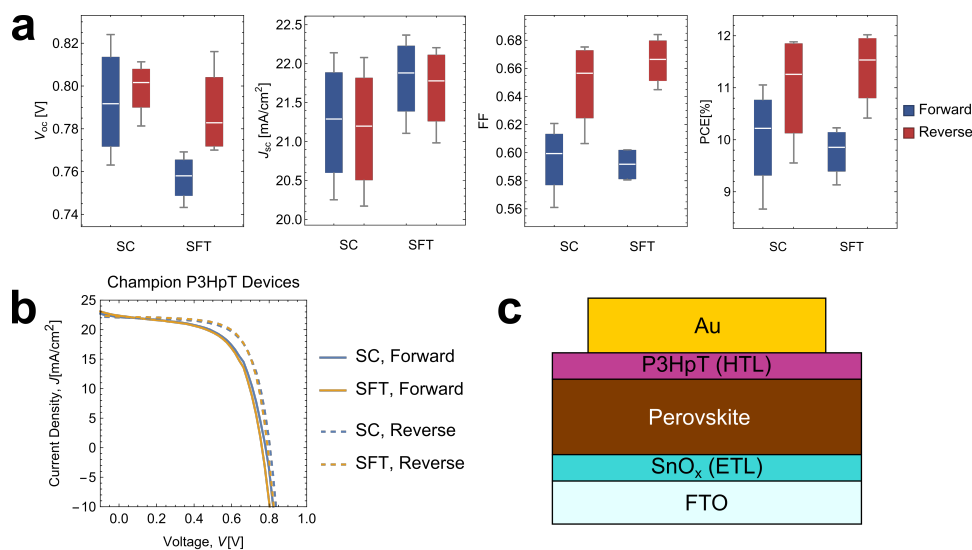
Figure 4.11. a) Photovoltaic metrics of perovskite solar cells using a P3HpT hole-transport layer deposited by solvent-free transfer (SFT) or spin-coating (SC). b) JV curves of the champion devices made using the two different deposition methods. c) Architecture of the device stack.

As expected, the films formed in a nitrogen environment, where the polymers were protected from oxidation, had an overall superior performance. Furthermore, we found that the use of chloroform to transiently plasticize the transferred polymer resulted in device improved but only for relatively short treatments (Figure 4.13. Beyond a few minutes, the chloroform began to have a deleterious impact on the devices. Lastly, we found that aging devices in a dark, inert (nitrogen) environment was beneficial for their overall performance (Figure 4.14. From the characteristic current-voltage (JV) curves, we can clearly see that aging eliminated the double diode behaviour of the devices and results in a remarking improvement to the fill factor.
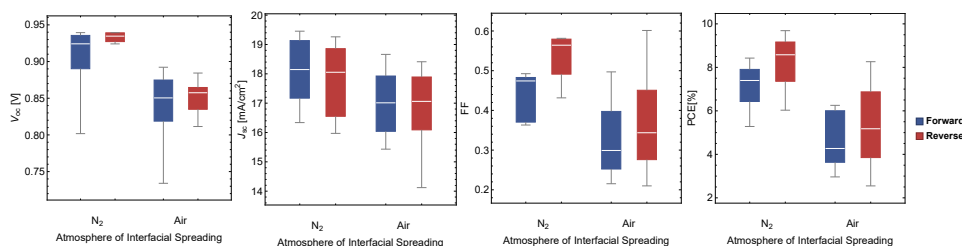
Figure 4.12. Photovoltaic metrics of perovskite cells using an SFT P3BT hole-transport layer, where the atmosphere used during film formation was either ambient air or N_2
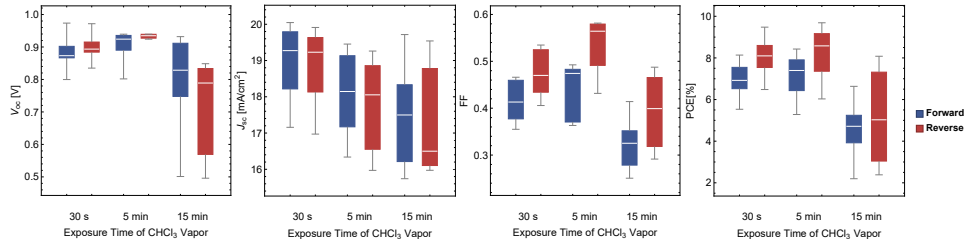
Figure 4.13. Photovoltaic metrics of perovskite cells using an SFT P3BT hole-transport layer, where the chloroform vapor exposure time was varied after the P3BT was transferred
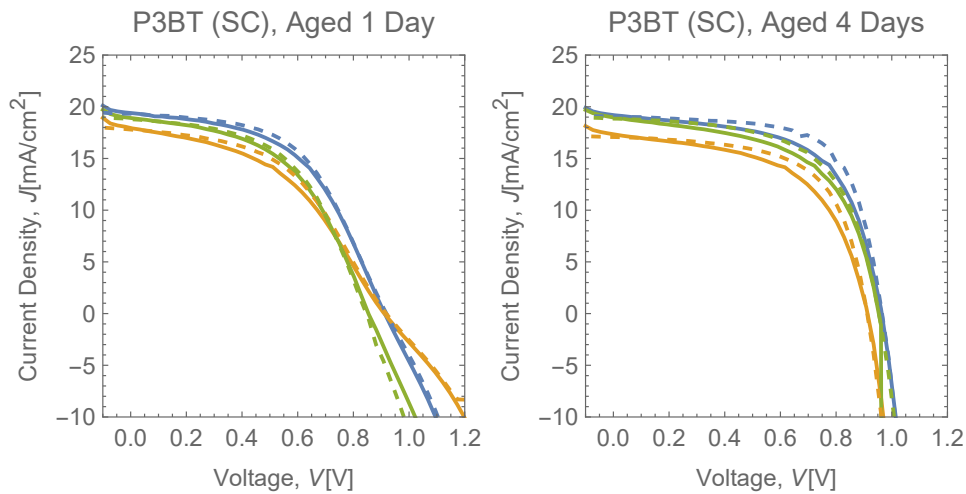
Figure 4.14. Current Density vs. Voltage sweeps of a batch of perovskite solar cells using spin-coated P3BT HTLs. The effect of aging in N_2 is shown to improve the fill-factor significantly as the "double-diode" behaviour is reduced/eliminated. This effect was consistent across P3AT batches, both for spin-coated films and those applied by SFT.

4.4 Conclusions

In summary, we have introduced a novel processing method, SFT, that leverages the mechanical robustness of conjugated polymers to form exceptionally thin, freestanding films that can be transferred onto sensitive substrates without using liquid solvents. The process is demonstrated to be amenable to large areas, and the quality of the films is assessed for uniformity by profilometry (where we found films of ca. 20 nm thickness to have a standard deviation in thickness of 5 nm or less). The films were also compared against spin-coated controls. Film roughness was assessed using SEM and AFM (where we found SFT films to be slightly smoother than the controls), surface coverage was estimated by chronoamperometry (where SFT films yields slightly better coverage than the controls.) Lastly, we implemented SFT to produce the HTLs in PSCs, which performed very comparably to those in which the HTL was fabricated by spin-coating.

In SFT, after original solidification from solution, the subsequent processing occurs in the solid phase, allowing for deposition which is free of liquid solvents and therefore fully circumvents the usual need for solvent orthogonality. In principle, SFT could work with any polymer film that is floating on the surface of water or an alternative solvent, and interfacial spreading may be the most scalable method to produce such a film.[156] Additionally, because the polymers are initially processed from solution, SFT is expected to be compatible with the vast majority of conjugated polymers in use today. We believe this process holds additional potential in roll-to-roll application as well as in enabling other processing opportunities which leverage the ability to modify the film before applying them to the desired substrate.

Chapter 4, in part, is under preparation to be submitted under the title "Solvent-free Transfer of Freestanding Large-Area Conjugated Polymer Films for Optoelectronic Applications" by Guillermo L. Esparza, Moses Kodur, Benjamin Wang, Alexander X. Chen, Rory Runser, David P. Fenning, and Darren J. Lipomi. The dissertation author was the primary investigator and author of this material.

Chapter 5

Robotic High-Throughput Screening Identifies Durable Halide Perovskite Absorbers for Tandem Photovoltaics

5.1 Introduction

The next step in the evolution of perovskite (PSK) photovoltaics is their commercial deployment.[163] While significant and rapid development has been made in single junction perovskite devices, the most direct path to commercialization is as a top cell in perovskite-silicon tandems.[164, 165] These tandem photovoltaics present an attractive route due to their high theoretical power conversion efficiencies (PCE) which can result in an overall lowered balance of system costs.[166, 167] Lead halide perovskite absorbers are uniquely positioned to serve as tandem partners given their relatively low production costs, tunable bandgaps, and sharp optical absorption edges.[8, 168, 169] However, the investigation of wide bandgap perovskites suitable for perovskite-silicon tandems ($Eg > 1.6eV$)[170, 171] has proved challenging; these absorbers typically suffer from phase segregation, especially under illumination, leading to large open-circuit voltage (V_{OC}) deficits and rapid degradation of device performance.[172] Adjustments to the intrinsic properties of perovskite absorbers (carrier mobility/lifetime, bandgap, thermal/structural stability, etc..) can be achieved through mixed perovskite absorbers.[27] Among single junction applications, the so-called "kitchen-sink" or "triple cation" family of compositions has dominated the best-

73
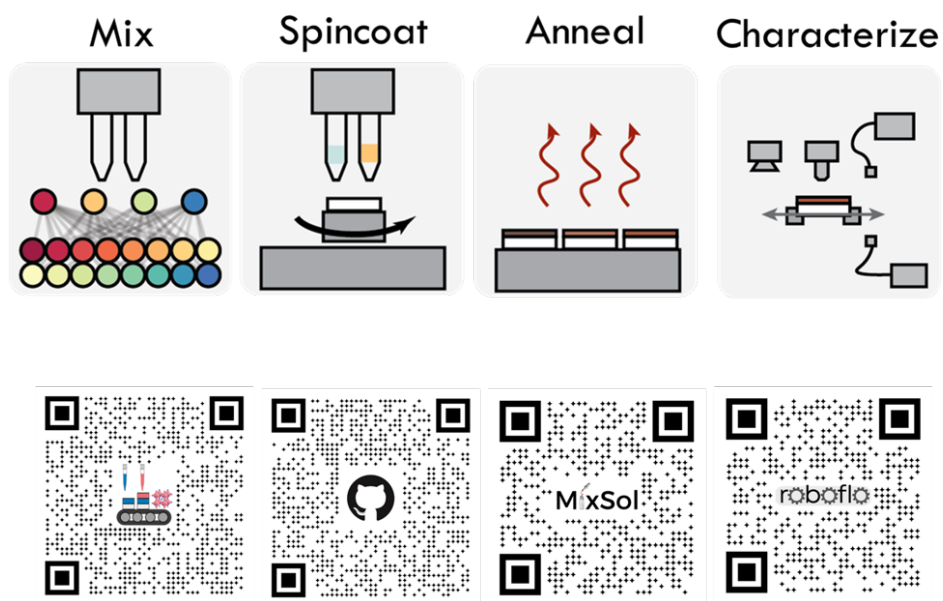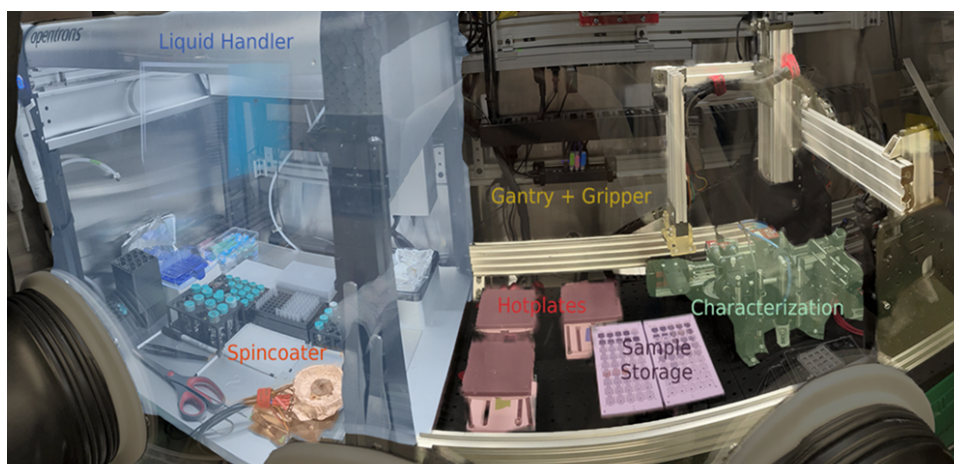
Figure 5.1. a) False-colored image of the Perovskite Automated Solar Cell Assembly Line (PASCAL) with the various hardware stations labeled. b) Workflow for a typical experiment. c) Schematics and example data for the in-line measurements taken by PASCAL.)

performing, most-repeatable, and most-stable reports.[26, 173] While some efforts have been made to discover a wide bandgap analogue to the "kitchen-sink" composition,[174] there remains a largely unexplored compositional space among $FAPbI_3$-based perovskites.

The compositional flexibility of halide perovskites present both opportunity for discovery of tailored materials and risk of extraneous effort. Whether fine-tuning compositions within known spaces, such as the the kitchen sink, or searching for greener pastures (double PSKs, pseudocations/pseudohalides, new additives, chalcogenides), the field faces a number of hurdles in screening efforts. First is the enormity of design space of halide perovskite absorbers – nearly half of the periodic table can plausibly be incorporated into the perovskite structure, making a systematic search of the space intractable. Second is the sensitivity and irreproducibility of the fabrication of perovskite thin films, owing largely to low (or even metastable) formation energies, a highly kinetic synthesis process (spincoating with an antisolvent), and inconsistency in precursor quality. These factors make it difficult to compare results across facilities whose practices may deviate in innocuous ways ranging from variability in quality of chemical precursors to sensitivity to the rate of antisolvent dispensing during spincoating.[175] Finally, the absorber is but one component of the final photovoltaic cell, and covariances between absorber composition, passivation strategies, charge transport layers, and the process parameters associated with each step explode the scale of what is ideally a global optimization problem.

This risks inherent to bold compositional searches can be ameliorated by the use of robotics. Robotic automation of experiments is growing in prevalence, improving experimental throughput and process precision. Such automation has been commonplace in drug discovery, facilitated by liquid handling hardware to execute solution-based experiments. This technology has been arbitraged for study of halide perovskite nanocrystals in solution. Automation of thin film experiments is more difficult because solid samples require more advanced hardware to manipulate than liquids; nevertheless, some examples exist of automation platforms for thin film halide perovskite research, including Ada in the Burlinguette lab[176] and AMANDA at the Institute of Materials for Electronics and Energy Technologies (i-MEET).[177] Such platforms

have been used for tasks such as optimizing hole transport layers and evaluating the dependence of absorber thermal stability on composition.[176, 178] These works, along with ours, demonstrate the value of robotic platforms for systematic study of halide perovskites.

In this work, we execute rapid experimental screening of absorber compositions using PASCAL, our robotic platform for spin-coating and characterizing halide perovskite thin films. The Perovskite Automated Solar Cell Assembly Line (PASCAL) automates fabrication of thin films by the standard spin-coating procedures employed in manual processes, albeit with precision and control surpassing that of human operators. PASCAL additionally passes samples through an in-line "characterization train", generating a standard dataset of imaging (darkfield, brightfield, and photoluminescence intensity) and spectroscopy (transmittance and photoluminescence) for each sample. With PASCAL, we fabricate and measure samples at a rate of up to 10^3 samples/day. As a proof of concept, we fabricate and test films of 83 unique compositions in the $\text{MA}_x\text{FA}_{0.78}\text{Cs}_{0.22-x}\text{Pb}(\text{I}_{0.8-y-z}\text{Br}_y\text{Cl}_z)_3$ space in under 48 cumulative hours, evaluating the films on bandgap, photoluminescence, and stability against intense illumination and thermal stress to establish the tradeoffs made between these properties across the space. From these results we divide the compositional space into four regions of durability behavior, and within each region identify Pareto-optimal compositions which promise the highest potential open circuit voltages with bandgaps closest to the 1.67 eV target for perovskite-on-silicon tandems. In summary, we offer a list of promising absorber compositions for development of top cells on silicon bottom cells, demonstrating the power of robotic screening for design of halide perovskites.

5.2 Materials and Methods

5.2.1 Preparation of Absorber Stock Solutions

Eight "endpoint" stock solutions were prepared to reach a nominal composition of $\text{MA}_x\text{FA}_{0.78}\text{Cs}_{0.22-x}\text{Pb}(\text{I}_{0.8-y-z}\text{Br}_y\text{Cl}_z)_3$, where, for (x,y,z), the solutions were (0,0.1,0), (0, 0.2, 0), (0,0,0.1), (0,0.1,0.1), (0.1,0.1,0), (0.1, 0.2, 0), (0.1,0,0.1), and (0.1,0.1,0.1). All solutions were

prepared at 1.2 M in a 3:1 volume ratio of DMF:DMSO using MAI (GreatCell), FAI (GreatCell), CsI (Sigma, 99.999%), PbI_2 (Sigma, 99.999%), $PbBr_2$ (Sigma, 99.999%), and $PbCl_2$ (Sigma, 99.999%). PbI_2 was added in 9% excess to the nominal amount. Solutions were vortexed until no solids were visible (15-20 minutes), heated to 85 °C for 10 minutes, allowed to cool down to room temperature, then filtered through a 0.20 micron filter. Finally, these eight "endpoint" solutions were mixed in a polycarbonate 96-well plate by an Opentrons OT2 liquid handler to achieve the target compositions for the screening experiments. All steps were performed within a nitrogen-filled glovebox.

5.2.2 Film Fabrication

1x1 cm glass slides were cleaned via sequential sonication steps each with a duration of 15 minutes in the following order: 5 v/v % Hellmanex (Sigma) in DI water, DI water, acetone, ethanol, and isopropyl alcohol. After drying with a filtered compressed dry air gun, the samples were treated by UV-ozone for 20 minutes under an oxygen flow of 5 scfm. Upon completion, the substrates were immediately moved into the glovebox containing the robotic platform for film deposition.

Films were fabricated by spincoating on the robotic platform. Specifically, 20 microliters of absorber solution were dispensed statically, followed by spinning at 3000 rpm for 50 seconds. 80 microliters of methyl acetate was dispensed from 2 mm above the spinning substrate at a rate of 100 microliters/second with 22 seconds remaining in the 3000 rpm spin step. After the spin completes, the sample is immediately moved to a hotplate and annealed at 100 °C for 30 minutes, and is finally moved to an aluminum-floored sample storage tray to cool to room temperature.

5.2.3 Characterization

All characterization is performed at least 3 minutes after the glass slide has moved onto the aluminum cooling tray. Once cooled, the sample is transferred to a linear stage, which carries the sample through a series of stations.

Photoluminescence

Photoluminescence spectra are acquired using a 0.9 watt 632 nm laser as an excitation source. Spectra are fit by single gaussians (cts vs eV) to extract PL intensity, center emission energy, and full-width half-max.

Transmittance

Transmission spectroscopy is used to estimate the optical bandgap using Tauc analysis[179, 180] assuming a direct bandgap material.

Photostability

Series of photoluminescence spectra are acquired at two second intervals using a focused 0.9 watt 450 nm laser as an excitation source. The focused power is equivalent to about four suns intensity. Individual spectra are fit by single gaussians (cts vs eV) to extract PL intensity, center emission energy, and full-width half-max, and these extracted parameters are compared over time to evaluate film stability.

Thermal Stability

A subset of the films are measured by transmittance and photoluminescence spectroscopy at 1.5 hour intervals over the course of heating at 85 °C on a hotplate in a nitrogen glovebox. Films are moved to the aluminum storage tray for at least 5 minutes before each measurement to cool to room temperature, measured, and then returned to the hot plate. While many samples are tracked for over 16 hours, some were dropped as early as the 6 hour measurement by the robot gripper in the course of the experiment. We therefore draw comparisons using only the first 4.5 hours shared by all tested samples.

5.3 Results and Discussion

5.3.1 PASCAL Workflow

PASCAL consists of five primary components: a liquid handler (Opentrons OT2) to mix and spincoat solutions, an array of three hotplates to anneal samples and perform thermal degradation tests, a characterization train to measure optical spectra and take images of each sample, storage trays to hold substrates and completed samples, and a carterian gantry with a parallel gripper to move samples between stations (Figure 5.1a). The spincoater was custom built to fit in one of the liquid handler deck slots such that the liquid handler can pipette directly onto it. All components are housed inside a nitrogen glovebox to enable work on halide perovskites, which are sensitive to both oxygen and humidity exposure. The overall system is controlled from one computer using a custom Python library. This library is publicly available, but is heavily tailored to PASCAL; some of the generally useful components, specifically those for planning of mixtures between stock solutions and targets and for job scheduling for parallel job execution, are available as standalone Python packages.

A typical compositional screening experiment begins with the interpolation of stock solutions into target solutions (Figure 5.1b). All compositions in our study were reached by mixing eight "endpoint" solutions that bound the compositional space, mixed in a 96-well plate by the liquid handler. Next, a glass substrate is transferred to the spincoater chuck by the robot arm. The spincoater chuck incorporates an indexed encoder such that it can be rotated to a known position, which is necessary for the parallel gripper to pick up the square sample substrates. During spincoating, PASCAL affords greater precision and recording of this critical step than is possible with human operation. The dispense height and rate are precisely controlled, and the dispense timing is repeatable to within 30 milliseconds (Figure 5.2). After spincoating, the sample is transferred to one of three hotplates (depending on the set temperature), annealed, then transferred to the storage tray to cool to room temperature prior to characterization. PASCAL's characterization line consists of cameras, LED and laser excitation sources, a halogen lamp,
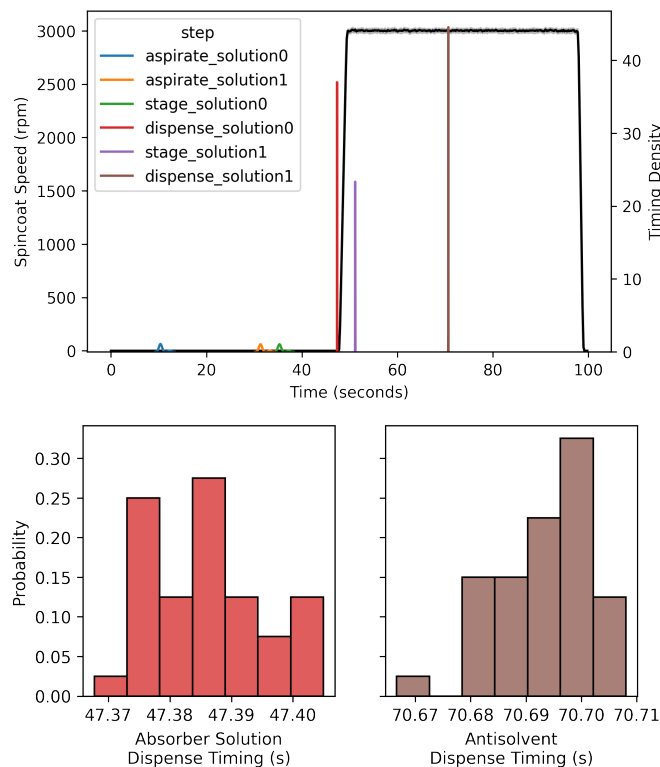
Figure 5.2. a) Representative distribution of spincoating timings over 45 samples. The black line represents the average recorded spincoating speed (rpm) vs time, with shading representing the standard deviation in rpm. The kernel density plots represent timing distributions for the steps performed by the liquid handler during spincoating, where each individual distribution is normalized such that the area under the curve is equal to one. b) histograms corresponding to the timings of the solution dispense times in a).

and a spectrometer to allow for a variety of measurements to be made. Additionally, the characterization line has a linear stage to carry one sample between the various stations, allowing sample transfers between stations during the characterization step (which can take many minutes) to be decoupled from transfers between the fabrication steps (which can occur every ten seconds or so when operating at maximum capacity). PASCAL works on many samples in parallel, with typical experiments requiring about 4 hours for fabrication and characterization of 45 samples (example job schedule in Figure 5.3).
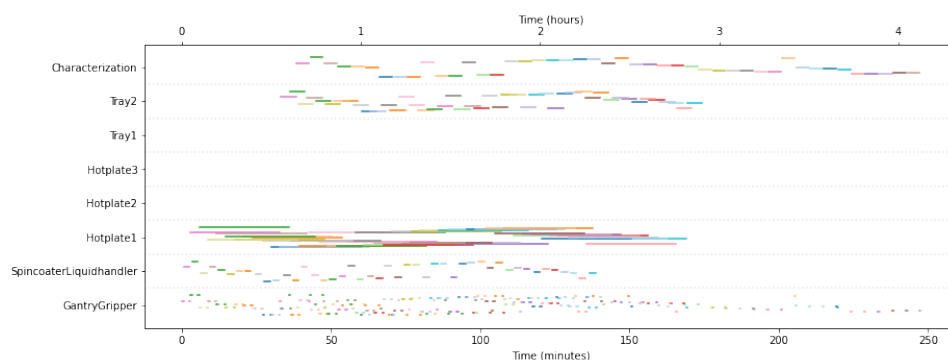
Figure 5.3. Typical job schedule for a compositional screening experiment of 45 samples. The rows correspond to the independent hardware workers in PASCAL. Colored lines indicate the duration of individual tasks on the, with each color representing a sample (note that colors repeat, as this colormap has only 20 unique colors).

The remainder of this work is a case study demonstrating the capability of PASCAL. We fabricate and test compositions over a compositional domain of interest for wide-bandgap solar absorbers, with the eventual goal of developing perovskite-on-silicon tandem cells. The data discussed were generated in two campaigns of 3-4 batches of 45 samples each. Each campaign covered the same compositional space but with different meshes, leading to irregular sampling of the total space. Nevertheless, these screening data allow us to evaluate absorber compositions on a variety of dimensions of merit prior to investing the additional effort of cell fabrication and optimization.
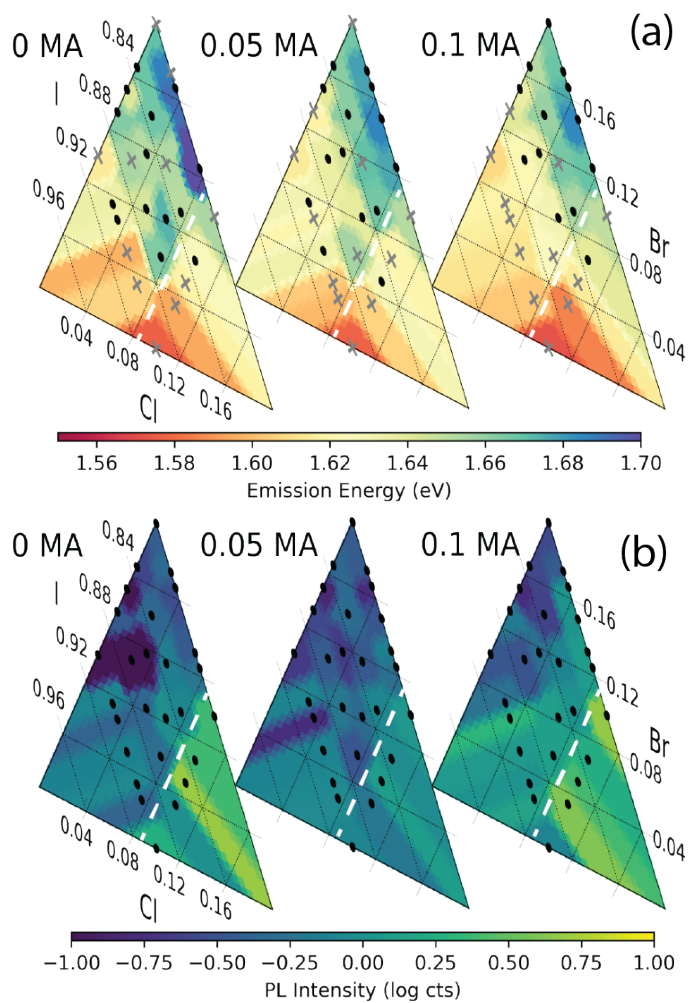
Figure 5.4. Photoluminescence a) emission energy and b) intensity for perovskite thin films across the tested compositional space. The dashed lines indicate a change in trend along the chlorine axis.

5.3.2 Photovoltaic Figures of Merit

Bandgap

The bandgap of thin films across our compositional space range from 1.55 to 1.72 eV (Figure 5.4a) which covers the spread of both the theoretically calculated and empirically tested ideal bandgaps of absorbers atop silicon in tandem devices.[170, 171, 181] The dominant trends in bandgap arise, expectedly, from variations in the halide composition at the X-site.[173, 182] Most evident is the widening bandgap with increasing bromine fraction (moving towards the top corner of the ternary diagrams). This contrasts with the non-monotonic relationship between chlorine content (moving towards the bottom right corner) which initially widens until chlorine comprises 7% of the halide content, after which the bandgap redshifts (dashed lines in Figure 5.4a). While lead bromide perovskites possess bandgaps around 2.3 eV regardless of the A-site composition, it has proven challenging to form single phase lead mixed halide perovskites when the bromine fraction is beyond 15-25% (depending on the A-site composition).[63] Reports on chlorine incorporation are scarce since absorbers for single junction application typically don't require Cl incorporation. Thus the use of this halide is typically limited to dilute doping of the seed solution with methylammonium chloride (MACl) which is expected to aid in the crystallization process of the absorber then evaporate out of the system. Our use of $MAPbCl_3$ to dope the system and the resulting phase split around a chlorine fraction of 7% is consistent with previous literature reports probing the solubility of chlorine in similar composition spaces where, past a certain percentage, chlorine addition causes compositional segregation into lower and higher chlorine regions and a net redshift in bandgap.[174] We speculate that this redshift is caused by the formation of iodine-rich phases which act as photoluminescence sinks– exactly the same as the phase splitting when the Br fraction is too high.[183] Interestingly, we observe this redshift in all 10% Cl compositions except those with the highest bromine content (10% Br) regardless of A-site composition, suggesting that the solubility limit of chlorine in this system is increased by bromine addition. The composition of the A-site also affects the material bandgap. As we

increase methyl ammonium content (and accordingly decrease cesium content), the bandgap narrows slightly likely due to octahedral tilt as the effective A-site radius is manipulated.[184]

Photoluminescence Intensity to Approximate Relative Open Circuit Voltage

The photoluminescence intensity of films across the compositional space is shown in Figure 5.4b. Transmittance spectra show that absorbance at the excitation wavelength (625 nm) does not vary across samples, implying that the photoluminescence intensity measured here is proportional to the external radiative efficiency (ERE) of the absorbers. As higher ERE is proportional to the open-circuit voltage expected from a photovoltaic cell,[185] we use these photoluminescence data to rank compositions for future cell development. Broadly, compositions with greater than 10% bromine content display poor photoluminescence intensity, and compositions with greater than 7% chlorine display the greatest photoluminescence intensity. Despite these broad trends, the actual data are rife with local maxima, and it may be the case that narrow windows in halide composition space provide opportunity for cells.

5.3.3 Absorber Durability

Photoinduced Degradation
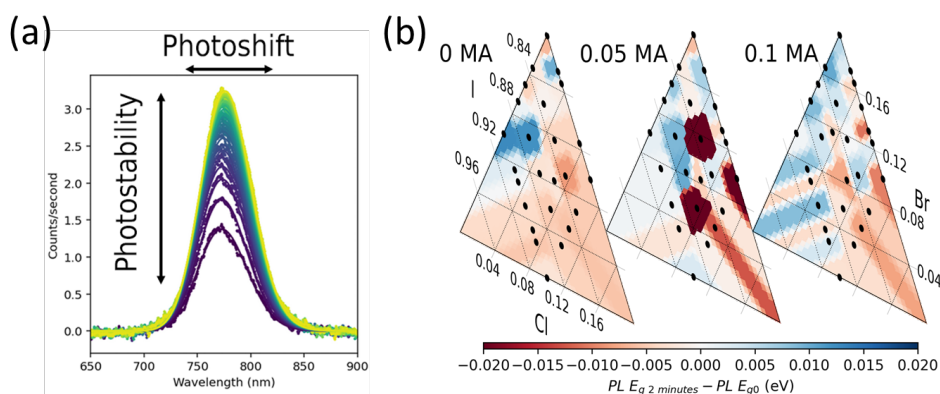
Figure 5.5. a) Example series of photoluminescence measurements and gaussian fits used to evaluate emission photostability. b) Shift in emission center after two minutes of exposure to intense (4 suns equivalent) 405 nm illumination.

We test the photostability of our thin films by recording changes in photoluminescence

84

spectra over 2 minutes of constant irradiation by a blue laser (405 nm), with power equivalent of approximately 4 suns. From these spectra, we extract the changes in both emission intensity and energy to evaluate a composition's photostability (Figure 5.5a).

Films across the composition space were seen to either "photobleach" or "photobrighten", with final photoluminescence intensities ranging from 10% to 200% of the initial intensity. We refer to this metric as photointensity. As with the PL data, the photo brightening landscape is mottled yet still reveals broad compositional trends. Compositions with $> 10\%$ bromine mostly lose emission intensity under photoexposure. All but one photobrightening composition contain chlorine, with the largest increases in emission intensity occurring in compositions with $> 5\%$ chlorine. As methylammonium loading increases, we see a slight narrowing in the distribution of intensity changes (p = 0.008 by the Brown-Forsythe test, Figure 5.6,[186]) suggesting that the A-site composition contributes to stability of emission intensity under intense illumination.[184]
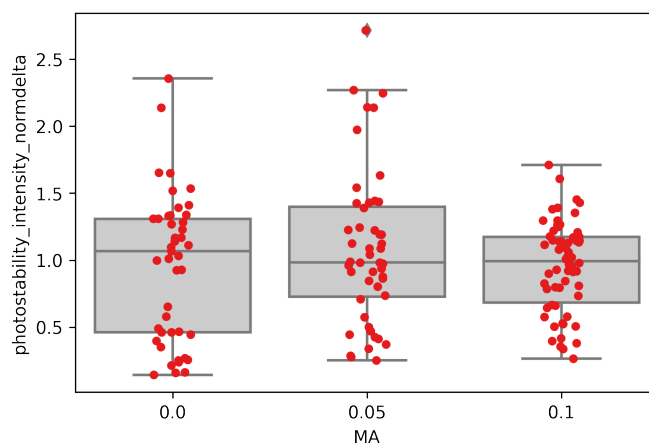
Figure 5.6. Distribution of normalized photoluminescence intensity change of films after two minutes of exposure to 4 suns equivalent 405 nm light.

Films were seen to either blueshift or redshift in emission energy under photoexposure, with all but three films shifting by less than 25 meV in either direction (Figure 5.5b). Broadly, we observe that compositions with higher chlorine fractions tend to redshift more after photoexposure (by about -10 meV per %Cl, p = 0.011, Figure 5.7).
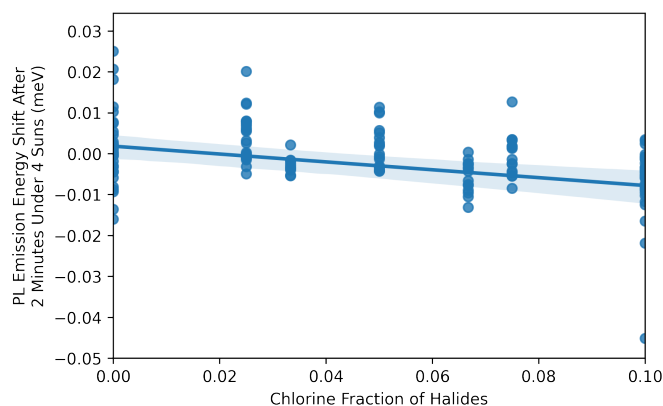
OLS Regression Results

Dep. Variable:	photostability_peakev_delta		R-squared:	0.041	
Model:	OLS		Adj. R-squared:	0.035	
Method:	Least Squares		F-statistic:	6.555	
Date:	Sat, 21 May 2022		Prob (F-statistic):	0.0114	
Time:	21:09:15		Log-Likelihood:	410.10	
No. Observations:	155		AIC:	-816.2	
Df Residuals:	153		BIC:	-810.1	
Df Model:	1				
Covariance Type:	nonrobust				

	coef	std err	t	P>|t|	[0.025	0.975]
const	0.0018	0.002	0.775	0.440	-0.003	0.006
Cl	-0.0962	0.038	-2.560	0.011	-0.170	-0.022

Omnibus:	240.767	Durbin-Watson:		2.061
Prob(Omnibus):	0.000	Jarque-Bera (JB):		20453.396
Skew:	-6.780	Prob(JB):		0.00
Kurtosis:	57.618	Cond. No.		27.2

Figure 5.7. a) Linear fit of photoluminescence emission energy shift against chlorine fraction for all films, and b) fit statistics for the regression shown in a). The points at each chlorine loading vary in bromine, chlorine, and methylammonium content.

Thermal Degradation
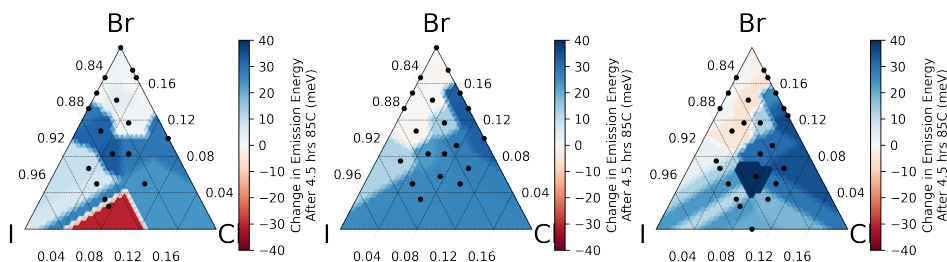
Figure 5.8. Shift in photoluminescence emission energy for films after exposure to 85 °C.

We test the thermal stability of our thin films by recording changes in photoluminescence spectra periodically during heating at 85 °C in a nitrogen environment. Photoluminescence intensity reduces for all films, with the majority of the reduction occuring after the first 1.5 hours of heating (Figure 5.10a). At 0 and 5% MA content, the films with the highest bromine fractions showed the most loss of photoluminescence intensity, dropping by up to three orders of magnitude (Figure 5.9). At 10% MA content, however, there is no clear relationship between halide composition and intensity loss. Averaging over all halide compositions, higher methylammonium content leads to greater losses in photoluminescence intensity after thermal degradation.
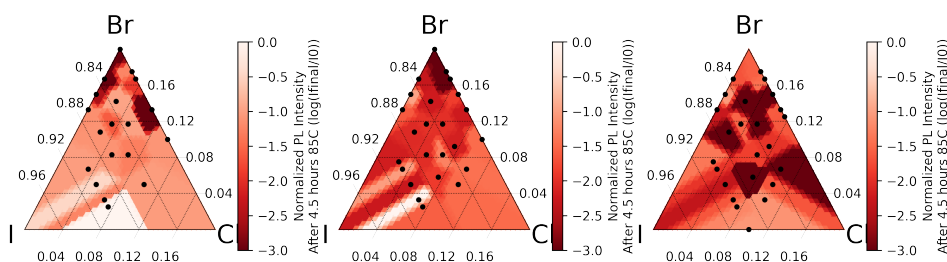
Figure 5.9. Normalized photoluminescence intensity of films after 4.5 hours of exposure to 85 °C under a nitrogen environment. Darker red here represents a greater loss of intensity.

Emission energy is seen to either redshift or blueshift, with the rate of shift varying across compositions as well (Figure 5.10b). Most films blueshifted, with those with 5% or higher chlorine loading show the largest blueshift (up to 40 meV after 4.5 hours, Figure 5.8). Films with over 10% bromine and under 5% chlorine slightly redshifted (up to 10 meV after 4.5 hours).

87
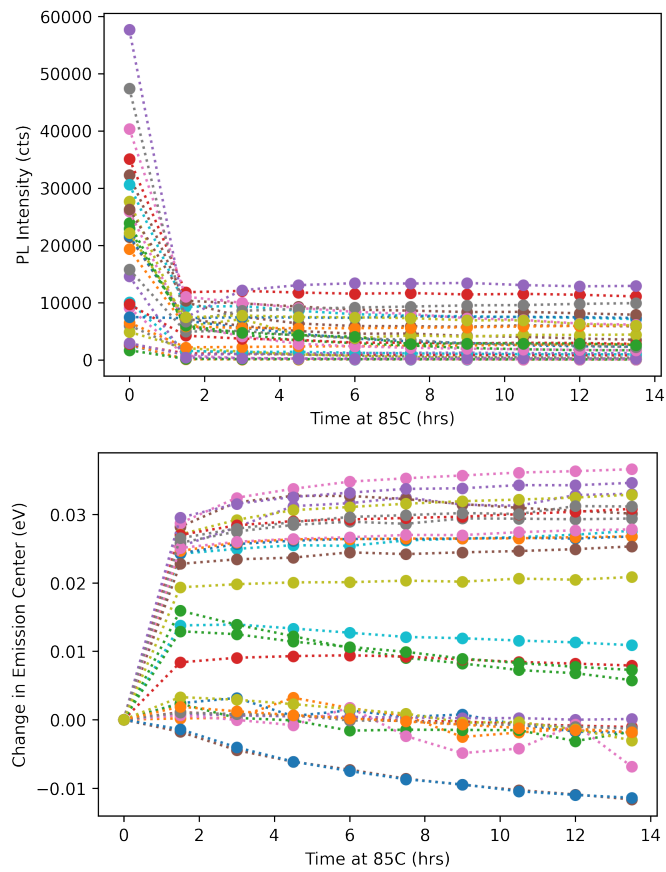
Figure 5.10. a) Photoluminescence intensity and b) change in emission energy for films of various compositions undergoing thermal degradation at 85 °C in a nitrogen environment.

The methylammonium content was not seen to have an effect on emission energy shifts during thermal degradation, likely due to the moderate 85°C temperature applied.

5.3.4 Parsing the Screening Data
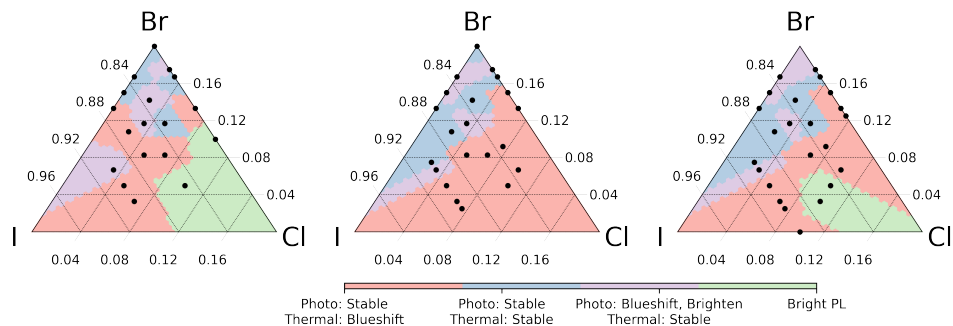
Figure 5.11. Segmentation of the compositional space into four distinct behavior regions, labeled on the colorbar. The broad behavioral trends for the four regions are labeled in on the colorbar: the red, blue, and purple regions are distinct in their response to photo and thermal stress, whereas the green region displays uniquely high photoluminescence intensity.

Segmenting the Compositional Space into Regions of Distinct Behavior

The screening data provide multiple dimensions over which the tested absorber compositions can be compared. We use K-Means Clustering (KMC) to segment the overall compositional space into four regions of distinct behavior. Specifically, we select five screening metrics which capture the durability and potential performance of the absorbers: thermal stability (by changes in emission intensity and energy), photostability (by changes in emission intensity, and energy), and the initial photoluminescence intensity (Figure 5.12). The number of clusters was selected by trial-and-error – fewer than four clusters grouped disparate compositions together, while greater than four clusters only divided clusters in spurious ways that were not meaningful in our context of absorber screening. Note that the composition was not used for clustering, and that KMC does not require clusters to be contiguous in the compositional space; that KMC naturally partitioned the compositional space into four contiguous regions suggests that the total screening data vary smoothly as composition is changed.
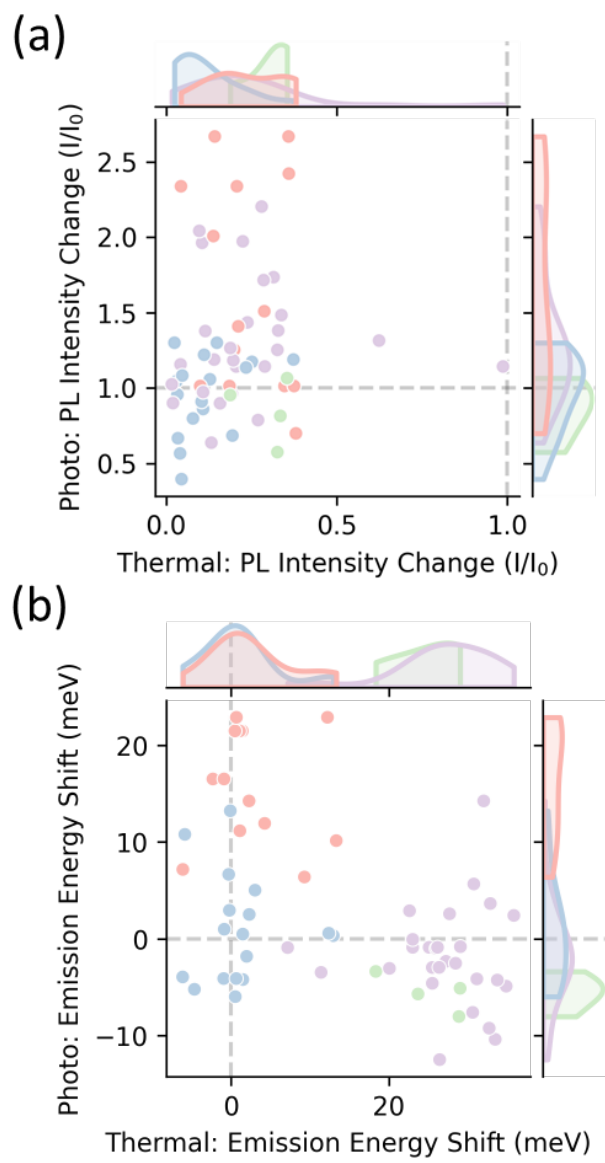
Figure 5.12. Scatterplots representing the 4 durability dimensions on which K-Means Clustering was performed to segment the compositional space into four distinct regions. Each point represents a unique absorber composition and is colored by the cluster to which that composition is assigned. The top plot displays emission energy shifts under thermal and photo degradation, while the bottom plot shows normalized emission intensity changes under thermal and photo degradation.

From the clustering process, we identify four distinct regions of absorber behavior, two of which are particularly interesting for tandem development. First, we see that many absorbers with the highest (10%) chlorine content have sufficiently high photoluminescence intensity to distinguish them from the rest of the compositions (green region in Figure 5.11). The remaining three regions are distinguished not by photoluminescence intensity, but by absorber stability against thermal and photo stressors. Compositions with over 4% chlorine tend to have a stable emission center under photoexposure, but blueshift in emission under heating. At lower chlorine loadings, the films have a stable emission energy under heating; of these compositions, some are also stable under photoexposure (blue regions), while the others blueshift and brighten in emission under photoexposure (purple regions). The purple regions exist at the boundary between blue and red regions, suggesting that the photobrightening emission behavior is a transitional property between thermally stable and thermally unstable compositions.

The methylammonium content on the absorber's A-site plays a significant role in shifting the boundaries of these four behavior regions. Most notably, the stable blue region grows with increasing methylammonium (10%) content, reducing the thermally unstable red region accordingly. The green "bright photoluminescence" region does not move with methylammonium loading, suggesting that this brightening effect is more a consequence of the halide fraction than the A-site composition.

Pareto-Optimal Compositions Within Each Segment

Armed with a segmented compositional space, we use our two main photovoltaic figures of merit – bandgap and photoluminescence intensity – to identify from each segment the most interesting compositions for investigation in perovskite-on-silicon tandems. Specifically, we select pareto-optimal compositions from each compositional segment, optimizing for proximity to the target top-cell bandgap (1.67 eV) and photoluminescence intensity (which suggests the potential open-circuit voltage of the absorber in a tandem cell) (Figure 5.13). The compositions we suggest for further exploration are given in Table 5.1.
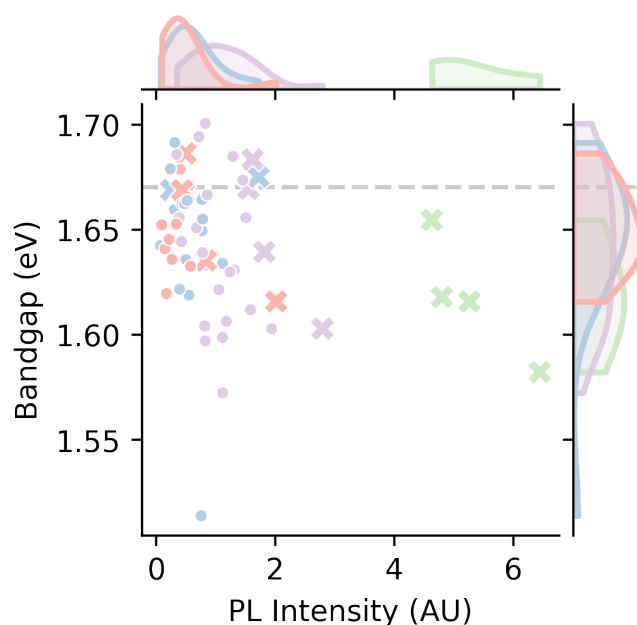
Figure 5.13. Pareto front scatterplots for the four clusters. Crosses are the pareto optimal points, and dots are the dominated points. The horizontal dashed line represents the target bandgap, the distance to which we minimize in our pareto optimization.

Table 5.1. "Most interesting" compositions from each segment of the compositional space as identified from pareto analysis.

Region	MA	I	Br	Cl	Eg (eV)	PL (a.u.)
Bright PL	0.1	0.867	0.033	0.1	1.582	6.450
	0.1	0.85	0.05	0.1	1.616	5.268
	0	0.85	0.05	0.1	1.618	4.806
	0	0.8	0.1	0.1	1.654	4.639
Photo, Thermal: Stable	0	0.833	0.167	0	1.669	0.258
	0.1	0.8	0.167	0.033	1.675	1.725
Photo: Blueshift, Thermal: Stable	0.1	0.9	0.067	0.033	1.616	2.021
	0.1	0.85	0.117	0.033	1.635	0.843
	0	0.833	0.142	0.025	1.667	0.475
	0.1	0.8	0.175	0.025	1.669	0.440
	0	0.8	0.175	0.025	1.686	0.498
Photo: Stable, Thermal: Blueshift	0.1	0.9	0.033	0.067	1.603	2.800
	0.1	0.833	0.067	0.1	1.639	1.826
	0.1	0.8	0.125	0.075	1.669	1.556
	0.1	0.8	0.133	0.067	1.683	1.627

5.3.5 Reliability of the Screening Data

One of the primary value propositions of robotics for lab automation is superhuman precision and repeatability. This is especially critical in the investigation of halide perovskites, which suffer from repeatability issues due to a variety of factors. The processing window for typical perovskite film fabrication is small, owing to the kinetic nature of the antisolvent-based crystal formation process. Slight variations in the spincoating procedure, such as the timing and rate of antisolvent dispensal, can significantly affect the behavior of resulting films.[187–189] The solid precursors used to fabricate perovskite thin films vary in quality from lot to lot, with potentially outsize influences on the performance of the films.[175]
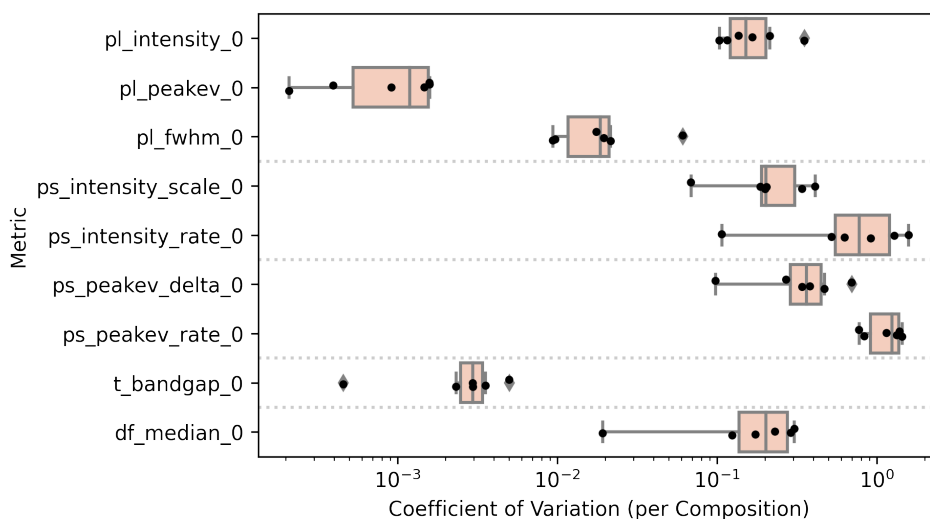
Figure 5.14. Distributions of coefficients of variation (CV) for features extracted from measurements on the PASCAL characterization line. Each dot represents the CV for five films fabricated and tested of a single composition. The box plots therefore show the distribution of CV for each of the features labeled on the y-axis. Features between the dotted lines are extracted from the same characterization mode. From top to bottom, the features are: 1) intensity, 2) emission energy, and 3) full-width half max of the photoluminescence spectra. 4) normalized intensity (I/I_0), 5) rate of intensity change (k from an exponential decay fit $I = I_0 e^{-k/T}$), 6) change in emission energy $(E - E_0)$, and 7) rate of energy change across two minutes of exposure to 4 suns 405 nm light. 8) bandgap of the films, measured from Tauc analysis of transmittance spectra. 9) a metric of film roughness from the darkfield imaging.

These problems are avoided in our robotic workflow, in which are able to maintain

93

precise control over all aspects of fabrication (Figure 5.2) and complete all experiments with small volumes of solutions generated from the same lot of precursors. Despite these factors, we still observe some variation in the films made by PASCAL. We evaluate repeatability by the coefficient of variation (CV) in various measurements of five films each of six unique compositions within our compositional space (Figure 5.14). Measures of material bandgap are most consistent, with average CV of 0.1% for photoluminescence emission energy and 0.3% for optical bandgap estimated from transmittance data. The intensity of photoluminescence varies with an average CV of 10%; this greater variation is to be expected, as radiative recombination rates within the films are sensitive to interfaces and defect states that do not affect the bulk material bandgap. More variable still are the measures of photostability. The magnitude of intensity or emission energy changes vary with CV's of 20-30%, while the rates of these changes vary with CV's of 70-100%. We expect that these photostability measures are driven by the nature of the film surfaces, as isolated tests of photostability before and after a surface treatment with phenethylammonium iodide (PEAI) show the surface passivation agent to greatly stabilize the film under photoexposure.

5.4   Conclusion

Our experimental screening results lay the foundation for informed development of wide bandgap halide perovskite absorbers for perovskite-on-silicon tandems. We confirm that chlorine addition does widen the absorber bandgap to a point, identifying a solubility limit of chlorine in our "kitchen-sink" inspired compositional space. Many compositions are shown to have suitable bandgaps for top cells, using addition of bromine, chlorine, or both to the prototypical iodine perovskite. A small amount of chlorine addition greatly increases the photoluminescence, implying that chlorine addition is important to maximize the open-circuit voltage of top cells. Too much chlorine, however, reduces the thermal stability of the films. Using the photoluminescence intensity, photostability, and thermal stability, the tested compositions broadly fall into four

regions of behavior, within each we have co-optimized bandgap and photoluminescence intensity to identify the most promising absorber compositions for further investigation.

Beyond the screening results, our work shows the value of automation in investigation of halide perovskites. The total data discussed in this work were acquired over about 48 hours of machine time using about 10 milliliters of precursor solutions. The throughput, material efficiency, and process precision afforded by PASCAL mitigate practical issues of variability in precursors, degradation of stock solutions, and operator error that plague studies of spincoated halide perovskites. These factors provide us with confidence that the trends identified by our screening reflect composition-driven material behavior.

Chapter 5, in part, is under preparation to be submitted under the title "Robotic High-Throughput Screening Identifies Durable Halide Perovskite Absorbers for Tandem Photovoltaics" by Rishi E. Kumar, Moses Kodur, Deniz N. Cakan, Jack Palmer, Apoorva Gupta, Eric Oberholtz, Sean P. Dunfield, David P. Fenning. The dissertation author was the primary investigator and author of this material.

Chapter 6

Summary and Outlook

Given their rapid development and early success, the future of perovskite photovoltaics is very bright. However, they still possess significant shortcomings that have hampered their commercial acceptance.

In Chapter 2, we tested an encapsulation scheme that had been widely proposed in the literature and found that it was not a sufficient air/moisture barrier for perovskite materials. Unfortunately, while graphene promises many exciting applications, the relatively small grain size of high quality CVD-graphene contains too many diffusion pathways for damp air and/or volatile perovskite species that ultimately lead to their complete degradation. Further, the lack of toughness (different from strength) of poly-crystalline graphene makes it susceptible to fracture during the extra handling that is required to prepare graphene stacks. Therefore, at this time, graphene is not a suitable encapsulation material for large-area perovskite films. Instead, we found that glass-glass encapsulation (similar to silicon photovoltaics) is a promising pathway forward for perovskite encapsulation. While others have previously used a glass-glass encapsulation with a PIB edge seal, our low-temperature application ($< 100°$C) presents a pathway by which compositions with less thermal stability could be encapsulation. Further, our results suggest that the volatilization of thermally unstable species, such as MA, is suppressed, even after > 1000 hours at 85 °C, due to the build up of MA vapor in the limited head space of the encapsulated film. Further work is needed to test encapsulated devices in real world

conditions to verify that the laboratory results translate to practical and real systems.

In Chapter 3, we showed how simple (and cheap!) electrochemical tools can be leveraged to screen transport layers. Through cyclic voltammetry, we were able to establish a feedback loop by which the repeatability, relative charge collection energies, and surface coverage of tin oxide could be quickly evaluated. Importantly, these metrics could be directly correlated with the final devices batches highlighting its utility for early screening of perovskite photovoltaics aiding in both the development of new materials and the process control of established recipes. Further, we showed that chronoamperometry could be used to determine the relative reactivity at the surface of tin oxide films. This was shown to indicate the oxidation state at the surface of tin oxide and we speculate that is can be used to predict the interfacial durability between tin oxide and perovskites. While this was demonstrated on tin oxide, the same principles were later leveraged to support the work presented in Chapter 4 on conjugated polymers showing the diverse application of these electrochemical tools.

In Chapter 4, we designed a solvent-free transfer mechanism by which conjugated polymers could be transferred on top of perovskite solar cells. This prevents degradation to the absorber caused by harmful solvents and presents a pathways to deposit ultra-thin, large-area conjugated polymers to be used as transport layers in a perovskite solar cell. In our devices, the solvent-free transfer films exhibited significant hysteresis. This could be caused by a poor interface between the perovskite and the polymer. This effect was largely mitigated by aging in an inert environment suggesting that it is not a fundamental limitation of the architecture or transfer technique. Further work is needed to improve the post deposition treatment to ensure better contact or implement an interlayer which anchors the perovskite to the hole transport layer. Adapting this scheme for other materials such as Poly-TPD, PTAA, or n-type conjugated polymers and applying it to textured substrates, such as silicon, could further advance the utility of the solvent-free transfer method by aiding in the development of silicon-perovskite tandem cells.

In Chapter 5, we present our robotic perovskite fabrication and characterization tool.

The high throughput capability of this tool allows a wide variety of experiments including an investigation of over 80 compositions in a single run. We leverage the capacity of the robot to study the compositional space of a triple cation, triple halide perovskites to be used as wide bandgap absorbers. Within our search space, we found that the bandgap increases monotonically as bromine and iodine are increased but that a clear extrema is presented with chlorine incorporation. This agreed with previous reports which suggested that too much chlorine induces phase segregation. Additionally, we showed that PL brightness increased with MA and Cl incorporation and that several compositions exhibit resilience to illumination or thermally induced degradation. Using a pareto-optimal analysis, we identified several promising compositions that were advanced to the device making stage. These devices were found to perform in excess of 16% PCE. While the devices exhibited J_{SC} and FF values that were close to expected, the V_{OC} was still low as is typical with wide bandgap materials. To address these shortcomings, PASCAL (the robot) can be used to quickly screen through materials which can passivate the PSK and ETL interface– removing recombination centers and improving the V_{OC}.

Through each of these contributions, our collective understanding of these materials has progress a little further and the capability of my team to produce high-quality devices has increased. With that, I pass on my knowledge to the next generation of scientist and engineers who have picked up the mantle. Perovskite have come a long way especially in the past 13 years but there is still work to be done.

As Thomas Edison stated, "We are like tenant farmers chopping down the fence around our house for fuel when we should be using Natures inexhaustible sources of energy – sun, wind and tide. ... I'd put my money on the sun and solar energy. What a source of power! I hope we don't have to wait until oil and coal run out before we tackle that."

At the end of the day, solar will win out in the energy race and I have no doubt that perovskite will play a pivotal role in their advancement.

Appendix A

Supplementary Notes

A.1 Calculation of Air Permeability

Calculation of the air permeability begins with the ideal gas law:

$$PV = nRT \tag{A.1}$$

Taking the derivative with respect to time, pulling out constants, and rearranging yields:

$$\frac{d}{dt}(PV) = \frac{d}{dt}(nRT) \tag{A.2}$$

$$V\frac{dP}{dt} = RT\frac{dn}{dt} \tag{A.3}$$

$$\frac{dn}{dt} = \frac{V}{RT}\frac{dP}{dt} \tag{A.4}$$

Where V = 5 cm^3 (volume of internal chamber in pressure sensor), T = 295 K (air temperature), R = 8.314 $\frac{m^3 \cdot Pa}{mol \cdot K}$ = 62.36 $\frac{L \cdot torr}{mol \cdot K}$ and

$$\frac{dP}{dt} = \left(\frac{1}{\left(\frac{\Delta P}{\Delta T}\right)_{barrier} - \left(\frac{\Delta P}{\Delta T}\right)_{nobarrier}} - \frac{1}{\left(\frac{\Delta P}{\Delta T}\right)_{leak}}\right)^{-1} \tag{A.5}$$

where the measurements of $(\frac{\Delta P}{\Delta T})_{barrier}$, $(\frac{\Delta P}{\Delta T})_{nobarrier}$, and $(\frac{\Delta P}{\Delta T})_{leak}$ are shown in Figure 2.11.

Extracting these values from their least square-fit trendlines, we obtain the following values:

Table A.1. Calculated values of $\frac{\Delta P}{\Delta t}$ and $\frac{dP}{dt}$ extracted from regions of linear change in pressure over time.

Sample	$\frac{\Delta P}{\Delta t} [\frac{torr}{s}]$	$\frac{\Delta P}{\Delta t} [\frac{torr}{h}]$	$\frac{dP}{dt} [\frac{torr}{h}]$
0L	—	0.0535	0.0489
1L	—	0.0078	0.0031
2L	—	0.0061	0.0014
3L	—	0.0072	0.0025
Leak	0.6751	1.87 x 10^{-4}	—
No Barrier	—	0.0047	—

Lastly, converting to conventional permeability units of $\frac{cm^3 of air at STP}{cm^2 \cdot day}$ and accounting for the circular opening in the rubber spacer with diameter 6.0 mm gives:

Table A.2. Calculated values of $\frac{\Delta P}{\Delta t}$ and $\frac{dP}{dt}$ extracted from regions of linear change in pressure over time.

Sample	Air Permeability ($\frac{\Delta P}{\Delta t}$ and $\frac{dP}{dt}$)
0L	2.73
1L	0.078
2L	0.078
3L	0.140

A.2 Calculating Conduction Band Positions

The electron concentration in a semiconductor can be expressed as the product of the electron density of states and the Fermi function integrated from the conduction band minimum to the top of the conduction band.[190] Making the parabolic band approximation, we can write the electron concentration as shown in Equation A.6. After accounting for the contribution to capacitance from the Helmholtz layer, we know from Mott-Schottky analysis that these films

are highly-doped. Using Fermi-Dirac statistics, rather than the typical Maxwell-Boltzmann approximation, this equation must be numerically integrated at non-zero temperatures.[191]

$$n_e = \int_{E_{CBM}}^{\infty} D_c(E) f(E) dE = \frac{1}{2\pi^2} \left(\frac{2m_e}{2}\right)^{\frac{3}{2}} \int_{E_{CBM}}^{\infty} (E - E_{CBM})^{\frac{1}{2}} \frac{1}{e^{\frac{E-E_f}{K_B T}} + 1}$$

(A.6)

where m_e is the effective mass of electrons in SnO_x and taken to be 0.3,[190, 191] is the Planck constant, E is energy, E_{CBM} is the energy of the conduction band minimum, E_f is the Fermi energy (parameterized by Mott-Schottky for each anneal condition), k_B is the Boltzmann constant, and T is the temperature (300K). Because the highest doping concentration determined here is on the order of approximately 10^{19} cm^{-3}, the assumption of a parabolic band yields a reasonable approximation. The error in using the Mott-Schottky analysis of capacitance voltage, which does not account for Fermi-Dirac statistics, is also small in the limit of weak degeneracy (i.e., below carrier concentrations of $5x10^{20}$ cm^{-3}).[192] Equation A.6 was solved utilizing numerical integration and the results for each condition are plotted in Figure 3.7a. The results are summarized in Figure 3.7b which shows that the estimated conduction band of the SnO_x is indeed changing. Thus, we conclude that our tracking of cathodic current onset in CV probes not just the changing flatband potential but also a change in the alignment of the conduction band minimum.

A.3 XPS-based O:Sn Calculations

In the absence of any contaminants the oxygen to tin ratio (O:Sn) can be calculated by scaling the area of the oxygen 1s (O 1s) spectral region by its relative sensitivity factor (RSF) and then dividing by the RSF scaled tin $3d_{5/2}$ (Sn $3d_{5/2}$) area:

$$O : Sn = \left(\frac{O1sArea}{O1sRSF}\right)\left(\frac{Sn3d_{5/2}Area}{Sn3d_{5/2}RSF}\right)^{-1}$$

(A.7)

However, when oxygen bearing contaminants are involved, their contribution from the O 1s signal must be removed. This requires scaling by the ratio of the RSF of the core levels as well as the elemental ratios of the expected bonds. While the former is well known and tabulated for various instruments, the latter requires some assumptions. For our work, we assumed that carbon 1s (C 1s) was from a mixture of COx states, detailed elsewhere, with the relevant species for this study below:[5]

Contaminant Peak and Species Breakdown:

1. Main Peak ($0.8 < \text{FWHM}_A < 2.0$)

   - C-C

   - C-H

2. Peak at A + 1.4 eV to 1.6 eV ($\text{FWHM}_B = \text{FWHM}_A$)

   - R_3C-OH

   - R_3C-O-CR_3

   - R-(C=O)-O-C*R_3

3. Peak at A + 3.7 eV to 4.3 eV ($\text{FWHM}_C = \text{FWHM}_A$)

   - R-(C*=O)-O-CR_2

   - R-(C*=O)-OH

Where R is an alkyl or hydrogen species. We then used the assumptions:

1. The amounts of the two components of C will be equally split between the two species.

2. The amounts of the two components B(1) and B(2) will be equally split between the two species. Thus, the C:O ratio for these combined peaks will be 3:2.

to calculate the respective C:O ratios. This resulted in:

$$O \ 1s \ from \ CO_x = 0 \cdot C_A + 1.5 \cdot C_B + \frac{2}{3}(C_C - \frac{C_B}{2}) \qquad (A.8)$$

To subtract the other contaminates from the O 1s, we assumed that the silicon (Si), calcium (Ca), and sodium (Na) were from soda lime glass and therefore were in the SiO_2, Na_2O, and CaO states with X:O ratios of 1:2, 2:1, and 1:1 respectively. To calculate the Sn:O ratio, we then replace the O 1s Area with O 1s Area*, where:

$$O \ 1s \ Area* = O \ 1s \ Area - \sum_i contaminate_i \ area \cdot \frac{O \ 1s \ RSF}{contaminate_i \ RSF} \cdot ratio \ multiplier_i \qquad (A.9)$$

$$O \ 1s \ Area* = O \ 1s \ Area - \sum_i contaminate_i \ area \cdot total \ multiplier_i \qquad (A.10)$$

We note that the following RSF ratio, area multipliers, and total multipliers are below:

Table A.3. RSF, Ratio Multipliers, and Total Multipliers for contaminant species.

Element	RSF Ratios (O:X)	Ratio Multiplier	Total Multiplier
CA	0.400	1	0.4
Na	0.435	0.5	0.22
Si	2.235	2	4.47

Using the above formulas, multipliers, and an area fit with a linear background (due to the low signal to noise), we calculated the following ratios for each of the contaminants removed individually, and together (-all):

Raw data for O 1s and contaminates are in Figure 3.15. Deconvoluted C 1s core levels are plotted in Figure 3.15 while the final ratios with everything subtracted (-all column) are plotted in main text Figure 3.19d alongside the Sn $3d_{5/2}$ binding energy shifts.

Table A.4. Summary of oxygen contaminants.

	% CO_x	% SiO_2	% CaO	% SnO_x
As-dep	8.3	26.5	0.4	35.2
180°C	7.2	9.8	0.8	17.8
190°C	13.7	13.6	2.5	29.7
200°C	6.9	25.5	0.4	32.8

Table A.5. Calculations for O:Sn ratio for each tin oxide sample with O contamination removal.

	O	-CO_x	-SiO_2	CaO	-all
As-dep	2.45	2.25	1.80	2.44	1.59
180°C	2.16	2.00	1.94	2.14	1.77
190°C	2.52	2.18	2.18	2.46	1.77
200°C	2.63	2.45	1.96	2.62	1.77

Bibliography

[1] National Renewable Energy Laboratory (NREL). Best Research-Cell Efficiencies, 2022.

[2] Fengyu Zhang, J. Clay Hamill, Yueh-Lin Loo, and Antoine Kahn. Gap States in Methylammonium Lead Halides: The Link to Dimethylsulfoxide? *Advanced Materials*, 32(42):2003482, oct 2020.

[3] Juan Tirado, Manuel Vásquez-Montoya, Cristina Roldán-Carmona, Maryline Ralaiarisoa, Norbert Koch, Mohammad Khaja Nazeeruddin, and Franklin Jaramillo. Air-Stable n–i–p Planar Perovskite Solar Cells Using Nickel Oxide Nanocrystals as Sole Hole-Transporting Material. *ACS Applied Energy Materials*, 2(7):4890–4899, jul 2019.

[4] Allen J. Bard and Larry R. Faulkner. *Electrochemical Methods: Fundamentals and Applications*. John Wiley Sons, Ltd, New York, NY, 2nd editio edition, 2001.

[5] B.P. Payne, M.C. Biesinger, and N.S. McIntyre. X-ray photoelectron spectroscopy studies of reactions on chromium metal and chromium oxide surfaces. *Journal of Electron Spectroscopy and Related Phenomena*, 184(1-2):29–37, feb 2011.

[6] Alessio Bosio, Stefano Pasini, and Nicola Romeo. The History of Photovoltaics with Emphasis on CdTe Solar Cells and Modules. *Coatings*, 10(4):344, apr 2020.

[7] Enhanced long-term stability of perovskite solar cells by passivating grain boundary with polydimethylsiloxane (PDMS). *Journal of Materials Chemistry A*, 7(36):20832–20839, 2019.

[8] Stefaan De Wolf, Jakub Holovsky, Soo Jin Moon, Philipp Löper, Bjoern Niesen, Martin Ledinsky, Franz Josef Haug, Jun Ho Yum, and Christophe Ballif. Organometallic halide perovskites: Sharp optical absorption edge and its relation to photovoltaic performance. *Journal of Physical Chemistry Letters*, 5(6):1035–1039, 2014.

[9] Jun Hong Noh, Sang Hyuk Im, Jin Hyuck Heo, Tarak N. Mandal, and Sang Il Seok. Chemical management for colorful, efficient, and stable inorganic-organic hybrid nanostructured solar cells. *Nano Letters*, 13(4):1764–1769, 2013.

[10] Qingfeng Dong. DigitalCommons @ University of Nebraska - Lincoln Electron-hole diffusion lengths ¿ 175 μ m in solution-grown CH 3 NH 3 PbI 3 single crystals. *Science*, 347(6225):967–970, 2015.

[11] Henry J Snaith. Perovskites: The Emergence of a New Era for Low-Cost, High-Efficiency Solar Cells. *The Journal of Physical Chemistry Letters*, 4(21):3623–3630, nov 2013.

[12] Samuel D Stranks, Giles E Eperon, Giulia Grancini, Christopher Menelaou, Marcelo J P Alcocer, Tomas Leijtens, Laura M Herz, Annamaria Petrozza, and Henry J Snaith. Electron-Hole Diffusion Lengths Exceeding 1 Micrometer in an Organometal Trihalide Perovskite Absorber. *Science*, 342(6156):341–344, oct 2013.

[13] Molang Cai, Yongzhen Wu, Han Chen, Xudong Yang, Yinghuai Qiang, and Liyuan Han. Cost-Performance Analysis of Perovskite Solar Modules. *Advanced Science*, 4(1):1600269, jan 2017.

[14] Severin N. Habisreutinger, Tomas Leijtens, Giles E. Eperon, Samuel D. Stranks, Robin J. Nicholas, and Henry J. Snaith. Carbon Nanotube/Polymer Composites as a Highly Stable Hole Collection Layer in Perovskite Solar Cells. *Nano Letters*, 14(10):5561–5568, oct 2014.

[15] Luis K Ono, Emilio J. Juarez-Perez, and Yabing Qi. Progress on Perovskite Materials and Solar Cells with Mixed Cations and Halide Anions. *ACS Applied Materials Interfaces*, 9(36):30197–30246, sep 2017.

[16] Jon M. Azpiroz, Edoardo Mosconi, Juan Bisquert, and Filippo De Angelis. Defect migration in methylammonium lead iodide and its role in perovskite solar cell operation. *Energy Environmental Science*, 8(7):2118–2127, 2015.

[17] Maithili K. Rao, D.N. Sangeetha, M. Selvakumar, Y.N. Sudhakar, and M.G. Mahesha. Review on persistent challenges of perovskite solar cells' stability. *Solar Energy*, 218(July 2020):469–491, apr 2021.

[18] Jaeki Jeong, Minjin Kim, Jongdeuk Seo, Haizhou Lu, Paramvir Ahlawat, Aditya Mishra, Yingguo Yang, Michael A. Hope, Felix T. Eickemeyer, Maengsuk Kim, Yung Jin Yoon, In Woo Choi, Barbara Primera Darwich, Seung Ju Choi, Yimhyun Jo, Jun Hee Lee, Bright Walker, Shaik M. Zakeeruddin, Lyndon Emsley, Ursula Rothlisberger, Anders Hagfeldt, Dong Suk Kim, Michael Grätzel, and Jin Young Kim. Pseudo-halide anion engineering for α-FAPbI3 perovskite solar cells. *Nature*, 592(7854):381–385, apr 2021.

[19] Martin A. Green, Ewan D. Dunlop, Jochen Hohl-Ebinger, Masahiro Yoshita, Nikos Kopidakis, and Anita W.Y. Ho-Baillie. Solar cell efficiency tables (Version 55). *Progress in Photovoltaics: Research and Applications*, 28(1):3–15, jan 2020.

[20] Xihong Hu, Hong Jiang, Juan Li, Jiaxin Ma, Dong Yang, Zhike Liu, Fei Gao, and Shengzhong (Frank) Liu. Air and thermally stable perovskite solar cells with CVD-graphene as the blocking layer. *Nanoscale*, 9(24):8274–8280, 2017.

[21] Zhaoning Song, Antonio Abate, Suneth C. Watthage, Geethika K. Liyanage, Adam B. Phillips, Ullrich Steiner, Michael Graetzel, and Michael J. Heben. Perovskite Solar Cell Stability in Humid Air: Partially Reversible Phase Transitions in the PbI 2 -CH 3 NH 3 I-H 2 O System. *Advanced Energy Materials*, 6(19):1600846, oct 2016.

[22] Azat F. Akbulatov, Sergey Yu Luchkin, Lyubov A. Frolova, Nadezhda N. Dremova, Kirill L. Gerasimov, Ivan S. Zhidkov, Denis V. Anokhin, Ernst Z. Kurmaev, Keith J. Stevenson, and Pavel A. Troshin. Probing the Intrinsic Thermal and Photochemical Stability of Hybrid and Inorganic Lead Halide Perovskites. *The Journal of Physical Chemistry Letters*, 8(6):1211–1218, mar 2017.

[23] Wanliang Tan, Andrea R. Bowring, Andrew C. Meng, Michael D. McGehee, and Paul C. McIntyre. Thermal Stability of Mixed Cation Metal Halide Perovskites in Air. *ACS Applied Materials Interfaces*, 10(6):5485–5491, feb 2018.

[24] Hiroyuki Kanda, Onovbaramwen J. Usiobo, Cristina Momblona, Mousa Abuhelaiqa, Albertus Adrian Sutanto, Cansu Igci, Xiao-Xin Gao, Jean-Nicolas Audinot, Tom Wirtz, and Mohammad Khaja Nazeeruddin. Light Stability Enhancement of Perovskite Solar Cells Using 1H , 1H , 2H , 2H -Perfluorooctyltriethoxysilane Passivation. *Solar RRL*, 5(3):2000650, mar 2021.

[25] Ying Cai, Shirong Wang, Mengna Sun, Xianggao Li, and Yin Xiao. Mixed cations and mixed halide perovskite solar cell with lead thiocyanate additive for high efficiency and long-term moisture stability. *Organic Electronics*, 53(August 2017):249–255, feb 2018.

[26] Michael Saliba, Taisuke Matsui, Ji-Youn Seo, Konrad Domanski, Juan-Pablo Correa-Baena, Mohammad Khaja Nazeeruddin, Shaik M. Zakeeruddin, Wolfgang Tress, Antonio Abate, Anders Hagfeldt, and Michael Grätzel. Cesium-containing triple cation perovskite solar cells: improved stability, reproducibility and high efficiency. *Energy Environmental Science*, 9(6):1989–1997, 2016.

[27] Michael Saliba, Taisuke Matsui, Konrad Domanski, Ji-Youn Seo, Amita Ummadisingu, Shaik M. Zakeeruddin, Juan-Pablo Correa-Baena, Wolfgang R. Tress, Antonio Abate, Anders Hagfeldt, and Michael Grätzel. Incorporation of rubidium cations into perovskite solar cells improves photovoltaic performance. *Science*, 354(6309):206–209, oct 2016.

[28] Xiao Xin Gao, Ding Jiang Xue, Dong Gao, Qiwei Han, Qian Qing Ge, Jing Yuan Ma, Jie Ding, Weifeng Zhang, Bao Zhang, Yaqing Feng, Gui Yu, and Jin Song Hu. High-Mobility Hydrophobic Conjugated Polymer as Effective Interlayer for Air-Stable Efficient Perovskite Solar Cells. *Solar RRL*, 3(1):1–8, 2019.

[29] Qi Jiang, Yang Zhao, Xingwang Zhang, Xiaolei Yang, Yong Chen, Zema Chu, Qiufeng Ye, Xingxing Li, Zhigang Yin, and Jingbi You. Surface passivation of perovskite film for efficient solar cells. *Nature Photonics*, 13(7):460–466, jul 2019.

[30] Rongrong Cheacharoen, Nicholas Rolston, Duncan Harwood, Kevin A. Bush, Reinhold H. Dauskardt, and Michael D. McGehee. Design and understanding of encapsulated perovskite solar cells to withstand temperature cycling. *Energy Environmental Science*, 11(1):144–150, 2018.

[31] Dianyu Dong, Junjie Li, Man Cui, Jinmei Wang, Yuhang Zhou, Liu Luo, Yufei Wei, Lei Ye, Hong Sun, and Fanglian Yao. In Situ "Clickable" Zwitterionic Starch-Based Hydrogel for 3D Cell Encapsulation. *ACS Applied Materials Interfaces*, 8(7):4442–4455, feb 2016.

[32] Muge Acik and Seth B Darling. Graphene in perovskite solar cells: device design, characterization and implementation. *Journal of Materials Chemistry A*, 4(17):6185–6235, 2016.

[33] Bo Li, Mengru Wang, Riyas Subair, Guozhong Cao, and Jianjun Tian. Significant Stability Enhancement of Perovskite Solar Cells by Facile Adhesive Encapsulation. *The Journal of Physical Chemistry C*, 122(44):25260–25267, nov 2018.

[34] Fabio Matteocci, Lucio Cinà, Enrico Lamanna, Stefania Cacovich, Giorgio Divitini, Paul A. Midgley, Caterina Ducati, and Aldo Di Carlo. Encapsulation for long-term stability enhancement of perovskite solar cells. *Nano Energy*, 30(July):162–172, dec 2016.

[35] Mark V. Khenkin, Eugene A. Katz, Antonio Abate, Giorgio Bardizza, Joseph J. Berry, Christoph Brabec, Francesca Brunetti, Vladimir Bulović, Quinn Burlingame, Aldo Di Carlo, Rongrong Cheacharoen, Yi-Bing Cheng, Alexander Colsmann, Stephane Cros, Konrad Domanski, Michał Dusza, Christopher J. Fell, Stephen R. Forrest, Yulia Galagan, Diego Di Girolamo, Michael Grätzel, Anders Hagfeldt, Elizabeth von Hauff, Harald Hoppe, Jeff Kettle, Hans Köbler, Marina S. Leite, Shengzhong Liu, Yueh-Lin Loo, Joseph M. Luther, Chang-Qi Ma, Morten Madsen, Matthieu Manceau, Muriel Matheron, Michael McGehee, Rico Meitzner, Mohammad Khaja Nazeeruddin, Ana Flavia Nogueira, Çağla Odabaşı, Anna Osherov, Nam-Gyu Park, Matthew O. Reese, Francesca De Rossi, Michael Saliba, Ulrich S. Schubert, Henry J. Snaith, Samuel D. Stranks, Wolfgang Tress, Pavel A. Troshin, Vida Turkovic, Sjoerd Veenstra, Iris Visoly-Fisher, Aron Walsh, Trystan Watson, Haibing Xie, Ramazan Yıldırım, Shaik Mohammed Zakeeruddin, Kai Zhu, and Monica Lira-Cantu. Consensus statement for stability assessment and reporting for perovskite photovoltaics based on ISOS procedures. *Nature Energy*, 5(1):35–49, jan 2020.

[36] Saikumar Nair and Jignasa V. Gohel. A study on optoelectronic performance of perovskite solar cell under different stress testing conditions. *Optical Materials*, 109(September):110377, nov 2020.

[37] Lei Shi, Martin P. Bucknall, Trevor L. Young, Meng Zhang, Long Hu, Jueming Bing, Da Seul Lee, Jincheol Kim, Tom Wu, Noboru Takamure, David R. McKenzie, Shujuan Huang, Martin A. Green, and Anita W. Y. Ho-Baillie. Gas chromatography–mass spectrometry analyses of encapsulated stable perovskite solar cells. *Science*, 368(6497), jun 2020.

[38] Clara Aranda, Antonio Guerrero, and Juan Bisquert. Crystalline Clear or Not: Beneficial and Harmful Effects of Water in Perovskite Solar Cells. *ChemPhysChem*, 20(20):2587–2599, oct 2019.

[39] Nicholas Aristidou, Irene Sanchez-Molina, Thana Chotchuangchutchaval, Michael Brown, Luis Martinez, Thomas Rath, and Saif A. Haque. The Role of Oxygen in the Degradation of Methylammonium Lead Trihalide Perovskite Photoactive Layers. *Angewandte Chemie*, 127(28):8326–8330, jul 2015.

[40] Alessandro Senocrate, Tolga Acartürk, Gee Yeong Kim, Rotraut Merkle, Ulrich Starke, Michael Grätzel, and Joachim Maier. Interaction of oxygen with halide perovskites. *Journal of Materials Chemistry A*, 6(23):10847–10855, 2018.

[41] K. Agroui and G. Collins. Characterisation of EVA encapsulant material by thermally stimulated current technique. *Solar Energy Materials and Solar Cells*, 80(1):33–45, oct 2003.

[42] Bing-Mau Chen, Cheng-Yu Peng, Ju-Lu Cho, and Glen Andrew Porter. Optimization of Solar Module Encapsulant Lamination by Optical Constant Determination of Ethylene-Vinyl Acetate. *International Journal of Photoenergy*, 2015:1–7, 2015.

[43] Felix Lang, Marc A. Gluba, Steve Albrecht, Jörg Rappich, Lars Korte, Bernd Rech, and Norbert H. Nickel. Perovskite Solar Cells with Large-Area CVD-Graphene for Tandem Solar Cells. *The Journal of Physical Chemistry Letters*, 6(14):2745–2750, jul 2015.

[44] Rui Wang, Jingjing Xue, Kai-Li Wang, Zhao-Kui Wang, Yanqi Luo, David Fenning, Guangwei Xu, Selbi Nuryyeva, Tianyi Huang, Yepin Zhao, Jonathan Lee Yang, Jiahui Zhu, Minhuan Wang, Shaun Tan, Ilhan Yavuz, Kendall N. Houk, and Yang Yang. Constructive molecular configurations for surface-defect passivation of perovskite photovoltaics. *Science*, 366(6472):1509–1513, dec 2019.

[45] Ashraf Uddin, Mushfika Upama, Haimang Yi, and Leiping Duan. Encapsulation of Organic and Perovskite Solar Cells: A Review. *Coatings*, 9(2):65, jan 2019.

[46] J. Scott Bunch, Scott S. Verbridge, Jonathan S. Alden, Arend M. van der Zande, Jeevak M. Parpia, Harold G. Craighead, and Paul L. McEuen. Impermeable Atomic Membranes from Graphene Sheets. *Nano Letters*, 8(8):2458–2462, aug 2008.

[47] Daniel E. Sheehy and Jörg Schmalian. Optical transparency of graphene as determined by the fine-structure constant. *Physical Review B*, 80(19):193411, nov 2009.

[48] Rongrong Cheacharoen, Caleb C. Boyd, George F. Burkhard, Tomas Leijtens, James A. Raiford, Kevin A. Bush, Stacey F. Bent, and Michael D. McGehee. Encapsulating perovskite solar cells to withstand damp heat and thermal cycling. *Sustainable Energy Fuels*, 2(11):2398–2406, 2018.

[49] Rongrong Cheacharoen, Kevin A. Bush, Nicholas Rolston, Duncan Harwood, Reinhold H. Dauskardt, and Michael D. McGehee. Damp Heat, Temperature Cycling and UV Stress Testing of Encapsulated Perovskite Photovoltaic Cells. In *2018 IEEE 7th World Conference on Photovoltaic Energy Conversion (WCPEC) (A Joint Conference of 45th IEEE PVSC, 28th PVSEC 34th EU PVSEC)*, pages 3498–3502. IEEE, jun 2018.

[50] Peng You, Zhike Liu, Qidong Tai, Shenghua Liu, and Feng Yan. Efficient Semitransparent Perovskite Solar Cells with Graphene Electrodes. *Advanced Materials*, 27(24):3632–3638, jun 2015.

[51] Gi-Hwan Kim, Hyungsu Jang, Yung Jin Yoon, Jaeki Jeong, Song Yi Park, Bright Walker, In-Yup Jeon, Yimhyun Jo, Hyun Yoon, Minjin Kim, Jong-Beom Baek, Dong Suk Kim, and Jin Young Kim. Fluorine Functionalized Graphene Nano Platelets for Highly Stable Inverted Perovskite Solar Cells. *Nano Letters*, 17(10):6385–6390, oct 2017.

[52] Hao Li, Leiming Tao, Feihong Huang, Qiang Sun, Xiaojuan Zhao, Junbo Han, Yan Shen, and Mingkui Wang. Enhancing Efficiency of Perovskite Solar Cells via Surface Passivation with Graphene Oxide Interlayer. *ACS Applied Materials Interfaces*, 9(44):38967–38976, nov 2017.

[53] Qing-Dan Yang‡, Jia Li, Yuanhang Cheng, Ho-Wa Li, Zhiqiang Guan, Binbin Yu, and Sai-Wing Tsang. Graphene oxide as an efficient hole-transporting material for high-performance perovskite solar cells with enhanced stability. *Journal of Materials Chemistry A*, 5(20):9852–9858, 2017.

[54] Menghua Zhu, Weiwei Liu, Weijun Ke, Lisha Xie, Pei Dong, and Feng Hao. Graphene-Modified Tin Dioxide for Efficient Planar Perovskite Solar Cells with Enhanced Electron Extraction and Reduced Hysteresis. *ACS Applied Materials Interfaces*, 11(1):666–673, jan 2019.

[55] Kwanpyo Kim, Zonghoon Lee, William Regan, C. Kisielowski, M. F. Crommie, and A. Zettl. Grain Boundary Mapping in Polycrystalline Graphene. *ACS Nano*, 5(3):2142–2146, mar 2011.

[56] Hyo Won Kim, Hee Wook Yoon, Seon-mi Yoon, Byung Min Yoo, Byung Kook Ahn, Young Hoon Cho, Hye Jin Shin, Hoichang Yang, Ungyu Paik, Soongeun Kwon, Jae-Young Choi, and Ho Bum Park. Selective Gas Transport Through Few-Layered Graphene and Graphene Oxide Membranes. *Science*, 342(6154):91–95, oct 2013.

[57] Yang Chen, Yuan-Yuan Yue, Shi-Rong Wang, Nan Zhang, Jing Feng, and Hong-Bo Sun. Graphene as a Transparent and Conductive Electrode for Organic Optoelectronic Devices. *Advanced Electronic Materials*, 5(10):1900247, oct 2019.

[58] Xiaofeng Tang, Marco Brandl, Benjamin May, Ievgen Levchuk, Yi Hou, Moses Richter, Haiwei Chen, Shi Chen, Simon Kahmann, Andres Osvet, Florian Maier, Hans-Peter Steinrück, Rainer Hock, Gebhard J. Matt, and Christoph J. Brabec. Photoinduced degradation of methylammonium lead triiodide perovskite semiconductors. *Journal of Materials Chemistry A*, 4(41):15896–15903, 2016.

[59] Xuhui Zhang, Zhaoqian Li, Yong Ding, Linhua Hu, Jiajiu Ye, Xu Pan, and Songyuan Dai. Highly efficient and stable perovskite solar cell prepared from an in situ pre-wetted PbI 2 nano-sheet array film. *Sustainable Energy Fuels*, 1(5):1056–1064, 2017.

[60] Constantinos C. Stoumpos, Christos D. Malliakas, and Mercouri G. Kanatzidis. Semiconducting Tin and Lead Iodide Perovskites with Organic Cations: Phase Transitions, High Mobilities, and Near-Infrared Photoluminescent Properties. *Inorganic Chemistry*, 52(15):9019–9038, aug 2013.

[61] Gang Hee Han, Fethullah Güneş, Jung Jun Bae, Eun Sung Kim, Seung Jin Chae, Hyeon-Jin Shin, Jae-Young Choi, Didier Pribat, and Young Hee Lee. Influence of Copper Morphology in Forming Nucleation Seeds for Graphene Growth. *Nano Letters*, 11(10):4144–4148, oct 2011.

[62] Lianfeng Zhao, He Tian, Scott H. Silver, Antoine Kahn, Tian-Ling Ren, and Barry P. Rand. Ultrasensitive Heterojunctions of Graphene and 2D Perovskites Reveal Spontaneous Iodide Loss. *Joule*, 2(10):2133–2144, oct 2018.

[63] Eric T. Hoke, Daniel J. Slotcavage, Emma R. Dohner, Andrea R. Bowring, Hemamala I. Karunadasa, and Michael D. McGehee. Reversible photo-induced trap formation in mixed-halide hybrid perovskites for photovoltaics. *Chemical Science*, 6(1):613–617, 2015.

[64] Jin-Wook Lee, Deok-Hwan Kim, Hui-Seon Kim, Seung-Woo Seo, Sung Min Cho, and Nam-Gyu Park. Formamidinium and Cesium Hybridization for Photo- and Moisture-Stable Perovskite Solar Cell. *Advanced Energy Materials*, 5(20):1501310, oct 2015.

[65] Irene Calizo, Igor Bejenari, Muhammad Rahman, Guanxiong Liu, and Alexander A. Balandin. Ultraviolet Raman microscopy of single and multilayer graphene. *Journal of Applied Physics*, 106(4):043509, aug 2009.

[66] Dale A. C. Brownson and Craig E. Banks. CVD graphene electrochemistry: the role of graphitic islands. *Physical Chemistry Chemical Physics*, 13(35):15825, 2011.

[67] Sibel Kasap, Hadi Khaksaran, Süleyman Çelik, Hasan Özkaya, Cenk Yanık, and Ismet I. Kaya. Controlled growth of large area multilayer graphene on copper by chemical vapour deposition. *Physical Chemistry Chemical Physics*, 17(35):23081–23087, 2015.

[68] Taeshik Yoon, Jeong Hun Mun, Byung Jin Cho, and Taek-Soo Kim. Penetration and lateral diffusion characteristics of polycrystalline graphene barriers. *Nanoscale*, 6(1):151–156, 2014.

[69] Pinshane Y. Huang, Carlos S. Ruiz-Vargas, Arend M. van der Zande, William S. Whitney, Mark P. Levendorf, Joshua W. Kevek, Shivank Garg, Jonathan S. Alden, Caleb J. Hustedt, Ye Zhu, Jiwoong Park, Paul L. McEuen, and David A. Muller. Grains and grain boundaries in single-layer graphene atomic patchwork quilts. *Nature*, 469(7330):389–392, jan 2011.

[70] Rassin Grantab, Vivek B. Shenoy, and Rodney S. Ruoff. Anomalous Strength Characteristics of Tilt Grain Boundaries in Graphene. *Science*, 330(6006):946–948, nov 2010.

[71] Dinh Loc Duong, Gang Hee Han, Seung Mi Lee, Fethullah Gunes, Eun Sung Kim, Sung Tae Kim, Heetae Kim, Quang Huy Ta, Kang Pyo So, Seok Jun Yoon, Seung Jin Chae, Young Woo Jo, Min Ho Park, Sang Hoon Chae, Seong Chu Lim, Jae Young Choi, and Young Hee Lee. Probing graphene grain boundaries with optical microscopy. *Nature*, 490(7419):235–239, oct 2012.

[72] Shahriary Leila and Athawale Anjali A. Graphene Oxide Synthesized by using Modified Hummers Approach. *International Journal of Renewable Energy and Environmental Engineering*, 02(01):58–63, 2014.

[73] Ping Tzeng, Bart Stevens, Ian Devlaming, and Jaime C. Grunlan. Polymer-graphene oxide quadlayer thin-film assemblies with improved gas barrier. *Langmuir*, 31(21):5919–5927, 2015.

[74] Weiwei Liu, Xiaohong Li, Yiling Song, Cong Zhang, Xiaobo Han, Hua Long, Bing Wang, Kai Wang, and Peixiang Lu. Cooperative Enhancement of Two-Photon-Absorption-Induced Photoluminescence from a 2D Perovskite-Microsphere Hybrid Dielectric Structure. *Advanced Functional Materials*, 28(26):1707550, jun 2018.

[75] Julian Ramírez, Armando D. Urbina, Andrew T. Kleinschmidt, Mickey Finn, Samuel J. Edmunds, Guillermo L. Esparza, and Darren J. Lipomi. Exploring the limits of sensitivity for strain gauges of graphene and hexagonal boron nitride decorated with metallic nanoislands. *Nanoscale*, 10(12):5559–5565, 2020.

[76] Emilio J. Juarez-Perez, Michael Wuβler, Francisco Fabregat-Santiago, Kerstin Lakus-Wollny, Eric Mankel, Thomas Mayer, Wolfram Jaegermann, and Ivan Mora-Sero. Role of the Selective Contacts in the Performance of Lead Halide Perovskite Solar Cells. *The Journal of Physical Chemistry Letters*, 5(4):680–685, feb 2014.

[77] E. Yablonovitch, T. Gmitter, R. M. Swanson, and Y. H. Kwark. A 720 mV open circuit voltage SiO x : c -Si:SiO x double heterostructure solar cell. *Applied Physics Letters*, 47(11):1211–1213, dec 1985.

[78] Bart Roose, Qiong Wang, and Antonio Abate. The Role of Charge Selective Contacts in Perovskite Solar Cell Stability. *Advanced Energy Materials*, 9(5):1803140, dec 2018.

[79] Ladislav Kavan. Electrochemistry and dye-sensitized solar cells. *Current Opinion in Electrochemistry*, 2(1):88–96, apr 2017.

[80] Ladislav Kavan, Nicolas Tétreault, Thomas Moehl, and Michael Grätzel. Electrochemical Characterization of TiO 2 Blocking Layers for Dye-Sensitized Solar Cells. *The Journal of Physical Chemistry C*, 118(30):16408–16418, jul 2014.

[81] Bo Xu, Jinbao Zhang, Yong Hua, Peng Liu, Linqin Wang, Changqing Ruan, Yuanyuan Li, Gerrit Boschloo, Erik M.J. Johansson, Lars Kloo, Anders Hagfeldt, Alex K.Y. Jen, and Licheng Sun. Tailor-Making Low-Cost Spiro[fluorene-9,9-xanthene]-Based 3D Oligomers for Perovskite Solar Cells. *Chem*, 2(5):676–687, may 2017.

[82] Gergely F. Samu, Rebecca A. Scheidt, Prashant V. Kamat, and Csaba Janáky. Electrochemistry and Spectroelectrochemistry of Lead Halide Perovskite Films: Materials Science Aspects and Boundary Conditions. *Chemistry of Materials*, 30(3):561–569, feb 2018.

[83] Zhanfeng Li, Jinbo Chen, Hui Li, Qi Zhang, Zhiliang Chen, Xiaolu Zheng, Guojia Fang, Hua Wang, and Yuying Hao. A facilely synthesized 'spiro' hole-transporting material based on spiro[3.3]heptane-2,6-dispirofluorene for efficient planar perovskite solar cells. *RSC Advances*, 7(66):41903–41908, 2017.

[84] Erin L. Ratcliff, Brian Zacher, and Neal R. Armstrong. Selective Interlayers and Contacts in Organic Photovoltaic Cells. *The Journal of Physical Chemistry Letters*, 2(11):1337–1350, jun 2011.

[85] Sampreetha Thampy, Boya Zhang, Ki-ha Hong, Kyeongjae Cho, and Julia W P Hsu. Altered Stability and Degradation Pathway of CH3NH3PbI3 in Contact with Metal Oxide. *ACS Energy Letters*, 5(4):1147–1152, apr 2020.

[86] Kelly Schutt, Pabitra K Nayak, Alexandra J Ramadan, Bernard Wenger, Yen-hung Lin, and Henry J Snaith. Overcoming Zinc Oxide Interface Instability with a Methylammonium-Free Perovskite for High-Performance Solar Cells. *Advanced Functional Materials*, 29(47):1900466, nov 2019.

[87] Wiley A. Dunlap-Shohl, Tianyang Li, and David B. Mitzi. Interfacial Effects during Rapid Lamination within MAPbI 3 Thin Films and Solar Cells. *ACS Applied Energy Materials*, 2(7):5083–5093, jul 2019.

[88] Ladislav Kavan, Ludmilla Steier, and Michael Grätzel. Ultrathin Buffer Layers of SnO 2 by Atomic Layer Deposition: Perfect Blocking Function and Thermal Stability. *The Journal of Physical Chemistry C*, 121(1):342–350, jan 2017.

[89] Shijing Sun, Tonio Buonassisi, and Juan-Pablo Correa-Baena. State-of-the-Art Electron-Selective Contacts in Perovskite Solar Cells. *Advanced Materials Interfaces*, 5(22):1800408, nov 2018.

[90] Philip Schulz, David Cahen, and Antoine Kahn. Halide Perovskites: Is It All about the Interfaces? *Chemical Reviews*, 119(5):3349–3417, mar 2019.

[91] Philip Schulz, Eran Edri, Saar Kirmayer, Gary Hodes, David Cahen, and Antoine Kahn. Interface energetics in organo-metal halide perovskite-based photovoltaic cells. *Energy Environmental Science*, 7(4):1377, 2014.

[92] Solène Béchu, Maryline Ralaiarisoa, Arnaud Etcheberry, and Philip Schulz. Photoemission Spectroscopy Characterization of Halide Perovskites. *Advanced Energy Materials*, 10(26):1904007, jul 2020.

[93] John M. Gregoire, Chengxiang Xiang, Xiaonao Liu, Martin Marcin, and Jian Jin. Scanning droplet cell for high throughput electrochemical and photoelectrochemical measurements. *Review of Scientific Instruments*, 84(2):024102, feb 2013.

[94] Helge S. Stein and John M. Gregoire. Progress and prospects for accelerating materials science with automated and autonomous workflows. *Chemical Science*, 10(42):9640–9649, 2019.

[95] Zemin Zhang, Sarah A. Lindley, Dan Guevarra, Kevin Kan, Aniketa Shinde, John M. Gregoire, Weihua Han, Erqing Xie, Joel A. Haber, and Jason K. Cooper. Fermi Level Engineering of Passivation and Electron Transport Materials for p-Type CuBi2O4 Employing a High-Throughput Methodology. *Advanced Functional Materials*, 30(24):2000948, jun 2020.

[96] Alexander V. Akkuratov, Ilya E. Kuznetsov, Ilya V. Martynov, Diana K. Sagdullina, Petr M. Kuznetsov, Laura Ciammaruchi, Fedor A. Prudnov, Mikhail V. Klyuev, Eugene A. Katz, and Pavel A. Troshin. What can we learn from model systems: Impact of polymer backbone structure on performance and stability of organic photovoltaics. *Polymer*, 183(September):121849, nov 2019.

[97] Claudia M. Cardona, Wei Li, Angel E. Kaifer, David Stockdale, and Guillermo C. Bazan. Electrochemical Considerations for Determining Absolute Frontier Orbital Energy Levels of Conjugated Polymers for Solar Cell Applications. *Advanced Materials*, 23(20):2367–2371, may 2011.

[98] Elena I. Romadina, Alexander V. Akkuratov, Sergey D. Babenko, Petr M. Kuznetsov, and Pavel A. Troshin. New low bandgap polymer for organic near-infrared photodetectors. *Thin Solid Films*, 717(November 2020):138470, jan 2021.

[99] Austin L. Jones, Zilong Zheng, Parand Riley, Ian Pelse, Junxiang Zhang, Maged Abdelsamie, Michael F. Toney, Seth R. Marder, Franky So, Jean-Luc Brédas, and John R. Reynolds. Acceptor Gradient Polymer Donors for Non-Fullerene Organic Solar Cells. *Chemistry of Materials*, 31(23):9729–9741, dec 2019.

[100] Md. Mahbubur Rahman, Narayan Chandra Deb Nath, and Jae-Joon Lee. Electrochemical Impedance Spectroscopic Analysis of Sensitization-Based Solar Cells. *Israel Journal of Chemistry*, 55(9):990–1001, sep 2015.

[101] Motonari Adachi, Masaru Sakamoto, Jinting Jiu, Yukio Ogata, and Seiji Isoda. Determination of Parameters of Electron Transport in Dye-Sensitized Solar Cells Using Electrochemical Impedance Spectroscopy. *The Journal of Physical Chemistry B*, 110(28):13872–13880, jul 2006.

[102] Francisco Fabregat-Santiago, Germà Garcia-Belmonte, Iván Mora-Seró, and Juan Bisquert. Characterization of nanostructured hybrid and organic solar cells by impedance spectroscopy. *Physical Chemistry Chemical Physics*, 13(20):9083, 2011.

[103] Francisco Fabregat-Santiago, Juan Bisquert, Germà Garcia-Belmonte, Gerrit Boschloo, and Anders Hagfeldt. Influence of electrolyte in transport and recombination in dye-sensitized solar cells studied by impedance spectroscopy. *Solar Energy Materials and Solar Cells*, 87(1-4):117–131, may 2005.

[104] Gergely F. Samu, Ádám Balog, Filippo De Angelis, Daniele Meggiolaro, Prashant V. Kamat, and Csaba Janáky. Electrochemical Hole Injection Selectively Expels Iodide from Mixed Halide Perovskite Films. *Journal of the American Chemical Society*, 141(27):10812–10820, jul 2019.

[105] Juan Bisquert, Francisco Fabregat-Santiago, Iván Mora-Seró, Germà Garcia-Belmonte, Eva M. Barea, and Emilio Palomares. A review of recent results on electrochemical determination of the density of electronic states of nanostructured metal-oxide semiconductors and organic hole conductors. *Inorganica Chimica Acta*, 361(3):684–698, feb 2008.

[106] Seul-Gi Kim, Jeong-Hyeon Kim, Philipp Ramming, Yu Zhong, Konstantin Schötz, Seok Joon Kwon, Sven Huettner, Fabian Panzer, and Nam-Gyu Park. How antisolvent miscibility affects perovskite film wrinkling and photovoltaic properties. *Nature Communications*, 12(1):1554, dec 2021.

[107] Jason J Yoo, Gabkyung Seo, Matthew R Chua, Tae Gwan Park, Yongli Lu, Fabian Rotermund, Young-ki Kim, Chan Su Moon, Nam Joong Jeon, Juan-Pablo Correa-Baena, Vladimir Bulović, Seong Sik Shin, Moungi G Bawendi, and Jangwon Seo. Efficient perovskite solar cells via improved carrier management. *Nature*, 590(7847):587–593, feb 2021.

[108] Elham Halvani Anaraki, Ahmad Kermanpur, Ludmilla Steier, Konrad Domanski, Taisuke Matsui, Wolfgang Tress, Michael Saliba, Antonio Abate, Michael Grätzel, Anders Hagfeldt, and Juan Pablo Correa-Baena. Highly efficient and stable planar perovskite solar cells by solution-processed tin oxide. *Energy and Environmental Science*, 9(10):3128–3134, 2016.

[109] Yonghui Lee, Seunghwan Lee, Gabseok Seo, Sanghyun Paek, Kyung Taek Cho, Aron J. Huckaba, Marco Calizzi, Dong-won Choi, Jin-Seong Park, Dongwook Lee, Hyo Joong Lee, Abdullah M. Asiri, and Mohammad Khaja Nazeeruddin. Efficient Planar Perovskite Solar Cells Using Passivated Tin Oxide as an Electron Transport Layer. *Advanced Science*, 5(6):1800130, jun 2018.

[110] Silver-Hamill Turren-Cruz, Anders Hagfeldt, and Michael Saliba. Methylammonium-free, high-performance, and stable perovskite solar cells on a planar architecture. *Science*, 362(6413):449–453, oct 2018.

[111] Axel F Palmstrom, James A Raiford, Rohit Prasanna, Kevin A Bush, Melany Sponseller, Rongrong Cheacharoen, Maxmillian C Minichetti, David S Bergsman, Tomas Leijtens, Hsin-ping Wang, Vladimir Bulović, Michael D. McGehee, and Stacey F Bent. Interfacial Effects of Tin Oxide Atomic Layer Deposition in Metal Halide Perovskite Photovoltaics. *Advanced Energy Materials*, 8(23):1800591, aug 2018.

[112] Ma Ro Kim, Hyung Wook Choi, and Chung Wung Bark. Low-Temperature Thermally Evaporated SnO 2 Based Electron Transporting Layer for Perovskite Solar Cells with Annealing Process. *Journal of Nanoscience and Nanotechnology*, 20(9):5491–5497, sep 2020.

[113] Yuxiao Guo, Xingtian Yin, Jie Liu, Wei Chen, Sen Wen, Meidan Que, Haixia Xie, Yawei Yang, Wenxiu Que, and Bowen Gao. Vacuum thermal-evaporated SnO2 as uniform electron transport layer and novel management of perovskite intermediates for efficient and stable planar perovskite solar cells. *Organic Electronics*, 65:207–214, feb 2019.

[114] Longbin Qiu, Zonghao Liu, Luis K. Ono, Yan Jiang, Dae-Yong Son, Zafer Hawash, Sisi He, and Yabing Qi. Scalable Fabrication of Stable High Efficiency Perovskite Solar Cells and Modules Utilizing Room Temperature Sputtered SnO 2 Electron Transport Layer. *Advanced Functional Materials*, 29(47):1806779, nov 2019.

[115] Guangfeng Bai, Zhengli Wu, Jing Li, Tongle Bu, Wangnan Li, Wei Li, Fuzhi Huang, Qi Zhang, Yi-Bing Cheng, and Jie Zhong. High performance perovskite sub-module with sputtered SnO2 electron transport layer. *Solar Energy*, 183(March):306–314, may 2019.

[116] P. Westbroek. Fundamentals of electrochemistry. In *Analytical Electrochemistry in Textiles*, pages 3–36. Elsevier, 2005.

[117] Anna Hankin, Franky E. Bedoya-Lora, John C Alexander, Anna Regoutz, and Geoff H. Kelsall. Flat band potential determination: avoiding the pitfalls. *Journal of Materials Chemistry A*, 7(45):26162–26176, 2019.

[118] Juan Pablo Correa-Baena, Yanqi Luo, Thomas M. Brenner, Jordan Snaider, Shijing Sun, Xueying Li, Mallory A. Jensen, Noor Titan Putri Hartono, Lea Nienhaus, Sarah Wieghold, Jeremy R. Poindexter, Shen Wang, Ying Shirley Meng, Ti Wang, Barry Lai, Martin V. Holt, Zhonghou Cai, Moungi G. Bawendi, Libai Huang, Tonio Buonassisi, and David P. Fenning. Homogenized halides and alkali cation segregation in alloyed organic-inorganic perovskites. *Science*, 363(6427):627–631, 2019.

[119] R. Sanjines, F. Lévy, V. Demarne, and A. Grisel. Some aspects of the interaction of oxygen with polycrystalline SnOx thin films. *Sensors and Actuators B: Chemical*, 1(1-6):176–182, jan 1990.

[120] S. Kaciulis, G. Mattogno, A. Galdikas, A. Mironas, and A. Setkus. Influence of surface oxygen on chemoresistance of tin oxide film. *Journal of Vacuum Science Technology A: Vacuum, Surfaces, and Films*, 14(6):3164–3168, nov 1996.

[121] Koichi Suematsu, Nan Ma, Ken Watanabe, Masayoshi Yuasa, Tetsuya Kida, and Kengo Shimanoe. Effect of Humid Aging on the Oxygen Adsorption in SnO2 Gas Sensors. *Sensors*, 18(1):254, jan 2018.

[122] Y. Son, A. Liao, and R. L. Peterson. Effect of relative humidity and pre-annealing temperature on spin-coated zinc tin oxide films made via the metal–organic decomposition route. *Journal of Materials Chemistry C*, 5(32):8071–8081, 2017.

[123] Alexander J.R. Botz, Michaela Nebel, Rosalba A. Rincón, Edgar Ventosa, and Wolfgang Schuhmann. Onset potential determination at gas-evolving catalysts by means of constant-distance mode positioning of nanoelectrodes. *Electrochimica Acta*, 179:38–44, oct 2015.

[124] M. Šeruga, M. Metikoš-Huković, T. Valla, M. Milun, H. Hoffschultz, and K. Wandelt. Electrochemical and X-ray photoelectron spectroscopy studies of passive film on tin in citrate buffer solution. *Journal of Electroanalytical Chemistry*, 407(1-2):83–89, may 1996.

[125] Bill X. Huang, Pete Tornatore, and Ying-Sing Li. IR and Raman spectroelectrochemical studies of corrosion films on tin. *Electrochimica Acta*, 46(5):671–679, jan 2001.

[126] Ross A Kerner and Barry P Rand. Linking Chemistry at the TiO2/CH3NH3PbI3 Interface to Current–Voltage Hysteresis. *The Journal of Physical Chemistry Letters*, 8(10):2298–2303, may 2017.

[127] Ross A. Kerner and Barry P. Rand. Electrochemical and Thermal Etching of Indium Tin Oxide by Solid-State Hybrid Organic–Inorganic Perovskites. *ACS Applied Energy Materials*, 2(8):6097–6101, aug 2019.

[128] Won-Kook Choi, Jun-Sik Cho, Seok-Kyun Song, Hyung-Jin Jung, and Seok-Keun Koh. Auger Electron and X-Ray Photoelectron Spectroscopy Studies of Oxidation of Tin Using S n O x Thin Films Grown by Reactive Ion-Assisted Deposition. *Japanese Journal of Applied Physics*, 35(Part 1, No. 11):5820–5824, nov 1996.

[129] Davide Barreca, Simona Garon, Eugenio Tondello, and Pierino Zanella. SnO2 Nanocrystalline Thin Films by XPS. *Surface Science Spectra*, 7(2):81–85, apr 2000.

[130] Michael A. Stranick and Anthony Moskwa. SnO2 by XPS. *Surface Science Spectra*, 2(1):50–54, jan 1993.

[131] Michael A. Stranick and Anthony Moskwa. SnO by XPS. *Surface Science Spectra*, 2(1):45–49, jan 1993.

[132] Tin — XPS Periodic Table — Thermo Fisher Scientific - US.

[133] Bettina Friedel, Christopher R. McNeill, and Neil C. Greenham. Influence of Alkyl Side-Chain Length on the Performance of Poly(3-alkylthiophene)/Polyfluorene All-Polymer Solar Cells. *Chemistry of Materials*, 22(11):3389–3398, jun 2010.

[134] Xiangbo Meng. An overview of molecular layer deposition for organic and organic-inorganic hybrid materials: Mechanisms, growth characteristics, and promising applications. *J. Mater. Chem. A*, 5(35):18326–18378, 2017.

[135] David Bilger, S. Zohreh Homayounfar, and Trisha L. Andrew. A critical review of reactive vapor deposition for conjugated polymer synthesis. *J. Mater. Chem. C*, 7(24):7159–7174, jun 2019.

[136] Malancha Gupta and Karen K. Gleason. Initiated chemical vapor deposition of poly(1H,1H,2H,2H-perfluorodecyl acrylate) thin films. *Langmuir*, 22(24):10047–10052, nov 2006.

117

[137] Fallon J.M. Colberts, Martijn M. Wienk, Ruurd Heuvel, Weiwei Li, Vincent M. Le Corre, L. Jan Anton Koster, and René A.J. Janssen. Bilayer–Ternary Polymer Solar Cells Fabricated Using Spontaneous Spreading on Water. *Adv. Energy Mater.*, 8(32):1802197, nov 2018.

[138] Guillermo L. Esparza and Darren J. Lipomi. Solid-phase deposition: Conformal coverage of micron-scale relief structures with stretchable semiconducting polymers. *ACS Mater. Lett.*, 3:988–995, 2021.

[139] Christopher J. Ellison and John M. Torkelson. The distribution of glass-transition temperatures in nanoscopically confined glass formers. *Nat. Mater.*, 2(10):695–700, sep 2003.

[140] Luke A. Galuska, Eric S. Muckley, Zhiqiang Cao, Dakota F. Ehlenberg, Zhiyuan Qian, Song Zhang, Simon Rondeau-Gagné, Minh D. Phan, John F. Ankner, Ilia N. Ivanov, and Xiaodan Gu. SMART transfer method to directly compare the mechanical response of water-supported and free-standing ultrathin polymeric films. *Nat. Commun.*, 12(1):1–11, apr 2021.

[141] Rodney D. Priestley, Christopher J. Ellison, Linda J. Broadbelt, and John M. Torkelson. Materials Science: Structural relaxation of polymer glasses at surfaces, interfaces, and in between. *Science (80-.).*, 309(5733):456–459, jul 2005.

[142] Mataz Alcoutlabi and Gregory B. McKenna. Effects of confinement on material behaviour at the nanometre size scale. *J. Phys. Condens. Matter*, 17(15):R461, apr 2005.

[143] Victor L Pushparaj, Manikoth M Shaijumon, Ashavani Kumar, Saravanababu Murugesan, Lijie Ci, Robert Vajtai, Robert J Linhardt, Omkaram Nalamasu, and Pulickel M Ajayan. Flexible energy storage devices based on nanocomposite paper. 104, 2007.

[144] Sergiy Markutsya, Chaoyang Jiang, Yuri Pikus, and Vladimir V. Tsukruk. Freely suspended layer-by-layer nanomembranes: Testing micromechanical properties. *Adv. Funct. Mater.*, 15(5):771–780, may 2005.

[145] Silvia Taccola, Francesco Greco, Alessandra Zucca, Claudia Innocenti, César De Julián Fernández, Giulio Campo, Claudio Sangregorio, Barbara Mazzolai, and Virgilio Mattoli. Characterization of free-standing PEDOT:PSS/iron oxide nanoparticle composite thin films and application as conformable humidity sensors. *ACS Appl. Mater. Interfaces*, 5(13):6324–6332, jul 2013.

[146] Mathias Ulbricht. Advanced functional polymer membranes. *Polymer (Guildf).*, 47(7):2217–2262, mar 2006.

[147] Toshinori Fujie, Noriyuki Matsutani, Manabu Kinoshita, Yosuke Okamura, Akihiro Saito, and Shinji Takeoka. Adhesive, flexible, and robust polysaccharide nanosheets integrated for tissue-defect repair. *Adv. Funct. Mater.*, 19(16):2560–2568, aug 2009.

[148] Yosuke Okamura, Koki Kabata, Manabu Kinoshita, Daizoh Saitoh, and Shinji Takeoka. Free-standing biodegradable poly(lactic acid) nanosheet for sealing operations in surgery. *Adv. Mater.*, 21(43):4388–4392, nov 2009.

[149] Wenlong Cheng, Michael J. Campolongo, Shawn J. Tan, and Dan Luo. Freestanding ultrathin nano-membranes via self-assembly. *Nano Today*, 4(6):482–493, dec 2009.

[150] Michael Stadermann, Salmaan H. Baxamusa, Chantel Aracne-Ruddle, Maverick Chea, Shuaili Li, Kelly Youngblood, and Tayyab Suratwala. Fabrication of large-area free-standing ultrathin polymer films. *J. Vis. Exp.*, 2015(100):e52832, jun 2015.

[151] Sumin Kang, Jae Bum Pyo, and Taek Soo Kim. Layer-by-Layer Assembly of Free-Standing Nanofilms by Controlled Rolling. *Langmuir*, 34(20):5831–5836, may 2018.

[152] Francesco Greco, Alessandra Zucca, Silvia Taccola, Arianna Menciassi, Toshinori Fujie, Hiroki Haniuda, Shinji Takeoka, Paolo Dario, and Virgilio Mattoli. Ultra-thin conductive free-standing PEDOT/PSS nanofilms. *Soft Matter*, 7(22):10642–10650, nov 2011.

[153] Jonghyeon Noh, Seonju Jeong, and Jung Yong Lee. Ultrafast formation of air-processable and high-quality polymer films on an aqueous substrate. *Nat. Commun.*, 7, 2016.

[154] Manish Pandey, Shyam S. Pandey, Shuichi Nagamatsu, Shuzi Hayase, and Wataru Takashima. Influence of backbone structure on orientation of conjugated polymers in the dynamic casting of thin floating-films. *Thin Solid Films*, 619:125–130, nov 2016.

[155] Yong Jae Kim, Hee Tae Jung, Chi Won Ahn, and Hwan Jin Jeon. Simultaneously Induced Self-Assembly of Poly(3-hexylthiophene) (P3HT) Nanowires and Thin-Film Fabrication via Solution-Floating Method on a Water Substrate. *Adv. Mater. Interfaces*, 4(19):1700342, oct 2017.

[156] Rory Runser, Samuel E. Root, Derick E. Ober, Kartik Choudhary, Alex X. Chen, Charles Dhong, Armando D. Urbina, and Darren J. Lipomi. Interfacial Drawing: Roll-to-Roll Coating of Semiconducting Polymer and Barrier Films onto Plastic Foils and Textiles. *Chemistry of Materials*, 31(21):9078–9086, nov 2019.

[157] Neil G. Connelly and William E. Geiger. Chemical Redox Agents for Organometallic Chemistry. *Chemical Reviews*, 96(2):877–910, jan 1996.

[158] Allen J Bard and Larry R Faulkner. Electrochemical Methods: Fundamentals and Applications. *Russ. J. Electrochem. 2002 3812*, 38(12):1364–1365, 2002.

[159] Moses Kodur, Zachary Dorfman, Ross A. Kerner, Justin H. Skaggs, Taewoo Kim, Sean P. Dunfield, Axel Palmstrom, Joseph J Berry, and David P Fenning. Electrochemical Screening of Contact Layers for Metal Halide Perovskites. *ACS Energy Letters*, 7(2):683–689, feb 2022.

[160] Richard Swartwout, Maximilian T. Hoerantner, and V. Bulović. Scalable Deposition Methods for Large-area Production of Perovskite Thin Films. *ENERGY ENVIRONMENTAL MATERIALS*, 2(2):119–145, jun 2019.

[161] Yawei Zhou, Adel Najar, Jing Zhang, Jiangshan Feng, Yang Cao, Zhigang Li, Xuejie Zhu, Dong Yang, and Shengzhong Frank Liu. Effect of Solvent Residue in the Thin-Film Fabrication on Perovskite Solar Cell Performance. *ACS Appl. Mater. Interfaces*, 14:28729–28737, jun 2022.

[162] Kartik Choudhary, Alexander X. Chen, Gregory M. Pitch, Rory Runser, Armando Urbina, Tim J. Dunn, Moses Kodur, Andrew T. Kleinschmidt, Benjamin G. Wang, Jordan A. Bunch, David P. Fenning, Alexander L. Ayzner, and Darren J. Lipomi. Comparison of the Mechanical Properties of a Conjugated Polymer Deposited Using Spin Coating, Interfacial Spreading, Solution Shearing, and Spray Coating. *ACS Appl. Mater. Interfaces*, 13(43):51436–51446, nov 2021.

[163] Timothy D. Siegler, Andrew Dawson, Peter Lobaccaro, David Ung, Markus E. Beck, Garrett Nilsen, and Leonard L. Tinker. The Path to Perovskite Commercialization: A Perspective from the United States Solar Energy Technologies Office. *ACS Energy Letters*, 7(5):1728–1734, may 2022.

[164] Jia Li, Ezra Alvianto, and Yi Hou. Developing the Next-Generation Perovskite/Si Tandems: Toward Efficient, Stable, and Commercially Viable Photovoltaics. *ACS Applied Materials Interfaces*, may 2022.

[165] Taisuke Matsui, Ji-Youn Seo, Michael Saliba, Shaik M. Zakeeruddin, and Michael Grätzel. Room-Temperature Formation of Highly Crystalline Multication Perovskites for Efficient, Low-Cost Solar Cells. *Advanced Materials*, 29(15):1606258, apr 2017.

[166] Jérémie Werner, Bjoern Niesen, and Christophe Ballif. Perovskite/Silicon Tandem Solar Cells: Marriage of Convenience or True Love Story? – An Overview. *Advanced Materials Interfaces*, 5(1):1700731, jan 2018.

[167] Zongqi Li, Yingzhi Zhao, Xi Wang, Yuchao Sun, Zhiguo Zhao, Yujing Li, Huanping Zhou, and Qi Chen. Cost Analysis of Perovskite Tandem Photovoltaics. *Joule*, 2(8):1559–1572, aug 2018.

[168] Joseph S. Manser, Makhsud I. Saidaminov, Jeffrey A. Christians, Osman M. Bakr, and Prashant V. Kamat. Making and Breaking of Lead Halide Perovskites. *Accounts of Chemical Research*, 49(2):330–338, feb 2016.

[169] David P. McMeekin, Golnaz Sadoughi, Waqaas Rehman, Giles E. Eperon, Michael Saliba, Maximilian T. Hörantner, Amir Haghighirad, Nobuya Sakai, Lars Korte, Bernd Rech, Michael B. Johnston, Laura M. Herz, and Henry J. Snaith. A mixed-cation lead mixed-halide perovskite absorber for tandem solar cells. *Science*, 351(6269):151–155, jan 2016.

[170] Kevin A. Bush, Salman Manzoor, Kyle Frohna, Zhengshan J. Yu, James A. Raiford, Axel F. Palmstrom, Hsin-Ping Wang, Rohit Prasanna, Stacey F. Bent, Zachary C. Holman, and Michael D. McGehee. Minimizing Current and Voltage Losses to Reach 25% Efficient Monolithic Two-Terminal Perovskite–Silicon Tandem Solar Cells. *ACS Energy Letters*, 3(9):2173–2180, sep 2018.

[171] Erkan Aydin, Thomas G. Allen, Michele De Bastiani, Lujia Xu, Jorge Ávila, Michael Salvador, Emmanuel Van Kerschaver, and Stefaan De Wolf. Interplay between temperature and bandgap energies on the outdoor performance of perovskite/silicon tandem solar cells. *Nature Energy*, 5(11):851–859, nov 2020.

[172] Jinhui Tong, Qi Jiang, Fei Zhang, Seok Beom Kang, Dong Hoe Kim, and Kai Zhu. Wide-Bandgap Metal Halide Perovskites for Tandem Solar Cells. *ACS Energy Letters*, 6(1):232–248, 2021.

[173] Somayeh Gholipour and Michael Saliba. Bandgap tuning and compositional exchange for lead halide perovskite materials. In *Characterization Techniques for Perovskite Solar Cell Materials*, pages 1–22. Elsevier, 2020.

[174] J Xu, CC Boyd, ZJ Yu, AF Palmstrom, DJ Witter, BW Larson, RM France, J Werner, SP Harvey, EJ Wolf, W Weigand, S Manzoor, MFAM van Hest, JJ Berry, JM Luther, ZC Holman, and MD McGehee. Triple-halide wide-band gap perovskites with suppressed phase segregation for efficient tandems. *Science*, 367(6482):1097–1104, 2020.

[175] Katelyn P. Goetz and Yana Vaynzof. The Challenge of Making the Same Device Twice in Perovskite Photovoltaics. *ACS Energy Letters*, 7(5):1750–1757, may 2022.

[176] B. P. MacLeod, F. G.L. Parlane, T. D. Morrissey, F. Häse, L. M. Roch, K. E. Dettelbach, R. Moreira, L. P.E. Yunker, M. B. Rooney, J. R. Deeth, V. Lai, G. J. Ng, H. Situ, R. H. Zhang, M. S. Elliott, T. H. Haley, D. J. Dvorak, A. Aspuru-Guzik, J. E. Hein, and C. P. Berlinguette. Self-driving laboratory for accelerated discovery of thin-film materials. *Science Advances*, 6(20), 2020.

[177] Jerrit Wagner, Christian G. Berger, Xiaoyan Du, Tobias Stubhan, Jens A. Hauch, and Christoph J. Brabec. The evolution of materials acceleration platforms: toward the laboratory of the future with amanda. *Journal of Materials Science*, 56(29):16422–16446, 2021.

[178] Y Zhao, J Zhang, Z Xu, S Sun, S Langner, NTP Hartono, T Heumueller, Y Hou, J Elia, N Li, GJ Matt, X Du, W Meng, A Osvet, K Zhang, T Stubhan, Y Feng, J Hauch, EH Sargent, T Buonassisi, and CJ Brabec. Discovery of temperature-induced stability reversal in perovskites using high-throughput robotic learning. *Nat Commun*, 12(1):2191, 2021.

[179] P Makuła, M Pacia, and W Macyk. How to correctly determine the band gap energy of modified semiconductor photocatalysts based on uv-vis spectra. *J Phys Chem Lett*, 9(23):6814–6817, 2018.

[180] J Tauc, Radu Grigorovici, and Anina Vancu. Optical properties and electronic structure of amorphous germanium. *physica status solidi (b)*, 15(2):627–637, 1966.

[181] Michele De Bastiani, Emmanuel Van Kerschaver, Quentin Jeangros, Atteq Ur Rehman, Erkan Aydin, Furkan H. Isikgor, Alessandro J. Mirabelli, Maxime Babics, Jiang Liu, Shynggys Zhumagali, Esma Ugur, George T. Harrison, Thomas G. Allen, Bin Chen, Yi Hou, Semen Shikin, Edward H. Sargent, Christophe Ballif, Michael Salvador, and Stefaan De Wolf. Toward Stable Monolithic Perovskite/Silicon Tandem Photovoltaics: A Six-Month Outdoor Performance Study in a Hot and Humid Climate. *ACS Energy Letters*, 6(8):2944–2951, aug 2021.

[182] Zewen Xiao, Yuanyuan Zhou, Hideo Hosono, Toshio Kamiya, and Nitin P. Padture. Bandgap Optimization of Perovskite Semiconductors for Photovoltaic Applications. *Chemistry – A European Journal*, 24(10):2305–2316, feb 2018.

[183] T. Jesper Jacobsson, Juan Pablo Correa-Baena, Meysam Pazoki, Michael Saliba, Kurt Schenk, Michael Grätzel, and Anders Hagfeldt. Exploration of the compositional space for mixed lead halogen perovskites for high efficiency solar cells. *Energy and Environmental Science*, 9(5):1706–1724, 2016.

[184] Giles E. Eperon, Kevin H. Stone, Laura E. Mundt, Tracy H. Schloemer, Severin N. Habisreutinger, Sean P. Dunfield, Laura T. Schelhas, Joseph J. Berry, and David T. Moore. The Role of Dimethylammonium in Bandgap Modulation for Stable Halide Perovskites. *ACS Energy Letters*, 5(6):1856–1864, jun 2020.

[185] Susanne Siebentritt, Thomas Paul Weiss, Mohit Sood, Max Hilaire Wolter, Alberto Lomuscio, and Omar Ramirez. How photoluminescence can predict the efficiency of solar cells. *Journal of Physics: Materials*, 4:042010, 2021.

[186] Morton B Brown and Alan B Forsythe. Robust tests for the equality of variances. *Journal of the American Statistical Association*, 69(346):364–367, 1974.

[187] AD Taylor, Q Sun, KP Goetz, Q An, T Schramm, Y Hofstetter, M Litterst, F Paulus, and Y Vaynzof. A general approach to high-efficiency perovskite solar cells by any antisolvent. *Nat Commun*, 12(1):1878, 2021.

[188] K Wang, MC Tang, HX Dang, R Munir, D Barrit, M De Bastiani, E Aydin, DM Smilgies, S De Wolf, and A Amassian. Kinetic stabilization of the sol-gel state in perovskites enables facile processing of high-efficiency solar cells. *Adv Mater*, 31(32):e1808357, 2019.

[189] Qingzhi An, Leonie Vieler, Katelyn P. Goetz, Oscar Telschow, Yvonne J. Hofstetter, Robin Buschbeck, Alexander D. Taylor, and Yana Vaynzof. Effect of antisolvent application rate on film formation and photovoltaic performance of methylammonium-free perovskite solar cells. *Advanced Energy and Sustainability Research*, 2(11):2100061, 2021.

[190] Geeta Sanon, Raj Rup, and Abhai Mansingh. Band-gap narrowing and band structure in degenerate tin oxide (SnO2) films. *Physical Review B*, 44(11):5672–5680, sep 1991.

[191] Raseong Kim, Xufeng Wang, and Mark Lundstrom. Notes on Fermi-Dirac Integrals 4th Edition. *arXiv*, (1):1–15, 2019.

[192] A.M. Sukhotin, M.S. Grilikhes, and E.V. Lisovaya. The influence of passivation on the kinetics of the dissolution of iron—I. Outer layer of the passivating film as a heavy doped thin semiconductor and mott-schottky equation. *Electrochimica Acta*, 34(2):109–112, feb 1989.